Summer 2019

Bimetallic Systems for Heterogeneous Catalysis and Tuning Electronic Properties of Functional Materials

Amy J. Brandt

BIMETALLIC SYSTEMS FOR HETEROGENEOUS CATALYSIS AND TUNING ELECTRONIC PROPERTIES OF FUNCTIONAL MATERIALS

by

Amy J. Brandt

Bachelor of Science
Truman State University, 2014

Submitted in Partial Fulfillment of the Requirements

For the Degree of Doctor of Philosophy in

Chemistry

College of Arts and Sciences

University of South Carolina

2019

Accepted by:

Donna A Chen, Major Professor

Michael L. Myrick, Committee Member

Richard D. Adams, Committee Member

John R. Regalbuto, Committee Member

Cheryl L. Addy, Vice Provost and Dean of the Graduate School

DEDICATION

To my parents, for always believing in me and providing invaluable motivation. Also to my lifelong friend and husband, Adam, who has selflessly supported me through my personal goals and endeavors.

ACKNOWLEDGEMENTS

There are many people with whom one interacts on the path to attaining a doctorate degree. Though sometimes it may feel otherwise, it most certainly is not a solitary journey. There are several individuals with whom I gladly worked that I would like to thank. I am extremely grateful to my advisor Dr. Donna Chen for her endless knowledge, patience, and motivation in mentoring me through my graduate research work. Thank you for your time and effort in always guiding me to becoming a better scientist. I would like to thank my committee members Dr. Rick Adams and Dr. John R. Regalbuto for their lessons in lectures, and Dr. Michael Myrick for the countless hours spent building and optimizing electronics and software in the lab. I would also like to thank Dr. John Monnier for his invaluable knowledge of industrial catalysis and cheerful sense of humor. I would like to thank my former lab colleagues, Dr. Randima Galhenage for first introducing me to the lab upon my arrival at USC; Dr. Audrey Phillips (Duke) for teaching me everything I know about the Leybold Chamber; Dr. Kangmin Xie for his training on the reactor system; and Dr. Grant Seuser for sharing his knowledge of "conventional" catalyst synthesis. I would also like to extend much appreciation and thanks to my current lab colleagues, Thathsara Maddumapatabandi for her insights on STM and assistance in all aspects in working in the lab; Deependra Shakya for his knowledge on running "conventional" catalytic experiments and assistance in moving heavy packages or opening tight cylinders; Sharfa Farzandh for her endless curiosity and care of the Leybold Chamber, and Narayan Acharya for his eagerness to learn. I must

extend my gratitude to the work done by the machinists Arthur Illingworth and Allen Frye, as well as Christian Price for technology support, Alex Skripnik from Omicron, and the individuals at Duniway and Swagelok for their crucial knowledge and assistance in troubleshooting. This journey would not have been possible without collaboration and training from Dr. Ye Lin, Dr. Stavros Karakalos, Dr. John Tengco, Dr. Weijian Diao, Dr. Ekaterina Dolgopolov, Dr. Allison Rice, Dr. Amrita Sarkar, Otega Ejegbavwo, Corey Martin and Travis Williams; and the many friends at USC including Alyssa Abraham, Hannah Liberatore, Esteban Villarreal, Stephen Roberts, and others, whose support and encouragement will always be remembered.

ABSTRACT

Throughout the past few decades, advancements have been made in altering monometallic materials through addition of a second metal to create a bimetallic material that displays enhanced properties over its monometallic components and optimized attributes toward the intended application. However, a lack of fundamental understanding of the interactions between the two metals and between the metals and their environment can hinder the process of designing enhanced functional materials with desirable properties. In this work, careful analysis of model catalysts and metal-organic frameworks (MOFs) is performed in ultrahigh vacuum, and evaluation of the catalytic activity of the catalysts and electronic properties of the MOFs establishes a relationship between the interactions of the bimetallic materials and their properties. Platinum-rhenium surfaces on diverse supports including TiO_2, HOPG, and Pt(111) are investigated for the effect of differences in their composition and morphology on their catalytic activity for the water-gas shift (WGS) reaction, as well as their potential for oxidation. Catalysts consisting of Pt with subsurface Re are found to have enhanced activity over Pt alone regardless of the support being used. However, clusters on the TiO_2 support have greater activity overall, indicating the oxide support plays a role in facilitating the reaction. The oxidation of Re is enhanced in the presence of Pt on all supports, and is attributed to greater dispersion when Re is intermixed with Pt.

The electronic properties of copper-containing MOFs are studied by transmetallating a second metal into the framework, including cobalt, rhodium, iron, manganese, ruthenium, or nickel to form a bimetallic MOF. Alternate secondary building units (SBUs) of monomeric M-HHTP, dimeric M_2-BTC and pentameric M_5-NIP metal centers are used with the monometallic and bimetallic MOFs to fully investigate the parameters that influence their electronic properties. The bimetallic CuCo-BTC and CuRh-BTC MOFs exhibit more density of states (DOS) near the Fermi edge (E_F) than the monometallic Cu-BTC MOF, demonstrating the influence of incorporating a second metal into the framework. However both the monometallic and bimetallic MOFs using the HHTP ligand all have greater DOS near E_F than the Cu-BTC MOF; and the Cu-NIP and CuRh-NIP also show enhanced DOS near E_F, suggesting the ligand plays an influential role in determining the DOS as well. Thin MOF films of Cu-BTC grown via dip-coating demonstrated successful transmetallation with Co to produce bimetallic CuCo-BTC films with controllable Co concentration based on immersion time and temperature. Films maintained a uniform coverage of the substrate and crystalline structure upon initial growth and after undergoing transmetallation.

TABLE OF CONTENTS

LIST OF FIGURES

LIST OF ABBREVIATIONS

AFM ..... Atomic force microscopy

BTC 1,3,5-benzenetricarboxylate

GIWAXS ..... Grazing incidence wide angle X-ray scattering

HHTP 2,3,5,6,10,11-hexahydroxytriphenylene

HOPG ..... Highly oriented pyrolytic graphite

ICP-AES ..... Inductively coupled plasma atomic emission spectroscopy

IRAS ..... Infrared reflection absorption spectroscopy

LEED ..... Low energy electron diffraction

ML ..... Monolayer

MOF ..... Metal-organic framework

NIP 5-nitroisophthalate

QCM ..... Quartz crystal microbalance

STM ..... Scanning tunneling microscopy

TPD ..... Temperature Programmed Desorption

UHV ..... Ultra-high vacuum

VLE ..... Vapor-liquid equilibrator

XPS ..... X-ray photoelectron spectroscopy

CHAPTER 1

INTRODUCTION

1.1 Bimetallic Materials

The study of bimetallic materials for fine tuning electronic and structural properties has been a source of interest for decades. The combination of two or more metals to form alloys, core-shell particles, or complex heterometallic structures has vastly expanded the pathways for designing functional materials. Their potential has flourished in a magnitude of applications ranging from catalysis[1,2] and electronics[3,4] to gas storage[5,6] and biomedical applications.[7,8] Many bimetallic systems exhibit superior properties over their monometallic counterparts.[9] Differences in performance for bimetallic materials from their individual components can be attributed to one of, or a combination of, three effects: 1) changes in electronic structure (ligand effect); 2) unique geometric arrangement of atoms (ensemble effect); or 3) separate, yet concurrent contribution from each metal toward the function of the material (bifunctional effect).[1,9,10] In order to isolate and understand these effects, different strategies of material preparation from ultrahigh vacuum (UHV) metal deposition to wet chemistry synthesis techniques have allowed careful adjustments of particle size, material composition, and structural orientation. The key to utilizing these materials in real-world applications is having fundamental knowledge of their morphology and structure, and evaluating how their properties behave and change in different environments. Establishing a basic understanding of bimetallic

systems paves the way for designing rational materials that possess the desirable characteristics and functionality that are sought after.

Bimetallic nanoparticles are highly studied for their application in catalysis based on their proven ability to enhance catalytic activity, improve selectivity, and extend the lifetime of the catalyst.[11,12] Platinum (Pt) based catalysts have been the focus of many studies due to their common use in hydrogenation, oxidation, and hydrogenolysis reactions.[12] Interest in the addition of rhenium (Re) to Pt catalysts has attracted substantial attention since the first industrial use of Pt-Re bimetallic catalysts in naptha reforming in the 1960's.[13,14] This bimetallic system has opened up many avenues of exploration related to the role of Re in catalytic reactions pertaining to its oxidation state and electronic interaction with Pt, as well as the influence of the catalyst support on the metal cluster morphology, composition, and reactivity.[14–21]

Metal-organic frameworks (MOFs) are another class of materials that have tunable properties. Most recently, the ability to synthesize MOFs containing more than one metal has become an innovative topic of research. MOFs can be defined as solid materials made up of hybrid organic-inorganic components. Clusters of metal nodes are connected by organic linkers that combine to form an extended, crystalline framework with inner porosity.[22,23] The incorporation of a second metal into the MOF framework while retaining porosity and crystallinity is not trivial, but it has proven to be successful.[24–28] Among the long list of applications that are relevant to bimetallic MOFs, one novel objective of incorporating a second metal into the framework is to obtain desirable electronic behavior. Metal node engineering and framework topology tailoring can alter the electronic properties of the MOF; shifting the originally insulating material

to exhibit intrinsic semiconducting behavior.[29] Bimetallic semiconducting MOFs that are able to retain their porosity and crystallinity have potential to advance supercapacitor[30] and thermoelectric[31] technologies, and improve current materials used in sensors[32] and catalysis.[33–35]

1.2 Catalysis and Surface Science

Catalysis is the phenomenon by which a reaction is accelerated by lowering the activation energy barrier between reactants and products. A catalyst material is used to alter the reaction pathway, but is not consumed in the reaction. By providing an advantageous energy pathway, catalysts improve process economics in terms of productivity and energy consumption.[36] Catalysis is very important to society, namely for its vital role in growing, manufacturing, and converting food,[37] products,[38] and energy.[39] Catalysis-based industries contribute to more than 35% of the global GDP,[40] and it has been estimated that ~90% of chemical products are derived in some manner from catalytic processes.[41] Some of the most important catalytic processes in industry take place via heterogeneous catalysis; this involves a solid catalyst with reactants and products in the gas or liquid phase. With efforts to reduce fossil fuel use, new catalysts are continually being developed to efficiently convert renewable resources such as biomass into fuels and fine chemicals.[42–44] Typically, heterogeneous catalysts used in industry consist of metal particles dispersed on a high surface area support.[45] From an economic standpoint, this is a convenient way to enable the greatest amount of active sites accessible for reaction using minimal material. However, this creates a catalyst that is ill defined and difficult to control, complicating studies intended for designing new and better catalysts. Since reactions in heterogeneous catalysis take place at the surface

interface between catalyst support and reactant molecules, techniques in surface science have been developed to reduce the complexities of the catalytic system and gain a fundamental understanding of how the catalyst operates.

Surface science is a very valuable approach to studying complex systems related to catalysis. The aim of using surface science is to fundamentally understand the relationship between atomic level structure of a catalyst surface and its catalytic performance.[46] By constructing model catalysts, the surface under study can be "simplified" and controlled. Typical model catalysts employ a single crystal support that has been well defined. The metals under investigation are then deposited on the support in a systematic way in order to study metal cluster structure, surface composition in bimetallic systems, and adsorption behavior that correlates to the catalytic activity.[47] Conducting studies with high resolution at the molecular and atomic scale typically requires a very clean environment and low gas pressures to eliminate contamination or interference from gas molecules. Many surface science techniques that operate in vacuum (and recently in near ambient pressure) have been developed that use photons, electrons, ions, and atoms as probes to uncover the atomic and electronic structures of surfaces and the nature of their chemical bonding with molecules.[48] Uncovering these phenomena can effectively guide the design of catalysts with greater activity, better selectivity, and longer lifetimes.

1.3 Motivation

Bimetallic materials are continuously developed and implemented all over the world in everyday life. From the catalytic converters in motor vehicles for reducing toxic gases, to sensing devices in thermostats used in homes. Understanding their atomic and

electronic structure is the foundation for designing materials to fit specific needs and improve systems in current applications. An array of surface science techniques are used in this work to study bimetallic systems in ultrahigh vacuum (UHV) including X-ray photoelectron spectroscopy (XPS), infrared reflection absorption spectroscopy (IRAS), scanning tunneling microscopy (STM), temperature programmed desorption (TPD), and low energy electron diffraction (LEED). The Pt-Re bimetallic system is studied specifically for its superior activity over monometallic Pt systems in the water-gas shift (WGS) reaction. Upon addition of Re to the Pt catalyst, the morphology, composition, and activity of bimetallic clusters have been investigated in previous work on an oxide support of TiO_2.[17,21] The work presented here expands on those results to understand the role of the support in influencing the catalytic activity, morphology, and composition of monometallic and bimetallic Pt and Re clusters. Supports of highly oriented pyrolytic graphite (HOPG) and a Pt(111) single crystal are used to decouple metal-metal interactions from metal-support interactions in the WGS reaction. The surface science techniques mentioned above are used to obtain comprehensive knowledge of the catalyst structure and composition in UHV. A microreactor coupled to the UHV chamber is used to bridge the pressure gap between the surface analysis in UHV and catalytic activity at atmospheric pressures. The design of the reactor allows samples to be analyzed before and after reaction without exposure to air, which is pertinent to understanding changes in structure or oxidation state caused by the reaction. The catalytic activity of many heterogeneous reactions that use the Pt-Re system, including the WGS reaction, depends on the oxidation state of the metal particles. Since Pt-Re catalysts are exposed to oxidizing environments in reactions such as aqueous phase reforming (APR) and

deoxydehydration of glycerol,[49,50] this work also seeks to understand the extent of Re oxidation in different systems. Re is oxidized at elevated temperatures and pressures in the microreactor, with and without the presence of Pt, as well as on three different supports (TiO_2, HOPG, and Pt(111)) to understand the influence of metal particle and support interactions on its oxidation state.

Metal-organic frameworks (MOFs) have emerged as very versatile materials, especially those containing more than one metal in their framework. Bimetallic MOFs are investigated in this work for the capacity to tune their electronic structure upon incorporation of a second metal and using various organic ligands in the framework. Copper MOFs constructed from Cu acetate and assorted linkers of BTC (BTC = benzenetricarboxylate), NIP (NIP = 5-nitroisophthalate) and HHTP (HHTP = 2,35,6,10,11-hexahydroxytriphenylene) are transmetallated with cobalt, rhodium, iron, manganese, ruthenium, zinc, and nickel to form bimetallic MOFs. The UHV technique of XPS can provide information on the density of states near the Fermi level in these bimetallic MOF materials, offering insight on their insulating or semiconducting properties. Progressing the use of MOFs in contemporary applications will require a sufficient means of incorporating MOF materials in solid-state devices. In this work, a novel procedure for synthesizing bimetallic MOF films is presented. Using a dip-coating method for achieving step-by-step growth, a monometallic Cu_3BTC_2 MOF film is grown on a support without the need for self-assembled monolayers. Transmetallation with Co^{2+} successfully incorporates Co into the metal nodes with Cu. The amount of cobalt incorporated can be analyzed using XPS and controlled through the temperature and length of time used during transmetallation. Grazing incidence wide angle X-ray

scattering (GIWAXS) shows the crystallinity of the MOF is maintained after transmetallation, and atomic force microscopy (AFM) exhibits uniform film coverage of the substrate.

Surface science techniques are used here to provide fundamental information on bimetallic materials from composition and density of states of thin film metal-organic frameworks and powders, to morphology, structure, and oxidation state of model Pt-Re catalysts. The pressure gap between UHV and conventional catalysis is bridged using an atmospheric microreactor coupled to the UHV chamber to correlate the surface properties of the model catalyst to its catalytic activity under real reaction conditions. The fundamental insights gained in this work lay the foundation for designing enhanced bimetallic materials for catalytic and electronic applications.

1.4 References

(1) Guczi, L. Bimetallic Nano-Particles: Featuring Structure and Reactivity. *Catal. Today* **2005**, *101*, 53–64.

(2) Singh, A. K.; Xu, Q. Synergistic Catalysis over Bimetallic Alloy Nanoparticles. *ChemCatChem* **2013**, *5*, 652–676.

(3) Mei, J.; Liao, T.; Spratt, H.; Ayoko, G. A.; Zhao, X. S.; Sun, Z. Honeycomb-Inspired Heterogeneous Bimetallic Co–Mo Oxide Nanoarchitectures for High-Rate Electrochemical Lithium Storage. *Small Methods* **2019**, *3*, 1900055.

(4) Kawamura, G.; Alvarez, S.; Stewart, I. E.; Catenacci, M.; Chen, Z.; Ha, Y.-C. Production of Oxidation-Resistant Cu-Based Nanoparticles by Wire Explosion. *Nat. Publ. Gr.* **2015**, *5*, 18333.

(5) Kim, D.; Song, K. S.; Buyukcakir, O.; Yildirim, T.; Coskun, A. Bimetallic Metal Organic Frameworks with Precisely Positioned Metal Centers for Efficient H_2 Storage. *Chem. Commun* **2018**, *54*, 12218.

(6) Yang, X.; Xu, Q. Bimetallic Metal−Organic Frameworks for Gas Storage and Separation. *Cryst. Growth Des.* **2017**, *17*, 1450–1455.

(7) Nasrabadi, H. T.; Abbasi, E.; Davaran, S.; Kouhi, M.; Akbarzadeh, A. Bimetallic Nanoparticles: Preparation, Properties, and Biomedical Applications. *Artif. Cells, Nanomedicine, Biotechnol.* **2016**, *44*, 376–380.

(8) McNamara, K.; M Tofail, S. A. Nanoparticles in Biomedical Applications. *Adv. Phys. X* **2017**, *2*, 54–88.

(9) Rodriguez, J. A.; Goodman, D. W. Surface Science Studies of the Electronic and Chemical Properties of Bimetallic Systems. *J. Phys. Chem.* **1991**, *95*, 4196–4206.

(10) Rodriguez, J. Physical and Chemical Properties of Bimetallic Surfaces. *Surf. Sci. Rep.* **1996**, *24*, 223–287.

(11) Sinfelt, J. H. Catalysis by Alloys and Bimetallic Catalysts. *Acc. Chem. Res.* **1977**, *10*, 15–20.

(12) Yu, W.; Porosoff, M. D.; Chen, J. G. Review of Pt-Based Bimetallic Catalysis: From Model Surfaces to Supported Catalysts. *Chem. Rev.* **2012**, *112*, 5780–5817.

(13) Kluhsdahl, H. E. Reforming a Sulfur-Free Naphtha with a Platinum-Rhenium Catalyst. *Chevron* **1968**, *US Patent*, 3,415,737.

(14) Xiao, J.; Puddephatt, R. J. Pt-Re Clusters and Bimetallic Catalysts. *Coord. Chem. Rev.* **1995**, *143*, 457–500.

(15) Azzam, K. G.; Babich, I. V.; Seshan, K.; Lefferts, L. Role of Re in Pt-Re/TiO_2 Catalyst for Water Gas Shift Reaction: A Mechanistic and Kinetic Study. *Appl.*

Catal. B Environ. **2008**, *80*, 129–140.

(16) Iida, H.; Igarashi, A. Difference in the Reaction Behavior between Pt-Re/TiO_2 (Rutile) and Pt-Re/ZrO_2 Catalysts for Low-Temperature Water Gas Shift Reactions. *Appl. Catal. A Gen.* **2006**, *303*, 48–55.

(17) Galhenage, R. P.; Xie, K.; Yan, H.; Seuser, G. S.; Chen, D. A. Understanding the Growth, Chemical Activity, and Cluster−Support Interactions for Pt−Re Bimetallic Clusters on TiO_2(110). *J. Phys. Chem. C* **2016**, *120*, 10866–10878.

(18) Duke, A. S.; Galhenage, R. P.; Tenney, S. A.; Sutter, P.; Chen, D. A. In Situ Studies of Carbon Monoxide Oxidation on Platinum and Platinum-Rhenium Alloy Surfaces. *J. Phys. Chem. C* **2015**, *119*, 28.

(19) Duke, A. S.; Galhenage, R. P.; Tenney, S. A.; Ammal, S. C.; Heyden, A.; Sutter, P.; Chen, D. A. In Situ Ambient Pressure X-Ray Photoelectron Spectroscopy Studies of Methanol Oxidation on Pt(111) and Pt–Re Alloys. *J. Phys. Chem. C* **2015**, *119*, 23082–23093.

(20) Duke, A. S.; Xie, K.; Monnier, J. R.; Chen, D. A. Superior Long-Term Activity for a Pt-Re Alloy Compared to Pt in Methanol Oxidation Reactions. *Surf. Sci.* **2017**, *657*, 35–43.

(21) Duke, A. S.; Xie, K.; Brandt, A. J.; Maddumapatabandi, T. D.; Ammal, S. C.; Heyden, A.; Monnier, J. R.; Chen, D. A. Understanding Active Sites in the Water-Gas Shift Reaction for Pt-Re Catalysts on Titania. *ACS Catal.* **2017**, *7*, 2597–2606.

(22) Tranchemontagne, D. J.; Mendoza-Corte, J. L.; O'Keeffe, M.; Yaghi, O. M. Secondary Building Units, Nets and Bonding in the Chemistry of Metal-Organic Frameworks. *Chem. Soc. Rev.* **2009**, *38*, 1257–1283.

(23) Stock, N.; Biswas, S. Synthesis of Metal-Organic Frameworks (MOFs): Routes to Various MOF Topologies, Morphologies, and Composites. *Chem. Rev.* **2012**, *112*, 933–969.

(24) Kim, M.; Cahill, J. F.; Fei, H. H.; Prather, K. A.; Cohen, S. M. Postsynthetic Ligand and Cation Exchange in Robust Metal-Organic Frameworks. *J. Am. Chem. Soc.* **2012**, *134*, 18082–18088.

(25) Shultz, A. M.; Sarjeant, A. A.; Farha, O. K.; Hupp, J. T.; Nguyen, S. T. Post-Synthesis Modification of a Metal-Organic Framework To Form Metallosalen-Containing MOF Materials. *J. Am. Chem. Soc* **2011**, *133*, 13252–13255.

(26) Lalonde, M.; Bury, W.; Karagiaridi, O.; Brown, Z.; Hupp, J. T.; Farha, O. K. Transmetalation: Routes to Metal Exchange within Metal-Organic Frameworks. *J. Mater. Chem. A* **2013**, *1*, 5453–5468.

(27) Zhai, Q. G.; Bu, X. H.; Mao, C. Y.; Zhao, X.; Feng, P. Y. Systematic and Dramatic Tuning on Gas Sorption Performance in Heterometallic Metal-Organic Frameworks. *J. Am. Chem. Soc.* **2016**, *138*, 2524–2527.

(28) Brozek, C. K.; Dinca, M. Cation Exchange at the Secondary Building Units of Metal-Organic Frameworks. *Chem. Soc. Rev.* **2014**, *43*, 5456–5467.

(29) Dolgopolova, E. A.; Brandt, A. J.; Ejegbavwo, O. A.; Duke, A. S.; Maddumapatabandi, T. D.; Galhenage, R. P.; Larson, B. W.; Reid, O. G.; Ammal, S. C.; Heyden, A.; et al. Electronic Properties of Bimetallic Metal-Organic Frameworks (MOFs): Tailoring Density of Electronic States Through MOF Modularity. *J. Am. Chem. Soc.* **2017**, *139*, 5201–5209.

(30) Chen, C.; Wu, M.-K.; Tao, K.; Zhou, J.-J.; Li, Y.-L.; Han, X.; Han, L. Formation of Bimetallic Metal–Organic Framework Nanosheets and Their Derived Porous Nickel–Cobalt Sulfides for Supercapacitors. *Dalt. Trans.* **2018**, *47*, 5639–5645.

(31) Sun, L.; Liao, B.; Sheberla, D.; Kraemer, D.; Zhou, J.; Stach, E. A.; Zakharov, D.; Stavila, V.; Alec Talin, A.; Ge, Y.; et al. A Microporous and Naturally Nanostructured Thermoelectric Metal-Organic Framework with Ultralow Thermal Conductivity. *Joule* **2017**, *1*, 168–177.

(32) Campbell, M. G.; Dincă, M. Metal–Organic Frameworks as Active Materials in Electronic Sensor Devices. *Sensors* **2017**, *17*, 1108.

(33) Sun, Q.; Liu, M.; Li, K.; Han, Y.; Zuo, Y.; Chai, F.; Song, C.; Zhang, G.; Guo, X. Synthesis of Fe/M (M = Mn, Co, Ni) Bimetallic Metal Organic Frameworks and Their Catalytic Activity for Phenol Degradation under Mild Conditions. *Inorg. Chem. Front* **2017**, *4*, 144–153.

(34) Pariyar, A.; Yaghoobnejad Asl, H.; Choudhury, A. Tetragonal versus Hexagonal: Structure-Dependent Catalytic Activity of Co/Zn Bimetallic Metal−Organic Frameworks. *Inorg. Chem* **2016**, *55*, 9250–9257.

(35) Shakya, D. M.; Ejegbavwo, O.; Farzandh, S.; Brandt, A. J.; Thayalan, R.; Senanyake, S. D.; Ebrahim, A.; Frenkel, A.; Tate, G.; Monnier, J. R.; et al. Metal Nodes in Bimetallic Metal-Organic Frameworks as Isolated, Catalytically Active Sites: Propylene Hydrogenation on CuRhBTC. *Manuscr. Prep.* **2019**.

(36) Wells, P. B. *Encyclopedia of Materials: Science and Technology*; 2nd ed.; University of Hull, UK, 2001.

(37) Ertl, G. Primary Steps in Catalytic Synthesis of Ammonia. *J. Vac. Sci. Technol. A Vacuum, Surfaces, Film.* **1983**, *1*, 1247–1253.

(38) Looi, M.-H.; Lee, S.-T.; Abd-Hamid, S. B. Use of Citric Acid in Synthesizing a Highly Dispersed Copper Catalyst for Selective Hydrogenolysis. *Chinese J. Catal.* **2008**, *29*, 566–570.

(39) Rostrup-Nielsen, J. R. Fuels and Energy for the Future: The Role of Catalysis. *Catal. Rev.* **2004**, *46*, 247–270.

(40) Hutchings, G. J.; Catlow, C. R. A.; Hardacre, C.; Davidson, M. G. Catalysis Making the World a Better Place: Satellite Meeting. *Philos. Trans. R. Soc. A Math.*

Phys. Eng. Sci. **2016**, *374*, 20150358.

(41) Recognizing the Best in Innovation: Breakthrough Catalyst. *R&D Magazine*. September 2005, p. 20.

(42) Kobayashi, H.; Ohta, H.; Fukuoka, A. Conversion of Lignocellulose into Renewable Chemicals by Heterogeneous Catalysis. *Catal. Sci. Technol* **2012**, *2*, 869–883.

(43) Lanzafame, P.; Centi, G.; Perathoner, S. Catalysis for Biomass and CO_2 Use through Solar Energy: Opening New Scenarios for a Sustainable and Low-Carbon Chemical Production. *Chem. Soc. Rev* **2014**, *43*, 7562.

(44) Huber, G. W.; Iborra, S.; Corma, A. Synthesis of Transportation Fuels from Biomass: Chemistry, Catalysts, and Engineering. *Chem. Rev.* **2006**, *106*, 4044–4098.

(45) Sakata, Y.; Tamaura, Y.; Imamura, H.; Watanabe, M. Preparation of a New Type of $CaSiO_3$ with High Surface Area and Property as a Catalyst Support. *Stud. Surf. Sci. Catal.* **2006**, *162*, 331–338.

(46) Campbell, C. T. Studies of Model Catalysts with Well-Defined Surfaces Combining Ultrahigh Vacuum Surface Characterization with Medium- and High-Pressure Kinetics. *Adv. Catal.* **1989**, *36*, 1–54.

(47) Freund, H.-J.; Libuda, J.; Bäumer, M.; Risse, T.; Carlsson, A. Clusters, Facets, and Edges: Site-Dependent Selective Chemistry on Model Catalysts. *Chem. Rec.* **2004**, *3*, 181–200.

(48) Somorjai, G. A. The Development of Molecular Surface Science and the Surface Science of Catalysis : The Berkeley Contribution. *J. Phys. Chem. B* **2000**, *104*, 2969–2979.

(49) Zhang, L.; Karim, A. M.; Engelhard, M. H.; Wei, Z. H.; King, D. L.; Wang, Y. Correlation of Pt-Re Surface Properties with Reaction Pathways for the Aqueous-Phase Reforming of Glycerol. *J. Catal.* **2012**, *287*, 37–43.

(50) Nijem, S.; Dery, S.; Carmiel, M.; Horesh, G.; Garrevoet, J.; Spiers, K.; Falkenberg, G.; Marini, C.; Gross, E. Bimetallic Pt−Re Nanoporous Networks: Synthesis, Characterization, and Catalytic Reactivity. *J. Phys. Chem. C* **2018**, *122*, 24801–24808.

CHAPTER 2

EXPERIMENTAL TECHNIQUES

2.1 X-ray Photoelectron Spectroscopy (XPS)

X-ray photoelectron spectroscopy (XPS) is a powerful analytical technique that can provide an abundance of information over a wide variety of samples. XPS is capable of identifying all elements (except H and He); it can provide information on the molecular environment, including oxidation state and bonded atoms; and it can be used for semiquantitative determination of the elemental surface composition.[1] X-rays of a known energy, typically from an Al or Mg source, irradiate the sample; energy from the X-ray photons is then transferred to core-level electrons in the sample, leading to photoemission of those electrons into vacuum. Figure 2.1 displays a schematic of a typical XPS experimental setup. The photoelectrons are collected from vacuum by a series of lenses, and then pass through a hemispherical analyzer that separates the photoelectrons based on their kinetic energy before arriving at the detector. The binding energy (E_B) of the detected electrons can be calculated based on the equation:

$$E_B = hv - E_K - \phi$$

where hv is the incident photon energy, E_K is the kinetic energy of the photoelectron, and ϕ is the work function. The work function is typically related to the spectrometer for conducting samples, and represents the minimum energy required to eject an electron from the highest occupied level into vacuum.

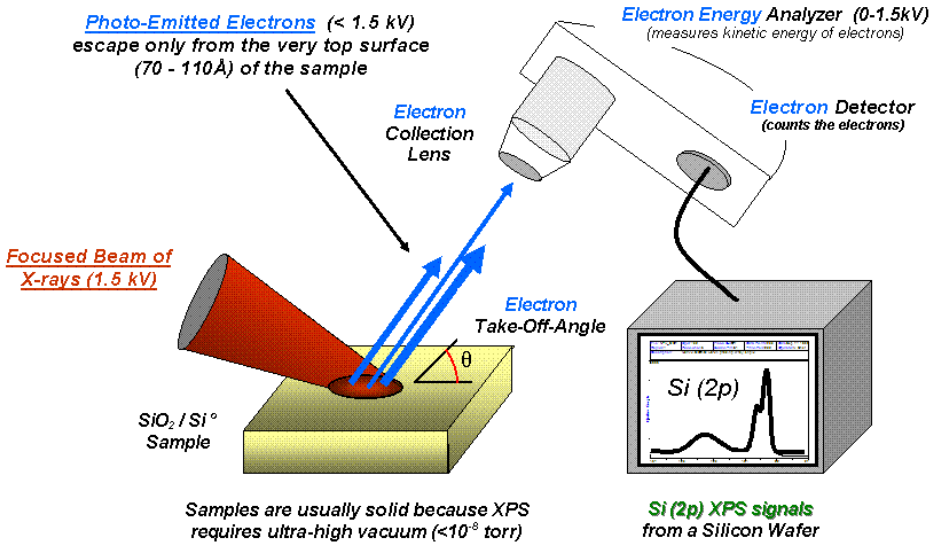

Figure 2.1: Schematic of the equipment and principle of X-ray photoelectron spectroscopy.[2]

Negatively charged core electrons are bound to the atom by the positively charged nucleus. The closer the electron is to the nucleus, the more tightly it will be bound; therefore the binding energy of the electron is specific to the type of atom it comes from. This makes it possible to identify different elements as well as their chemical environment based on binding energy shifts. While X-rays can easily penetrate through hundreds of nanometers of solid material, electrons have a much shorter mean free path, and can only penetrate ~10 nm.[1] XPS is therefore classified as a surface characterization technique for analyzing samples.

XPS is also capable of providing information regarding the conductive nature of a material. Analysis of the valence band spectrum can elucidate the extent of electron density that resides at or near the Fermi level of a sample. A greater intensity of electron density at the Fermi level is indicative of a conductive or semiconductive material. Less intensity near the Fermi level is characteristic of an insulator.

2.2 Infrared Reflection Absorption Spectroscopy (IRAS)

Infrared reflection absorption spectroscopy (IRAS) allows for identification of surface species generated by molecular adsorption and surface reactions. It can be operated in both high and low pressure conditions, and is generally nondestructive toward the sample. Infrared radiation is directed on the sample at an incident angle, where the radiation can interact with molecular dipoles on the surface creating vibrational excitation before being reflected into the detector. These vibrational modes originating from molecules or functional groups on the surface can be detected and identified. A flat metal substrate is typically used to achieve specular reflection. The "Surface Selection Rule" dictates the orientation in which the dipole change must occur in order to be detected (Figure 2.2a). Incident light parallel to the substrate, denoted as s-polarized, undergoes a 180-degree phase shift upon reflection with the substrate, resulting in a net amplitude of zero for the incident and emitted electric vectors parallel to the surface. Incident light perpendicular to the substrate, denoted as p-polarized, has a net radiation amplitude that is nearly twice that of the incident radiation at the point of contact at the surface.[3] Thus, only dipole changes perpendicular to the surface will be observed in IRAS.

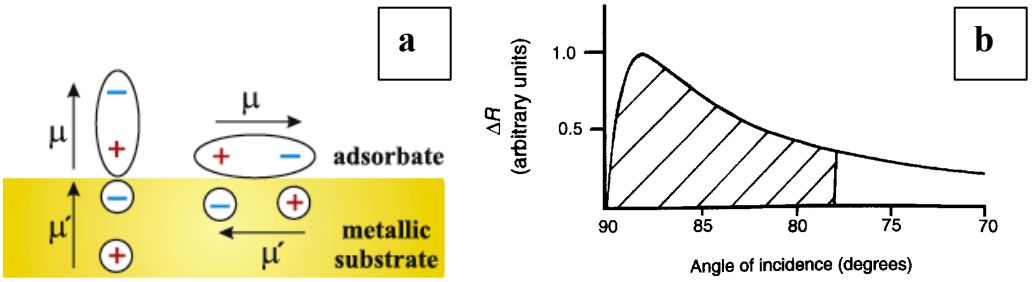

Figure 2.2: a) Schematic of the "Surface Selection Rule" in which dipole changes perpendicular to the surface are IR active and dipole changes parallel to the surface are IR inactive.[4] **b)** Schematic representation of the variation in band intensity with angle of incidence.[1]

IRAS is particularly powerful in studying adsorbed layers on metal surfaces by taking advantage of the grazing angle of incident light. The absorption of IR radiation by the adsorbate overlayer is enhanced at high angles of incidence, maximizing the reflectance of p-polarized light. Figure 2.2b represents the degree of reflectance achieved by grazing incidence angle.

For IRAS experiments conducted in this work, the setup allowed for the sample to remain in UHV while IR measurements were made. A SiC globar and tungsten halogen lamp provided sources of mid-infrared and near-infrared radiation. The beam traveled through one BaF_2 window of the vacuum chamber to reflect off the sample under analysis, then passed through a second BaF_2 window before traveling to the external liquid nitrogen cooled mercury cadmium telluride (LN-MCT) detector. In this manner, IRAS experiments sensitive to low concentrations of adsorbates could be conducted, as well as post-reaction evaluation of species remaining on the sample surface. Figure 2.3 shows the portion of the chamber where the sample was positioned to allow the IR beam to reflect across the surface.

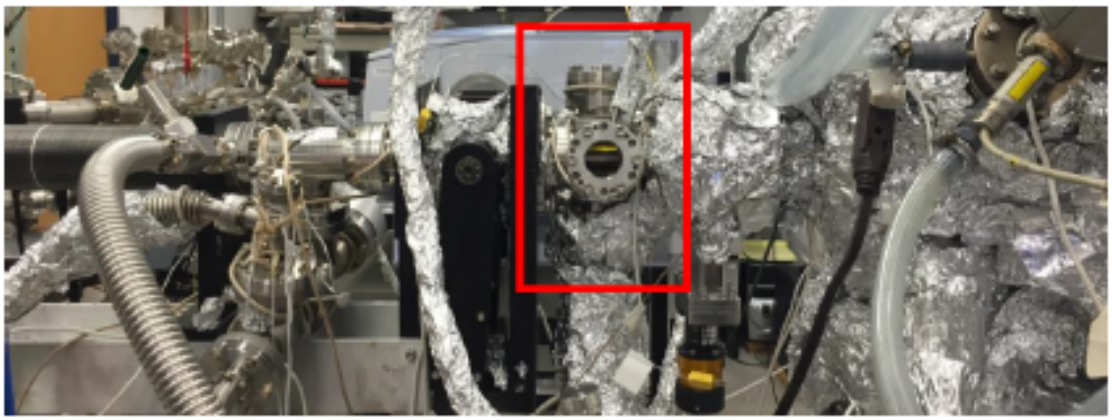

Figure 2.3: Photograph of the IR beam path and sample position on the UHV chamber.

2.3 Raman Spectroscopy

Raman spectroscopy is a form of vibrational spectroscopy similar to IR spectroscopy, however Raman bands arise from a change in the polarizability of the molecule, as opposed to a change in the dipole moment observed with IR.[1] Photons from the beam of incident light are absorbed by the material and scattered. When a photon interacts with the electric field of a molecule, an electron is excited to a virtual state lower in energy than a real electronic transition, and de-excitation results in a change of vibrational energy. The energy difference between the incident and emitted radiation is measured to detect molecular vibrations in the sample. In the work here, Raman spectroscopy was used to identify molecular bonding in bimetallic MOF samples.

2.4 UHV-Coupled Microreactor

The custom built microreactor[5] used in this work was designed to bridge the pressure gap between fundamental surface studies and conventional catalytic experiments. The microreactor is coupled to the UHV chamber, allowing samples to be prepared and fully characterized by UHV techniques both before and after reactions without ever exposing it to air (Figure 2.4). Thus, characteristics such as metal oxidation state and carbonaceous species can be analyzed by XPS, and post-reaction adsorbates can be examined by IRAS without influence from air or contamination. The reactor has a small dead volume (32 cm^3) built to house model catalysts with a low number of active sites in order to maximize sensitivity to the products formed (Figure 2.5). In addition to operating in flow-through mode (single-pass mode), the reactor can run in recirculation mode in which the reactants are passed over the catalyst multiple times until a sufficient concentration of product molecules accumulate to be detected. The system is equipped

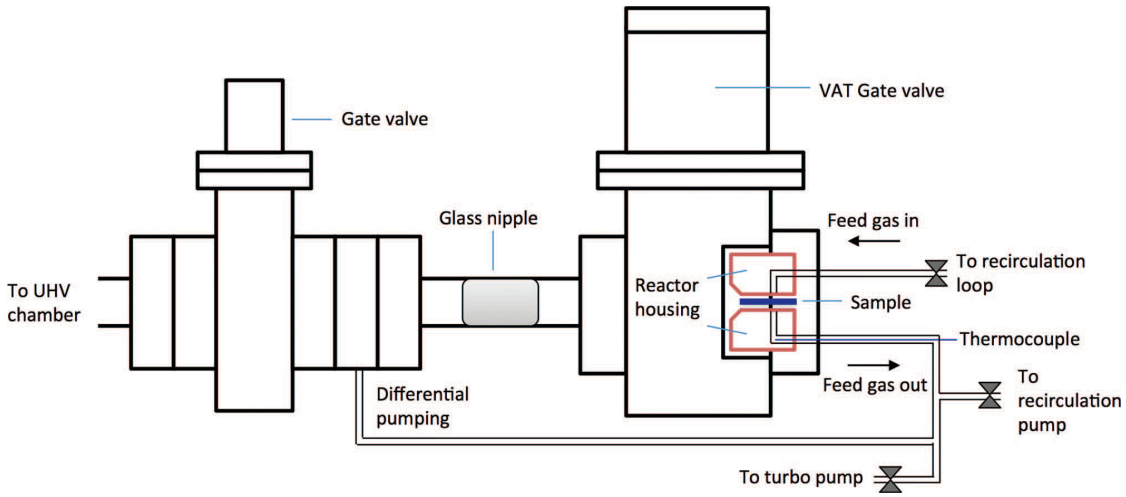

Figure 2.4: Diagram of the microreactor coupled to UHV.[5]

with a gas chromatogram (GC) for product separation and detection by either a thermal conductivity detector (TCD) or flame ionization detector (FID) for quantitative analysis. The microreactor is built to withstand heating temperatures up to 190 °C and operate at pressures of ~ 1 atm. Computer-controlled, automated switching valves initiate injections to the GC-TCD/FID and refilling of the reactor loop with fresh feed gas in order for multi-hour experiments to be run reliably without interruption. The design of this microreactor enabled real, catalytic experiments over model catalysts to be achieved.

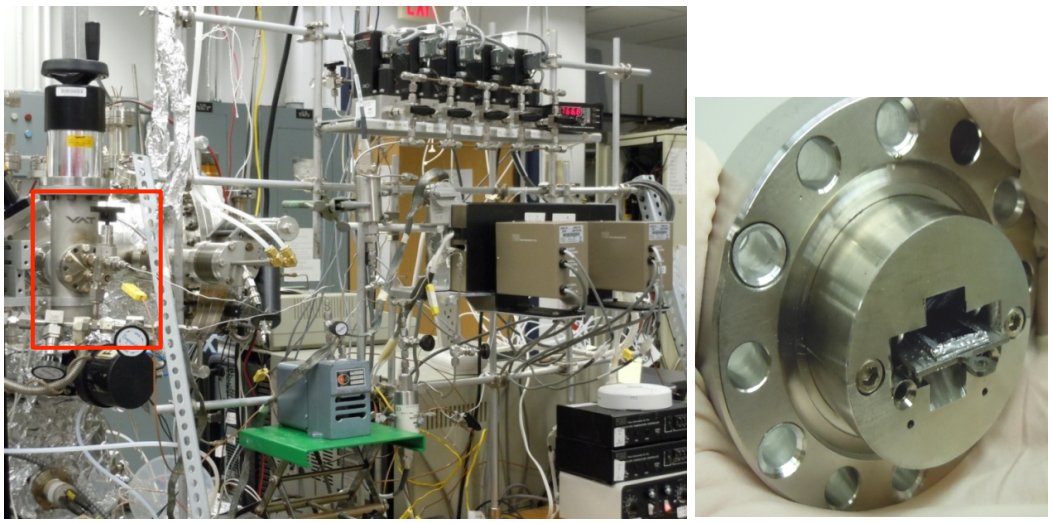

Figure 2.5: Photographs of the reactor loop and microreactor housing.[5]

2.5 Scanning Tunneling Microscopy (STM)

In scanning tunneling microscopy (STM), a sharp probe is used to scan across the sample in raster-fashion to detect changes in the surface structure on the atomic scale.[1] STM takes advantage of the quantum mechanical phenomenon of quantum tunneling. Electron tunneling through vacuum occurs when the tip is brought within a few angstroms of the sample surface and a voltage difference is applied. In constant current mode, the tunneling current is measured at each position and the voltage is adjusted to maintain a set current. Changes in the bias voltage cause the piezoelectric crystal to move up and down, and the resulting image maps the surface electron density of the sample as a function of vertical tip displacement (Figure 2.6).[6] An atomically sharp tip is necessary to achieve undistorted, high-resolution images. Tips can be made by electrochemical etching of a tungsten wire using NaOH. Tips can also be conditioned by applying high voltage pulses between the tip and the sample to draw tungsten atoms towards the apex of the tip, or to remove contaminants that have adsorbed during scanning.

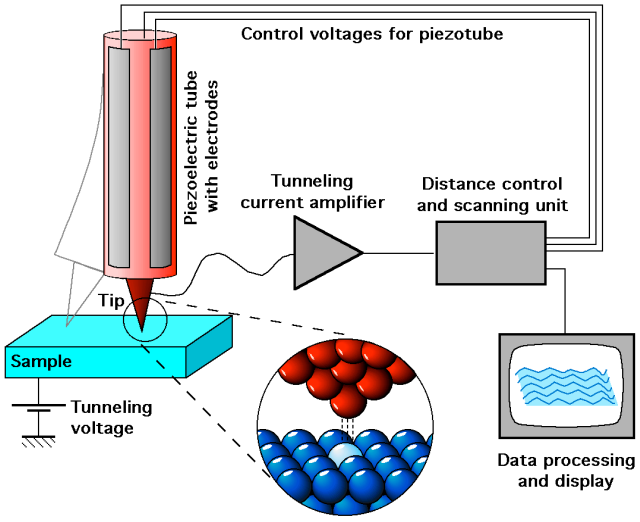

Figure 2.6: Schematic of the equipment and principle of scanning tunneling microscopy.[6]

STM experiments require a conductive or semiconductive sample for tunneling to occur between the tip and the sample surface. In this work, STM was used to characterize the growth of monometallic and bimetallic metal clusters, and study their morphology with changes in annealing temperature on the support.

2.6 Atomic Force Microscopy (AFM)

Atomic force microscopy (AFM) is another scanning probe technique similar to STM, however AFM can be used to measure both conductive and nonconductive samples. AFM does not require a vacuum environment and can be operated in air. Similar to STM, AFM utilizes a sharp tip to raster across the surface, but instead of measuring tunneling current, the force between the AFM tip and the sample surface is measured. The tip is connected to the end of a cantilever; when operated in non-contact mode, the cantilever oscillates at a given resonance frequency. When the tip comes close to a feature on the surface, forces from the sample interact with the cantilever, decreasing its resonance frequency. To maintain a constant oscillation frequency, the distance between the tip and sample most be adjusted. These height adjustments are used to create a topological map of the surface.[7] In the work here, AFM was used to evaluate full surface coverage, uniformity, and crystallite size of thin MOF films grown on a substrate.

2.7 Low Energy Electron Diffraction (LEED)

Low energy electron diffraction (LEED) can be used to determine the surface structure of single crystals or an ordered overlayer of films or adsorbates. A beam of low energy electrons is directed at the surface, and then backscattered onto a series of grids. Inelastically scattered electrons are filtered out, and those electrons which are elastically scattered are accelerated towards a phosphor screen creating a diffraction pattern of

bright spots due to the constructive interference of electron waves representing the periodicity of the surface being imaged.[8] The LEED pattern is a representation of reciprocal space; the distances between adjacent points in the LEED pattern are inversely proportional to the distances between points in the real surface.

Diffraction patterns can be used to view whether surface structures are ordered or if they have undergone reconstruction. In this work, LEED patterns were collected to establish the crystallinity of the TiO_2(110) and Pt(111) single crystal substrates used in experiments (Figure 2.7). It was also used to determine the structure of ZrO_2 and yttrium-ZrO_2 films.

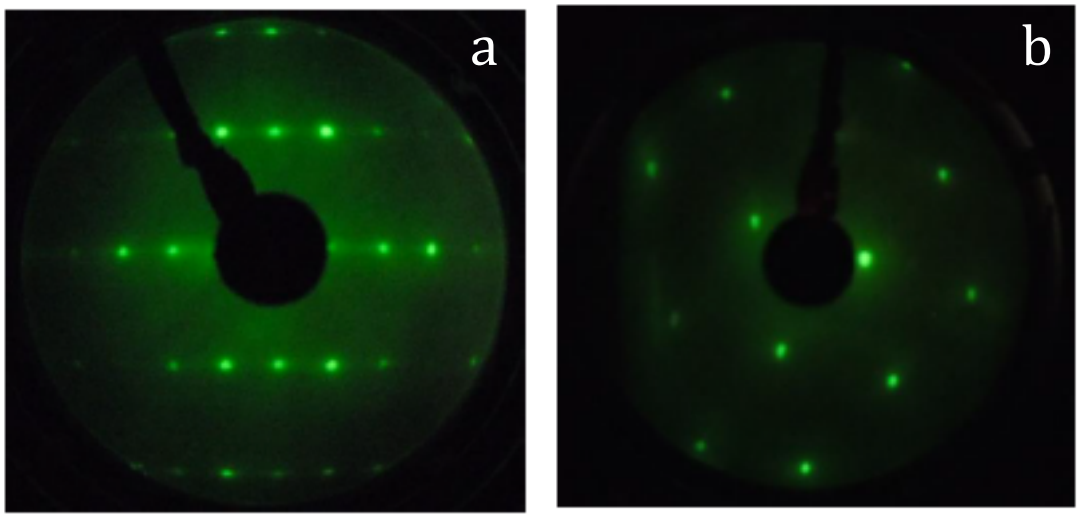

Figure 2.7: LEED patterns of a) TiO_2(110)-(1x1) and b) Pt(111).

2.8 Temperature Programmed Desorption (TPD)

Temperature programmed desorption (TPD) is a useful technique for studying the interaction of reaction gases with solid surfaces. It can be used to evaluate the number of active sites on a surface, as well as for understanding the mechanisms of adsorption, surface reaction, and desorption of molecules on surfaces.[9] The technique requires a mass spectrometer for detecting molecules and mass fragments after desorption. A TPD

experiment is conducted by cooling the sample to liquid nitrogen temperatures and saturating the surface with the gas or vapor of the molecule used in the analysis. The sample is placed in front of the mass spectrometer and heated at a linear rate. The desorbed molecules can be detected and quantified by the mass spectrometer. In this work, desorption as a function of temperature can provide information on the relative binding strength of molecules to different sites on the sample surface, and the relative number of adsorption sites in a sample. A typical TPD setup is shown in Figure 2.8.[10]

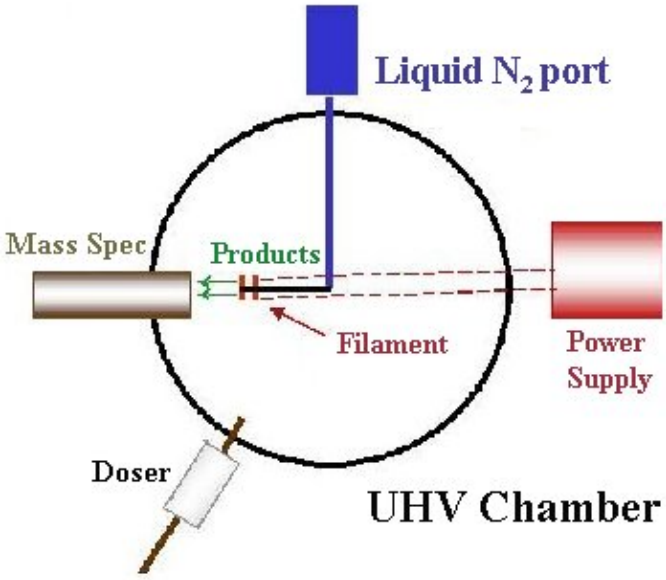

Figure 2.8: Diagram of temperature programmed desorption setup.[10]

2.9 Grazing Incidence Wide Angle X-ray Scattering (GIWAXS)

In a broad scope, small angle X-ray scattering (SAXS) is a powerful technique that can provide quantitative nanoscale information from a wide range of samples including liquids, pastes, powders, and films. It can operate in transmission or grazing incidence mode to measure the spatial arrangement of different interfaces and provide significant morphological details.[11] In the work done here, the technique was used for

analyzing thin films, therefore the X-ray beam was directed at an angle of grazing incidence to increase signal and eliminate the need for an X-ray transparent substrate. In grazing incidence wide angle X-ray scattering (GIWAXS), the incident beam has an increased interaction with the surface and the angle can be adjusted to probe only the top layer (~10 nm) or deeper film thicknesses. The scattered beam is collected by a 2D area detector; a schematic is illustrated in Figure 2.9.[12] When the detector is positioned at a

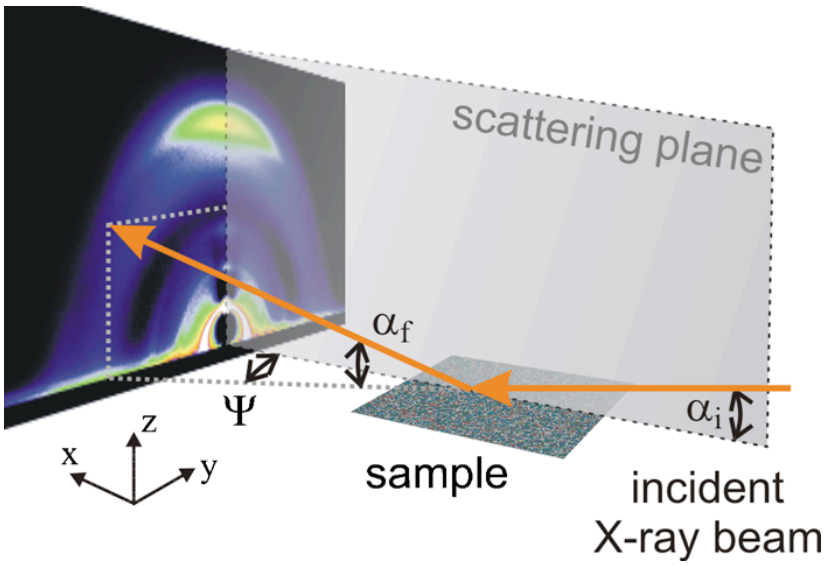

Figure 2.9: Schematic of incidence, scattering, and detection using GIWAXS.[12]

wide angle, information about the crystalline phase of the material can be collected. In this work, diffraction patterns were used to evaluate the crystallinity or degradation of the thin MOF films under study.

2.10 References

(1) Vickerman, J. C.; Gilmore, I. S. *Surface Analysis: The Principal Techniques*; 2nd ed.; John Wiley and Sons: Chichester, UK, 2009.

(2) Bvcrist; Carvalho, L. C. de. X-ray Photoelectron Spectroscopy https://commons.wikimedia.org/w/index.php?curid=7333849 (accessed May 8, 2019).

(3) Hoffmann, F. M. Infrared Reflection-Absorption Spectroscopy of Adsorbed Molecules. *Surf. Sci. Rep.* **1983**, *3*, 107.

(4) Tegeder, P. Optically and Thermally Induced Molecular Switching Processes at Metal Surfaces. *J. Phys. Condens. Matter* **2012**, *24*, 394001.

(5) Tenney, S. A.; Xie, K.; Monnier, J. R.; Rodriguez, A.; Galhenage, R. P.; Duke, A. S.; Chen, D. A. Novel Recirculating Loop Reactor for Studies on Model Catalysts: CO Oxidation on Pt/TiO_2(110). *Rev. Sci. Instrum.* **2013**, *84*, 104101.

(6) Schmid, M. Scanning Tunneling Microscopy https://commons.wikimedia.org/w/index.php?curid=180388 (accessed May 9, 2019).

(7) Gross, L.; Mohn, F.; Moll, N.; Liljeroth, P.; Meyer, G. The Chemical Structure of a Molecule Resolved by Atomic Force Microscopy. *Sciencee* **2009**, *325*, 1110–1114.

(8) *Surface Analysis Methods in Materials Science*; O'Connor, J.; Sexton, B.; Smart, R. S. C., Eds.; 2nd ed.; Springer-Verlag Berlin Heidelberg, 2003.

(9) Ishii, T.; Kyotani, T. Temperature Programmed Desorption. In *Materials Science and Engineering of Carbon*; Butterworth-Heinemann, 2016; pp. 287–305.

(10) Temperature Programmed Desorption - Wellesley College https://www.picswe.com/pics/temperature-programmed-38.html (accessed May 9, 2019).

(11) Feigin, L. A.; Svergun, D. I. *Structure Analysis by Small-Angle X-Ray and Neutron Scattering*; Taylor, G. W., Ed.; Plenum Press: New York and London, 1987.

(12) Perlich, J.; Rubeck, J.; Botta, S.; Gehrke, R.; Roth, S. V; Ruderer, M. A.; Prams, S. M.; Rawolle, M.; Zhong, Q.; Körstgens, V.; et al. Grazing Incidence Wide Angle X-Ray Scattering at the Wiggler Beamline BW4 of HASYLAB. *Rev. Sci. Instrum.* **2010**, *81*, 105105.

CHAPTER 3

WATER-GAS SHIFT ACTIVITY OF PT-RE CLUSTERS AND THE ROLE OF THE SUPPORT

3.1 Introduction

The field of heterogeneous catalysis has undergone many advances over the years, especially with the utilization of bimetallic catalysts.[1–4] Bimetallic catalysts have shown superior catalytic properties compared to their monometallic components by providing bifunctional sites to catalyze different reaction processes and through electronic interactions between the metals that lead to unique chemical activity.[5–7] Lately, bimetallic catalysts consisting of Pt and Re have become an attractive area of research for their excellent activity in several reactions relevant to biomass conversion. Aqueous phase reforming (APR) on bimetallic Pt-Re catalysts have exhibited excellent activity for converting biomass-derived molecules to fuels and chemicals. APR of glycerol over Pt-Re catalysts supported on carbon have shown an increase in turnover frequency (TOF) and longer lifetimes compared to monometallic Pt/C.[8–10] The increased activity of APR over Pt-Re/C catalysts has been attributed to decreased CO poisoning due to weaker binding of CO to the bimetallic surface.[9,11,12] Alternatively, the superior activity on Pt-Re catalysts has been explained by enhanced activity for the water-gas shift (WGS) reaction, which prevents CO poisoning by reaction with water to produce CO_2 and H_2.[13–16]

Previous investigations of the WGS activity on Pt-Re bimetallic catalysts have looked into the role Re plays in enhancing activity and extending the lifetime of the

catalyst.[13,15–19] Since the breaking of the O-H bond in water is believed to be the rate-limiting step in the WGS reaction on Pt,[20] it has been proposed that ReO_x provides the active sites for water dissociation on Pt-Re catalysts, leading to greater activity.[13,14,17] Hydrogenolysis of glycerol and other oxygenates is another reaction in which bimetallic Pt-Re catalysts have demonstrated an increased rate of activity over monometallic Pt catalysts, as well as enhancing selectivity toward internal hydrogenolysis to form higher value diols.[21,22] In this process, it has been proposed that ReO_x acts as a Bronsted acid site for dehydrogenation to aldehydes while Pt facilitates the rapid hydrogenation to the diol.[22] Other detailed studies investigating the role of Re have determined that CO binds less strongly to Pt-Re surfaces compared to Pt, and the enhanced activity is attributed to reduced CO poisoning on the bimetallic surfaces.[12,23–25] Another effect of the addition of Re to Pt catalysts has been found to result in greater Pt dispersion.[26–29] However, the support on which the metal particles are being grown has significant potential in influencing the size, composition, and electronic interactions of the metal clusters.

Metal-oxide supports such as TiO_2, CeO_2, and ZrO_2 have commonly been used as the support for Pt catalysts in the WGS reaction because of their reducible nature and ability to activate water.[20,30–33] It has been reported that TiO_2 reduction results in the creation of oxygen vacancies through reduction of the cation (Ti^{x+}, $x < 4$). It has then been proposed that these oxygen vacancies can form in the WGS reaction by reduction with CO over Pt/TiO_2, and serve as activate sites for water dissociation for hydroxyl and H_2 formation.[14,20,34–38] Nonetheless, inert supports such as carbon have been utilized with Pt-Re catalysts in which enhanced WGS reaction rates are attributed not to the support, but to the Pt-Re interactions upon alloy formation.[9,11] Even still, consideration must be

given to how the support may influence the chemical state, composition, and size of the metal particles. For instance, Re has been reported to interact strongly with oxide supports, given its oxophilic nature, compared to later transition metals such as Pt.[39–42]

Despite the increased interest in Pt-Re particles, only a handful of studies have specifically investigated their properties on different supports for the WGS reaction[14,30,43], and no direct comparison has been made of the influence Re has on Pt that may be dependent on the support. There are wide variations in the metal precursors, Pt/Re ratio, pretreatment conditions, and reaction parameters reported that can influence different factors such as metal oxidation state or extent of Pt-Re interaction, leading to conflicting results.[13,15,27,44,45] This work builds off our previous investigations on the growth[40] and activity[23] of Pt-Re clusters on TiO_2(110) in the WGS reaction by comparing cluster formation and chemical activity of Pt-Re particles on non-oxide supports. In our previous work[23,40], Re was found to interact strongly with the TiO_2 support, reducing Ti at room temperature. Bimetallic clusters of Pt and Re could be grown via either order of deposition at high coverages (2.0 ML Pt:1.7 ML Re), but the surface composition of the cluster was dependent on the order of sequential deposition. Using CO as a probe molecule, temperature programmed desorption (TPD) revealed that Pt deposited on top of Re, and low coverages of Re deposited on top of Pt, consisted of clusters with ~100% Pt at the surface. This was expected based on the lower surface free energy of Pt compared to Re, and the strong interaction of Re with the support. However, at high coverages of Re deposited on top of Pt, the amount of Re that can diffuse subsurface is kinetically limited, and the surface consisted of both Re and Pt.[40] For the WGS activity studies of Pt-Re clusters on TiO_2(110), Re was found to be inactive for the reaction, whereas

bimetallic surfaces of Pt on Re exhibited greater activity for the WGS reaction than pure Pt.[23] These bimetallic surfaces were prepared either by a Re core-Pt shell structure of 2 ML Pt deposited on 2 ML Re, or 0.5 ML Re deposited on 2 ML Pt in which the Re diffused subsurface leaving a layer of Pt on top. Furthermore, bimetallic clusters containing ReO_x proved to have lower activity than Pt-Re clusters containing metallic Re, ruling out ReO_x as an active site for the WGS reaction.[23]

In this work, Pt-Re surfaces are prepared on a nonreactive support of highly oriented pyrolytic graphite (HOPG) and on a Pt(111) single crystal to decouple metal-metal interactions and metal-support interactions. UHV techniques evaluate the cluster growth and surface composition, while reactor experiments assess their catalytic activity for the WGS reaction. A comparison is drawn between these studies and our previous work on Pt-Re surfaces supported by $TiO_2(110)$[23] in order to understand the influence of the support on the morphology, composition, and activity of the prepared model catalysts. Scanning tunneling microscopy (STM) provides information on the cluster size and bimetallic nature of the clusters, dependent on which support is used. CO TPD determines the surface composition of the Pt-Re particles and the dependence on metal deposition order for their bimetallic nature. WGS experiments are carried out in a specially designed microreactor coupled to the UHV chamber operating at ~1 atm. Reactor experiments show that activity is lower for clusters grown on HOPG and Pt(111) than the TiO_2 support, but that Pt with subsurface Re catalysts produce the greatest activity regardless of the support being used. The enhanced activity on the $TiO_2(110)$ support is further investigated by studying the relationship between interfacial sites of Pt/TiO_2 and TOF as a function of Pt coverage. It is shown that as the ratio of

perimeter/surface sites increases, the TOF increases at a very comparable rate; thus, providing insight on the bifunctional nature of the metal-support interface for the WGS reaction.

3.2 Experimental

Experiments were conducted in two ultrahigh vacuum chambers that have previously been described. The first chamber[23,46] operates at a base pressure < 2 x 10^{-10} Torr and is coupled to a microreactor.[47] It is equipped with a residual gas analyzer (Stanford Research Systems, RGA 300), a hemispherical analyzer (SPECS EA10) and Mg/Al Kα X-ray source (Leybold Heraeus, RQ 20/63) for XPS measurements. The chamber also includes an infrared reflection absorption spectroscopy (IRAS) system (Bruker, Tensor 27) with external liquid nitrogen-cooled mercury cadmium telluride (LN-MCT) detector. The second ultrahigh vacuum chamber[40,48–50] has been described previously and operates with a base pressure < 2 x 10^{-10} Torr. It is equipped with a variable-temperature scanning tunneling microscope (Omicron VT-25), a hemispherical analyzer (Omicron EA125) for X-ray photoelectron and low energy ion scattering spectroscopies, optics for low energy electron diffraction and Auger electron spectroscopy (Omicron Spec 3), and a quadrupole mass spectrometer (Leybold-Inficon, Transpector 2) for TPD measurements.

The HOPG supports (SPI Supplies, 10 mm x 10 mm x 1 mm) used in each chamber were mounted onto a Ta plate using thin Ta foil straps. Before preparing each sample, the surface of the HOPG support was cleaned by cleaving with adhesive tape. Clean HOPG was introduced to the vacuum chamber via a load lock cell and transferred to a sample holder within the chamber after sufficient evacuation of the load lock. For

each experiment, the HOPG surface was sputtered to create defects for metal nucleation using Ar^+ ions at 500 eV and a current of 0.1 μA for 5 minutes. The HOPG support was then heated by electron bombardment using a tungsten filament positioned behind the sample plate to 950-1000 K for 12 minutes (3 cycles of 4 min) to remove embedded Ar. The support temperature was monitored by an infrared pyrometer (Heitronics) and type K thermocouple spotwelded to the edge of the back plate in the second chamber. The Pt(111) single crystal (99.999%, Princeton Scientific Corp., 8 mm diameter, 2 mm thickness) was mounted by press-fitting two Ta wires into 1.1 mm deep slots cut into the sides of the crystal. The Ta wires were spot-welded onto a standard Omicron sample plate with an 8.9 x 8.9 mm^2 window so that the back of the crystal could be directly heated by electron bombardment from the tungsten filament. The rutile TiO_2(110) crystal (Princeton Scientific Corporation, 10 mm x 10 mm x 1 mm) was mounted on a Ta back plate using thin Ta foil straps. The Pt(111) and TiO_2 crystals were cleaned by Ar^+ ion sputtering at 1 kV for 20 min, followed by annealing to 950-1000 K for 3 min. The support temperature was monitored by an infrared pyrometer (Heitronics). Metal clusters of Pt and Re were grown by vapor deposition in both chambers from a Pt rod (ESPI, 2 mm diameter, 99.95%) and a Re rod (ESPI, 2 mm diameter, 99.99%) using a four-pocket electron-beam evaporator (Oxford Applied Research, EGCO4). Pt and Re metal were deposited sequentially onto the support surface at a rate of approximately 0.08-0.1 ML/min, with one monolayer (ML) being defined as the packing density of Pt(111) (1.50 x 10^{15} atoms/cm^2) or Re(0001) (1.52 x 10^{15} atoms/cm^2). The metal flux was calibrated in each chamber with a UHV bakeable quartz crystal microbalance (QCM, Inficon, XTM-2) before deposition. Fresh surfaces were prepared for each experiment.

Samples were prepared in the first UHV chamber and then directly transferred into the microreactor without exposure to air. The experiments were conducted in a feed gas mixture of 3% CO (Praxair)/ 7% H_2O/ 90% He (Airgas, 99.999%) at a flow rate of 60 SCCM determined by a digital flow meter (Agilent Technologies, ADM2000). CO and He were introduced via independently calibrated mass flow controllers (Brooks, 5850e and 5850i). Water vapor was introduced to the feed gas by a stainless steel vapor-liquid equilibrator (VLE) consisting of ultrapure liquid water (18.2 MΩ resistivity, Barnstead EasyPure II 7138), with He being the sweep gas. The temperature of the VLE was controlled by a cooling/heating recirculation bath (VWR), and the concentration of water vapor was configured using the vapor pressure calculated from the Antoine equation. The samples were heated in a continuous flow of the feed gas to a temperature of 160 °C at a rate of 2.0 °C/min by heating tape (Briskheat, BWHD) wrapped around the exterior of the reactor housing. To ensure uniform heating and cooling, the heating tape was regulated by a feedback loop on a temperature controller (Auber, SYL-4342P). The temperature of the sample was measured by a type K thermocouple (Omega, KMQSS-040G-6) welded into the feed gas inlet close to the surface of the sample. The gas lines were heated to a temperature of 65 °C using Valco Instruments temperature controllers. The pressures within the reactor and lines were measured by two capacitance manometers (MKS Instruments, Baratron 722A), one located upstream of the reactor in the feed gas line (790-800 Torr) and one downstream of the reactor (770-780 Torr). The reaction was operated in recirculation mode in which the reactant gases are recirculated over the catalyst surface once every 2 min, allowing the CO_2 concentration to increase to a detectable level during the recirculation period. An in-line gas sample (~1.096 cm^3) was

injected into the gas chromatograph (HP 5890A) equipped with a PoraPLOT Q capillary column and thermal conductivity detector (TCD) using He as the carrier gas. The initial oven temperature of the GC was kept at 70 °C for 2 minutes, then increased to 180 °C at a rate of 15 °C/min and held there for 5 minutes. The detector temperature was maintained at 200 °C. Automatic injections occurred every 20 minutes and were followed by refilling the gas sampling loop with fresh feed gas so that the pressure in the reactor remained unchanged. The activity was recorded for a reaction time of 2 hours. The total moles of CO_2 produced was corrected for the loss of CO_2 during gas injections by assuming ideal gas behavior. The background activity of the empty reactor and sample support were found to contribute minor amounts of CO_2 to the overall activity and were subtracted from the total activity.

Due to the reactor's direct coupling to the UHV chamber, XPS measurements were collected before and after reactor experiments without exposing the sample to air. A dwell time of 0.2 seconds and step size of 0.025 eV were used for C(1s), O(1s), Re(4f), Pt(4f), and Ti(2p) regions. A survey scan was also collected to ensure there were no contaminants before or after the reaction.

The second chamber was used to conduct all STM and TPD measurements. STM experiments were conducted using an Omicron VT-25 collected at constant tunneling current of 0.1-0.2 nA and a sample bias of +2.3 V with respect to the STM tip. STM tips were made by electrochemically etching a 0.38 mm diameter tungsten wire in NaOH. The tips were conditioned by sputtering with Ar^+ ions at 3 kV and pulsing to higher voltages. Cluster heights on HOPG were determined by the manual measurement of 30 clusters; cluster heights of submonolayer Pt coverages on TiO_2 were determined using an

in-house program that measured all clusters in a 1000 Å x 1000 Å region.[51,52] Cluster heights are used as a measure of cluster size since the diameters are known to be overestimated due to tip convolution effects.[53,54] Cluster densities were measured by counting all the clusters in a 1000 Å x 1000 Å image.

TPD experiments were carried out by exposing the surfaces to CO (99.998%, Matheson) via a stainless steel directed dosing tube. A saturation exposure of CO was achieved by leaking in CO to a pressure rise of 5.0 x 10^{-10} Torr for 3 min. The sample was heated at a rate of ~2 K/s using an automated ramp program while the temperature was monitored using a type K thermocouple spot welded to the Ta back plate. During TPD experiments, the mass spectrometer was linearly translated toward the chamber so that the sample was positioned ~2 mm in front of a 4.3 mm hole at the end of the tube (7.6 mm length) attached to the shroud of the mass spectrometer in order to minimize the detection of products desorbing from the sample holder.

3.3 Results

Monometallic and bimetallic clusters of Pt and Re are studied on a support of HOPG and a metal single crystal of Pt(111) in order to compare with our previous results for Pt-Re surfaces prepared on TiO_2(110). Experiments are designed so as to understand the role of metal-support interactions on cluster growth and catalytic activity in the WGS reaction.

HOPG was chosen as a support to distinguish between possible affects arising from metal clusters interacting with an oxide support such as TiO_2. HOPG has been reported to have very little or no interaction with metals.[55–58] Because of the weak interaction, metal atoms on HOPG have a high mobility, and form large clusters with low

cluster densities when metals are deposited on the untreated HOPG surface. However Ar ion sputtering can be used to introduce defects on the HOPG surface to decrease the cluster size and increase the cluster density.[59–61] Figure 3.1 shows STM images of 2 ML Re and 2 ML Pt on HOPG deposited after sputtering the clean HOPG surface for 5 min at 0.1 μA and 500 eV. In both cases, the metal clusters almost completely cover the surface, but the average cluster heights are much larger on HOPG compared to the same coverages on TiO_2: 13.7±2.3 Å vs. 4.7±1.0 Å for Re and 22.3±3.2 Å vs. 13.2±2.3 Å for Pt.[40] When 2 ML Pt are deposited on 2 ML Re, the average cluster height increases to 18.0±2.4 Å while the cluster density decreases, indicating that the Pt atoms join existing

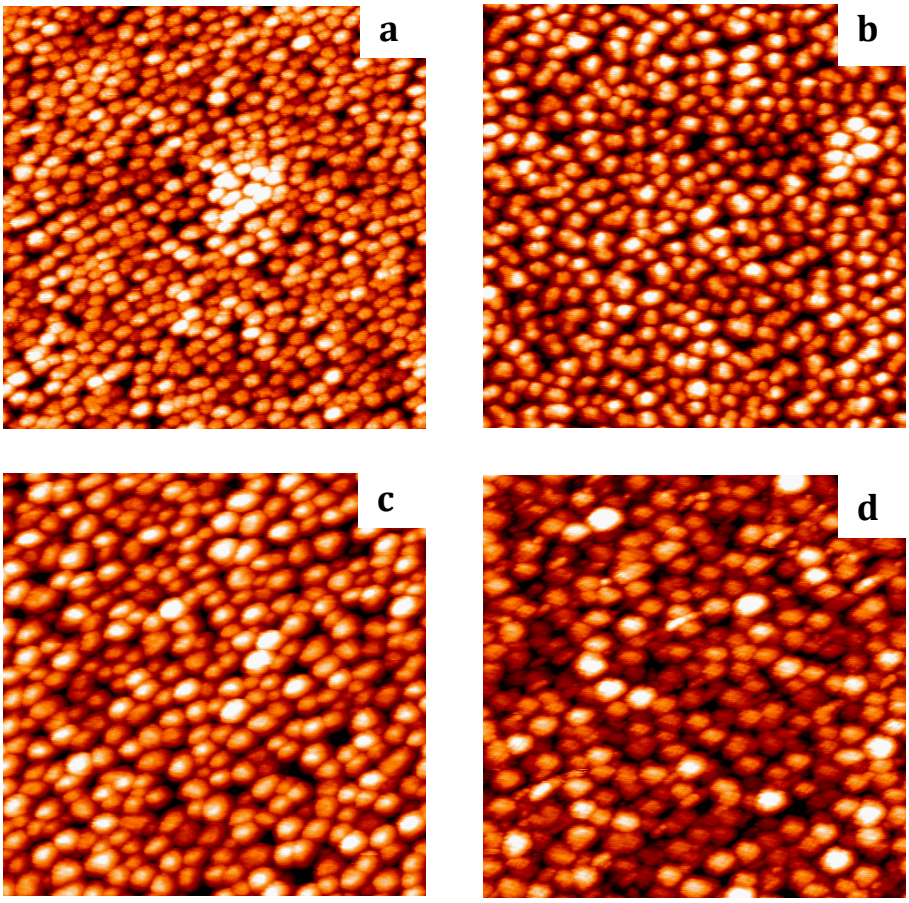

Figure 3.1: Scanning tunneling microscopy images for the following metal coverages on HOPG: a) 2 ML Re; b) 2 ML Re + 2 ML Pt; c) 2 ML Pt; d) 2 ML Pt + 2 ML Re. All images are 1000 Å x 1000 Å.

Re clusters to form exclusively bimetallic clusters on the surface. In contrast, when 2 ML Re are deposited on 2 ML Pt, the lower mobility of Re compared to Pt results in the formation of new, pure Re clusters. In this case, the cluster density increases after Re deposition, and the average cluster size decreases.

Surface compositions of the HOPG-supported clusters were probed in CO TPD experiments. Since CO dissociates on Re but not on Pt, the presence of a high temperature CO desorption peak from dissociation of CO and subsequent recombination of carbon and oxygen atoms illustrates the presence of Re at the surface. Figure 3.2 shows the CO desorption profiles of pure 2 ML Pt and 2 ML Re, where only a low temperature desorption peak around 460 K is observed on Pt, but peaks at 415 K and 845 K are observed on Re. For the exclusively bimetallic 2 ML Re + 2 ML Pt clusters, there

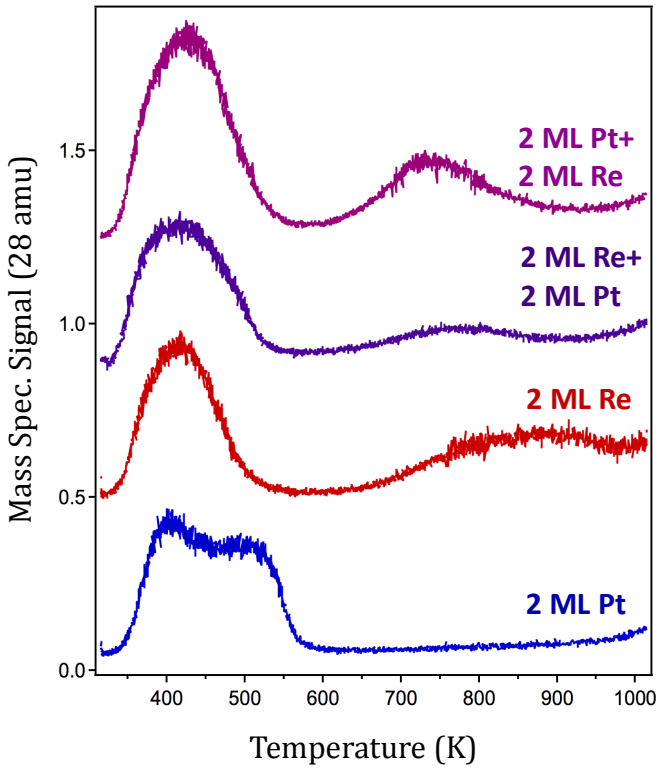

Figure 3.2: Temperature programmed desorption data for CO adsorbed at room temperature on various metal clusters on HOPG.

is a relatively small high temperature desorption peak which demonstrates that Re is present at the cluster surface. This behavior is in contrast to 2 ML Re + 2 ML Pt clusters on TiO_2, where the bimetallic clusters have only Pt at the surface;[23] the lower surface free energy of Pt (2.5 J/m^2) compared to Re (3.6 J/m^2) makes it thermodynamically favorable for Pt to reside at the surface.[62] Although Pt and Re can alloy at all compositions[62] and are likely intermixed in the clusters, given the stronger interaction of oxophilic Re with TiO_2 compared to HOPG it is not surprising that more Re remains at the interface with TiO_2. For the 2 ML Pt + 2 ML Re clusters, there is a substantial high temperature desorption peak at 740 K, indicating a significant fraction of Re resides at the surface either from Re atoms that did not diffuse into the Pt clusters or from Re atoms that exist at the surface of pure Re clusters.

Activity for the WGS reaction (3% CO + 7% H_2O + 90% He) is carried out on pure and bimetallic clusters of Pt and Re in a UHV-coupled microreactor at ~1 atm and 160 °C. At this temperature, cluster sintering should be minimal based on earlier STM work studying monometallic and bimetallic Pt-Re surfaces annealed to 800 K.[40] The occurrence of adsorbate-induced diffusion of Re to the surface during reaction was not found to take place. Unlike surface aggregation of Pt in Pt-Au[63] or Re in Pt-Re[64] in the presence of methanol or oxygen, the WGS reaction environment is not substantially oxidizing, and compositional changes are not observed. A comparison of TOFs for the WGS reaction on HOPG-supported clusters vs. TiO_2-supported clusters is shown in Figure 3.3. The number of sites for each surface was determined by CO desorption relative to the Pt(111) surface, which has a known surface area by geometry and packing density. Comparing the pure Pt clusters on HOPG to those on TiO_2, the TOF for 2 ML

Pt/HOPG is only 60% of that for 2 ML Pt/TiO_2. This result demonstrates that the titania support plays a significant role in the activity of the Pt clusters for the WGS reaction. For the Re clusters on both supports, the lack of activity is consistent with Re being inactive for the WGS reaction.[17,65] For the 2 ML Re + 2 ML Pt clusters, these surfaces consist of mainly Pt sites at the surface with Re in the subsurface. On HOPG, the Pt on Re clusters have a TOF that is 1.4 times higher than Pt alone, and on TiO_2, the TOF is 1.7 times greater. Therefore, in both cases the presence of subsurface Re enhances the activity. The smaller enhancement on HOPG could be due to the fact that a larger fraction of Re exists at the cluster surface based on the CO TPD results. The 2 ML Pt + 2 ML Re

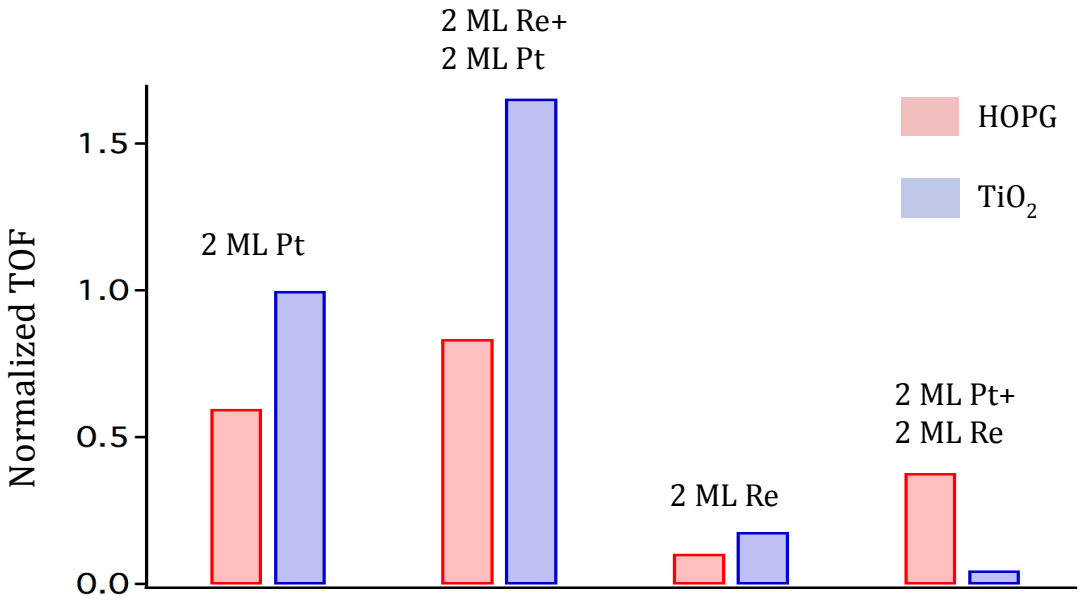

Figure 3.3: Comparison of TOFs for the WGS reaction at 160 °C on various metal clusters on HOPG (red) and TiO_2(110) (blue). All values are normalized to the TOF for 2 ML Pt on TiO_2(110).

clusters on TiO_2 have almost no activity due to a higher Re composition at the surface of the bimetallic clusters.[23] On HOPG, these clusters also have relatively low activity, but the TOF is still 60% of that for Pt/HOPG. Although these also have a large fraction of Re at the surface, the fact that monometallic Re clusters are present means that some of

the Re atoms are not incorporated into the existing Pt clusters on HOPG. Therefore, the fraction of active Pt sites covered by Re should be lower on HOPG compared to on TiO_2.

To further explore the role of the support, Pt-Re alloy surfaces on Pt(111) were investigated in order to completely remove any effects that may be coming from the support. One alloy surface was prepared by depositing 2.4 ML Re on Pt(111) and then annealing to 1000 K for 5 min, which causes the Re atoms to diffuse into the bulk, resulting in a pure Pt surface with Pt and Re alloyed in the subsurface.[24,66] Another surface was prepared by depositing a 1 ML Re film on Pt(111) and then 1 ML Pt on top

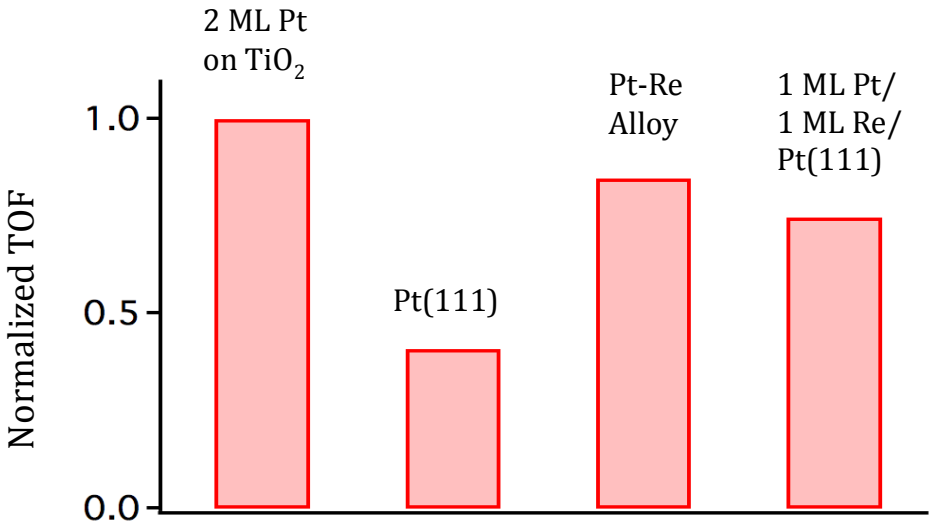

Figure 3.4: Comparison of TOFs for the WGS reaction at 160 °C on the designated surfaces. All values are normalized to the TOF for 2 ML Pt on TiO_2(110).

of the Re layer. In both cases, Pt on Re surfaces are formed, which have shown to be more active for the WGS reaction than Pt alone when supported by HOPG or TiO_2.[23] A comparison of TOFs is presented in Figure 3.4. The TOF for Pt(111) is only 40% of that for 2 ML Pt/TiO_2. Again, higher activity is seen for Pt clusters on TiO_2, compared to Pt on HOPG or pure Pt(111). This suggests that either TiO_2 itself promotes WGS activity through reaction at interfacial sites,[37] or the reaction is promoted at undercoordinated

edge sites,[67] which are more prevalent on the smaller clusters on TiO_2. The Pt-Re alloy surfaces are approximately twice as active as Pt(111), which is consistent with the higher activity seen for Pt on Re clusters, but still less active than Pt/TiO_2.

In order to better understand the role of cluster-titania interactions taking place in the WGS reaction, the activity of Pt clusters supported on $TiO_2(110)$ has been investigated as a function of increasing metal coverage. Figure 3.5 shows STM images for Pt coverages of 0.13 ML, 0.25 ML, and 0.75 ML on TiO_2. As the coverage increases, the average cluster height increases from 5.2±1.7 Å to 6.2±2.1 Å to 9.3±3.1 Å. However, the number of clusters on the surface initially increases from $1.02x10^{13}$ to $1.13x10^{13}$ and then decreases to $7.12x10^{12}$ clusters/cm^2 as the clusters coalesce to form larger particles

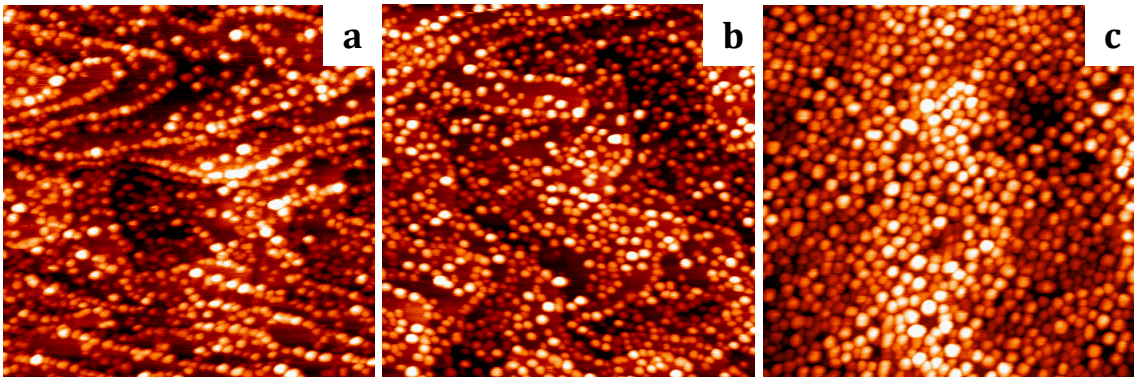

Figure 3.5: Scanning tunneling microscopy images for the following coverages of Pt on $TiO_2(110)$: a) 0.13 ML; b) 0.25 ML; c) 0.75 ML. All images are 1000 Å x 1000 Å.

at the higher coverage. Since cluster diameters are known to be overestimated in STM images due to tip convolution effects,[68] the true cluster diameters were estimated based on: a paraboloid cluster shape; the measured heights; the cluster density; and an accurate total coverage, which was measured with a quartz crystal microbalance. From the estimated true cluster diameters, the fraction of perimeter atoms/total surface atoms was calculated to be 44% for 0.13 ML, 35% for 0.25 ML, and 19% for 0.75 ML. Using CO

desorption experiments, the total number of Pt sites on surfaces with Pt coverages ranging from 0.13 ML to 2 ML was determined. These values are compared with the activity found for the WGS reaction as a function of the Pt coverage (Figure 3.6a); the values for the total number of sites and activity are normalized to that of 2 ML Pt. Although both activity and number of surface sites increase with Pt coverage, the activity/surface site is higher at submonolayer coverage. A plot of the turnover frequency (activity/surface site) and perimeter sites/surface sites as a function of Pt coverage is

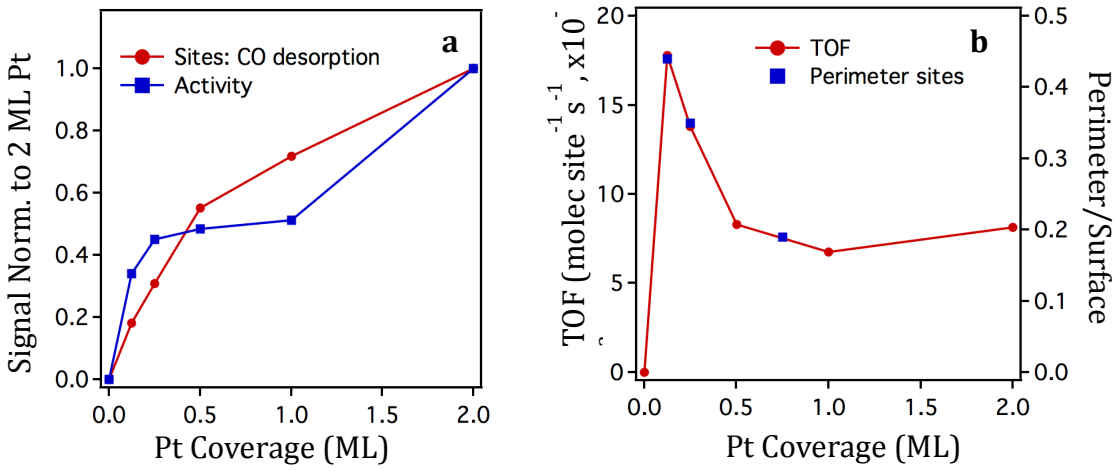

Figure 3.6: a) Number of active sites determined from CO desorption experiments (red) and activity for WGS at 160 °C (blue) as a function of Pt coverage on TiO_2(110). Both values are normalized to that of 2 ML Pt/TiO_2; b) TOF for WGS reaction at 160 °C (red, left axis) and the fraction of perimeter sites/total surface sites (blue, right) as a function of Pt coverage.

shown in Figure 3.6b. This plot illustrates that these two values have the same dependence on coverage and strongly suggests that reaction at perimeter atoms dominates the overall activity. These results are consistent with reports in the literature that propose WGS activity on noble metal clusters on TiO_2 occurs at the cluster-support interface.

3.4 Discussion

Pt-Re Interactions

In the WGS reactor experiments that take place in atmospheric pressures at 160 °C, bimetallic surfaces consisting of Pt on top of Re are found to have enhanced activity over monometallic Pt surfaces for both Pt clusters on HOPG and and the pure Pt(111) single crystal. Our previous catalytic studies of Pt-Re clusters on the TiO_2(110) support are in agreement with the results of Pt on Re surfaces having greater activity over Pt alone.[23] This consistent outcome for three different catalyst supports indicates that the enhanced activity of Pt surfaces with Re addition is not dependent on the support, but influenced by Pt-Re interactions.

The WGS reaction has a number of proposed mechanisms by which H_2O is activated and CO is adsorbed to form CO_2 and H_2. Water dissociation on pure Pt is not facile,[69] and it is generally accepted that OH bond scission in H_2O is an important step in the WGS reaction.[70–72] Some reports in the literature discuss ReO_x as a potential active site for water dissociation.[13,17] However, in our work conducted previously for clusters supported on TiO_2 it was found that ReO_x did not form under reaction conditions when starting with metallic Re, and that Re intentionally oxidized prior to reaction was less active in the WGS reaction than metallic Re.[23] As an alternative explanation, density functional theory (DFT) calculations determined that CO binds less strongly to Pt-Re surfaces compared to pure Pt, decreasing the chance for active Pt sites to become blocked by strongly bound CO molecules.[23] Additionally, IRAS experiments carried out after the WGS reaction confirmed that the CO coverage on Pt was greater than on Pt-Re,[23]

demonstrating that the reason behind the enhanced activity of the bimetallic Pt on Re surface is due to decreased CO poisoning.

Role of the Support

Activity studies on monometallic Pt surfaces on different supports revealed that Pt clusters on TiO_2(110) have a greater TOF than Pt supported on HOPG and the Pt(111) single crystal. The TOF takes into account the number of active sites available for reaction, thus the increased activity seen on TiO_2 supported Pt is not due to a greater number of active sites. Therefore, there is strong indication that contribution to the reaction is coming from the support. From reports in the literature, the metal-oxide interface is believed to play an important role in facilitating the WGS reaction on oxide-supported metal clusters.[67,71,73,74] In our studies of different Pt coverages on the TiO_2(110) support, the TOF is greatest at the highest ratio of perimeter/surface sites; additionally, the trend in TOF values appears to coincide closely with the perimeter/surface site ratio at submonolayer coverages. An experimental study by Kondarides et al.[30] found that Pt supported on reducible oxide supports such as TiO_2, CeO_2, and La_2O_3 exhibited significantly higher activity than on irreducible oxides such as Al_2O_3, MgO, and SiO_2. They attributed the higher activity to the ability of the support to more readily participate in the regenerative "redox" mechanism for the WGS reaction in which CO molecules adsorbed on Pt are oxidized by oxygen originating from the support, which in turn is oxidized by water. This bifunctional effect between the support and Pt particles is also supported by computational studies from Ammal et al.[20] Their calculations showed that Pt cluster edge sites on TiO_2(110) are more active than Pt terrace sites for the WGS reaction; stating the CO-promoted redox mechanism as the

dominant reaction pathway in which CO adsorbed to Pt is oxidized by oxygen in the TiO_2 support, creating an oxygen vacancy that is re-oxidized by H_2O.[20] Our findings of enhanced activity of Pt on the TiO_2(110) support compared to Pt on HOPG and the Pt(111) single crystal are in accordance with the rationale and findings presented in the literature.

It should be noted that the TOF as a function of particle size of Pt was not investigated for other supports besides TiO_2(110) in this work. It cannot be completely ruled out that the increasing TOF with increasing perimeter/surface sites is not also influenced by the decreasing Pt particle size; meaning more undercoordinated Pt atoms are available for reaction. However, a study by Ciftci et al.[75] examined the influence of Pt particle size on a carbon support on the catalytic activity for the WGS reaction. Utilizing a carbon support eliminated any possible contribution coming from the metal-support interface during the reaction. Their investigation did not find an increase in activity with decreasing particle size. Among Pt cluster sizes of 1.2, 1.6, 2.0 and 4.2 nm, the intermediate particle size of 2.0 nm showed the greatest TOF. Thus, it can be gathered that the increase in TOF with decreasing particle size is not dependent on the number of undercoordinated sites, but attributed to the increase in ratio of Pt perimeter sites interfaced with the TiO_2 support. The pathway by which Pt metal clusters at the interface of TiO_2 facilitates the WGS reaction has been studied in experimental and theoretical reports, and indicate it is the bifunctional nature of the Pt-TiO_2 interface that leads to enhanced activity compared to Pt clusters on HOPG or a Pt(111) single crystal support.

3.5 Conclusions

Pt-Re clusters on HOPG and Pt-Re alloy surfaces on Pt(111) were investigated in comparison to previous experiments for Pt-Re clusters on TiO_2(110) to understand the role of the support in the WGS reaction. Activity studies for the WGS experiment conducted at 160 °C resulted in Pt on Re surfaces supported by HOPG and Pt-Re alloys on Pt(111) both having higher activity than Pt alone on HOPG and pure Pt(111), respectively. This outcome is consistent with greater activity for Pt on Re surfaces supported by TiO_2(110), thus supporting the conclusion that bimetallic Pt on Re surfaces have enhanced activity for the WGS reaction regardless of the support being used. Further investigations into the role of the support demonstrated that Pt on TiO_2 had a greater TOF than Pt supported on HOPG and a pure Pt(111) single crystal. This indicated that the titania support was playing a role in the reaction. Metal-support interactions between Pt clusters and the TiO_2 support were studied by focusing on the correlation between WGS activity and Pt coverage. A comparison of the TOF and the ratio of perimeter/surface sites as a function of Pt coverage illustrated that both values follow extremely similar trends and have the same dependence on coverage. These results signify that the cluster-support interface for Pt-TiO_2(110) is playing a role in facilitating the WGS reaction.

Acknowledgements

Thank you to Thathsara Maddumapatabandi for the STM images and CO TPD measurements. Acknowledgment of funding is owed to the National Science Foundation (CHE 1300227) and National Science Foundation IGERT (DGE 1250052).

3.6 References

(1) Toshima, N.; Yonezawa, T. Bimetallic Nanoparticles - Novel Materials for Chemical and Physical Applications. *New J. Chem* **1998**, *22*, 1179–1201.

(2) Sankar, M.; Dimitratos, N.; Miedziak, P. J.; Wells, P. P.; Kiely, C. J.; Hutchings, G. J. Designing Bimetallic Catalysts for a Green and Sustainable Future. *Chem. Soc. Rev* **2012**, *41*, 8099–8139.

(3) Singh, A. K.; Xu, Q. Synergistic Catalysis over Bimetallic Alloy Nanoparticles. *ChemCatChem* **2013**, *5*, 652–676.

(4) Guczi, L. Bimetallic Nano-Particles: Featuring Structure and Reactivity. *Catal. Today* **2005**, *101*, 53–64.

(5) Sinfelt, J. H. *Bimetallic Catalysts. Discoveries, Concepts, and Applications*; John Wiley and Sons: New York, 1983.

(6) Rodriguez, J. Physical and Chemical Properties of Bimetallic Surfaces. *Surf. Sci. Rep.* **1996**, *24*, 223–287.

(7) Campbell, C. Bimetallic Surface Chemistry. *Annu. Rev. Phys. Chem.* **1990**, *41*, 775–837.

(8) Simonetti, D. A.; Kunkes, E. L.; Dumesic, J. A. Gas-Phase Conversion of Glycerol to Synthesis Gas over Carbon-Supported Platinum and Platinum-Rhenium Catalysts. *J. Catal.* **2007**, *247*, 298–306.

(9) Kunkes, E. L.; Simonetti, D. A.; Dumesic, J. A.; Pyrz, W. D.; Murillo, L. E.; Chen, J. G.; Buttrey, D. J. The Role of Rhenium in the Conversion of Glycerol to Synthesis Gas over Carbon Supported Platinum-Rhenium Catalysts. *J. Catal.* **2008**, *260*, 164–177.

(10) Ciftci, A.; Ligthart, D. A. J. M.; Sen, A. O.; van Hoof, A. J. F.; Friedrich, H.; Hensen, E. J. M. Pt-Re Synergy in Aqueous-Phase Reforming of Glycerol and the Water-Gas Shift Reaction. *J. Catal.* **2014**, *311*, 88–101.

(11) Ciftci, A.; Eren, S.; Ligthart, D.; Hensen, E. J. M. Platinum-Rhenium Synergy on Reducible Oxide Supports in Aqueous-Phase Glycerol Reforming. *ChemCatChem* **2014**, *6*, 1260–1269.

(12) Ishikawa, Y.; Liao, M.; Cabrera, C. R. Energetics of H_2O Dissociation and CO_{Ads}+ OH_{Ads} Reaction on a Series of Pt-M Mixed Metal Clusters: A Relativistic Density-Functional Study. *Surf. Sci.* **2002**, *513*, 98–110.

(13) Azzam, K. G.; Babich, I. V.; Seshan, K.; Mojet, B. L.; Lefferts, L. Stable and Efficient Pt-Re/TiO_2 Catalysts for Water-Gas-Shift: On the Effect of Rhenium. *ChemCatChem* **2013**, *5*, 557–564.

(14) Azzam, K. G.; Babich, I. V.; Seshan, K.; Lefferts, L. Bifunctional Catalysts for

Single-Stage Water-Gas Shift Reaction in Fuel Cell Applications. Part 1. Effect of the Support on the Reaction Sequence. *J. Catal.* **2007**, *251*, 153–162.

(15) Sato, Y.; Terada, K.; Hasegawa, S.; Miyao, T.; Naito, S. Mechanistic Study of Water-Gas-Shift Reaction over TiO_2 Supported Pt-Re and Pd-Re Catalysts. *Appl. Catal. A Gen.* **2005**, *296*, 80–89.

(16) Iida, H.; Igarashi, A. Difference in the Reaction Behavior between Pt-Re/TiO_2 (Rutile) and Pt-Re/ZrO_2 Catalysts for Low-Temperature Water Gas Shift Reactions. *Appl. Catal. A Gen.* **2006**, *303*, 48–55.

(17) Azzam, K. G.; Babich, I. V.; Seshan, K.; Lefferts, L. Role of Re in Pt-Re/TiO_2 Catalyst for Water Gas Shift Reaction: A Mechanistic and Kinetic Study. *Appl. Catal. B Environ.* **2008**, *80*, 129–140.

(18) Iida, H.; Yonezawa, K.; Kosaka, M.; Igarashi, A. Low-Temperature Water Gas Shift Reaction over Pt-Re/TiO_2 Catalysts Prepared by a Sub-Critical Drying Method. *Catal. Commun.* **2009**, *10*, 627–630.

(19) Gonzalez, I. D.; Navarro, R. M.; Wen, W.; Marinkovic, N.; Rodriguez, J. A.; Rosa, F.; Fierro, J. L. G. A Comparative Study of the Water Gas Shift Reaction over Platinum Catalysts Supported on CeO_2, TiO_2 and Ce-Modified TiO_2. *Catal. Today* **2010**, *149*, 372–379.

(20) Walker, E. A.; Mitchell, D.; Terejanu, G. A.; Heyden, A. Identifying Active Sites of the Water−Gas Shift Reaction over Titania Supported Platinum Catalysts under Uncertainty. *ACS Catal.* **2018**, *8*, 3990–3998.

(21) Daniel, O. M.; DeLaRiva, A.; Kunkes, E. L.; Datye, A. K.; Dumesic, J. A.; Davis, R. J. X-Ray Absorption Spectroscopy of Bimetallic Pt-Re Catalysts for Hydrogenolysis of Glycerol to Propanediols. *ChemCatChem* **2010**, *2*, 1107–1114.

(22) Falcone, D. D.; Hack, J. H.; Klyushin, A. Y.; Knop-Gericke, A.; Schlögl, R.; Davis, R. J. Evidence for the Bifunctional Nature of Pt−Re Catalysts for Selective Glycerol Hydrogenolysis. *ACS Catal.* **2015**, *5*, 5679–5695.

(23) Duke, A. S.; Xie, K.; Brandt, A. J.; Maddumapatabandi, T. D.; Ammal, S. C.; Heyden, A.; Monnier, J. R.; Chen, D. A. Understanding Active Sites in the Water-Gas Shift Reaction for Pt-Re Catalysts on Titania. *ACS Catal.* **2017**, *7*, 2597–2606.

(24) Ramstad, A.; Strisland, F.; Raaen, S.; Borg, A.; Berg, C. CO and O_2 Adsorption on the Re/Pt(111) Surface Studied by Photoemission and Thermal Desorption. *Surf. Sci.* **1999**, *440*, 290–300.

(25) Greeley, J.; Mavrikakis, M. Near-Surface Alloys for Hydrogen Fuel Cell Applications. *Catal. Today* **2006**, *111*, 52–58.

(26) Fung, A. S.; Kelley, M. J.; Koningsberger, D. C.; Gates, B. C. Gamma-Al_2O_3-Supported Re-Pt Cluster Catalyst Prepared from $Re_2Pt(CO)_{12}$: Characterization by Extended X-Ray Absorption Fine Structure Spectroscopy and Catalysis of

Methylcyclohexane Dehydrogenation. *J. Am. Chem. Soc.* **1997**, *119*, 5877–5887.

(27) Iida, H.; Igarashi, A. Structure Characterization of Pt-Re/TiO_2 (Rutile) and Pt-Re/ZrO_2 Catalysts for Water Gas Shift Reaction at Low-Temperature. *Appl. Catal. A Gen.* **2006**, *303*, 192–198.

(28) Dexpert, H.; Lagarde, P.; Bournonville, J. P. EXAFS Studies of Bimetallic Pt-Re/Al_2O_3 Catalysts. *J. Mol. Catal.* **1984**, *25*, 347–355.

(29) Falcone, D. D.; Hack, J. H.; Klyushin, A. Y.; Knop-Gericke, A.; Schlogl, R.; Davis, R. J. Evidence for the Bifunctional Nature of Pt-Re Catalysts for Selective Glycerol Hydrogenolysis. *ACS Catal.* **2015**, *5*, 5679–5695.

(30) Panagiotopoulou, P.; Kondarides, D. I. Effect of the Nature of the Support on the Catalytic Performance of Noble Metal Catalysts for the Water-Gas Shift Reaction. *Catal. Today* **2006**, *112*, 49–52.

(31) Rhatigan, S.; Nolan, M. CO_2 and Water Activation on Ceria Nanocluster Modified TiO_2 Rutile (110). *J. Mater. Chem. A* **2018**, *6*, 9139–9152.

(32) Vecchietti, J.; Bonivardi, A.; Xu, W.; Stacchiola, D.; Delgado, J. J.; Calatayud, M.; Sebastián, S.; Collins, E. Understanding the Role of Oxygen Vacancies in the Water Gas Shift Reaction on Ceria-Supported Platinum Catalysts. *ACS Catal.* **2014**, *4*, 2088–2096.

(33) Kauppinen, M. M.; Melander, M. M.; Bazhenov, A. S.; Honkala, K. Unraveling the Role of the Rh−ZrO_2 Interface in the Water−Gas-Shift Reaction via a First-Principles Microkinetic Study. *ACS Catal.* **2018**, *8*, 11633–11647.

(34) Calatayud, M.; Markovits, A.; Menetrey, M.; Mguig, B.; Minot, C. Adsorption on Perfect and Reduced Surfaces of Metal Oxides. *Catal. Today* **2003**, *85*, 125–143.

(35) Pan, J. M.; Maschhoff, B. L.; Diebold, U.; Madey, T. E. Interaction of Water, Oxygen, and Hydrogen with TiO_2(110) Surfaces Having Different Defect Densities. *J. Vac. Sci. Technol. A* **1992**, *10*, 2470–2476.

(36) Diebold, U. Structure and Properties of TiO_2 Surfaces: A Brief Review. *Appl. Phys. A* **2003**, *76*, 681–687.

(37) Geng, Z.; Jin, X.; Wang, R.; Chen, X.; Guo, Q.; Ma, Z.; Dai, D.; Fan, H.; Yang, X. Low-Temperature Hydrogen Production via Water Conversion on Pt-Supported TiO_2. *J. Phys. Chem. C* **2018**, *122*, 10956–10962.

(38) Ammal, S. C.; Heyden, A. Water−Gas Shift Catalysis at Corner Atoms of Pt Clusters in Contact with a TiO_2(110) Support Surface. *ACS Catal.* **2014**, *4*, 3654–3662.

(39) Huang, Z.; Fryer, J. R.; Park, C.; Stirling, D.; Webb, G. Transmission Electron Microscopy and Energy Dispersive X-Ray Spectroscopy Studies of Pt-Re/γ-Al_2O_3 Catalysts. *J. Catal.* **1994**, *148*, 478–492.

(40) Galhenage, R. P.; Xie, K.; Yan, H.; Seuser, G. S.; Chen, D. A. Understanding the Growth, Chemical Activity, and Cluster−Support Interactions for Pt−Re Bimetallic Clusters on TiO_2(110). *J. Phys. Chem. C* **2016**, *120*, 10866–10878.

(41) Park, J. B.; Ratliff, J. S.; Ma, S.; Chen, D. A. In Situ Scanning Tunneling Microscopy Studies of Bimetallic Cluster Growth: Pt-Rh on TiO_2(110). *Surf. Sci.* **2006**, *600*, 2913–2923.

(42) Galhenage, R. P.; Yan, H.; Tenney, S. A.; Park, N.; Henkelman, G.; Albrecht, P.; Mullins, D. R.; Chen, D. A. Understanding the Nucleation and Growth of Metals on TiO_2: Co Compared to Au, Ni and Pt. *J. Phys. Chem. C* **2013**, *117*, 7191–7201.

(43) Azzam, K. G.; Babich, I. V.; Seshan, K.; Lefferts, L. A Bifunctional Catalyst for the Single-Stage Water-Gas Shift Reaction in Fuel Cell Applications. Part 2. Roles of the Support and Promoter on Catalyst Activity and Stability. *J. Catal.* **2007**, *251*, 163–171.

(44) Ronning, M.; Gjervan, T.; Prestvik, R.; Nicholson, D. G.; Holmen, A. Influence of Pretreatment Temperature on the Bimetallic Interactions in Pt-Re/Al_2O_3 Reforming Catalysts Studied by X-Ray Absorption Spectroscopy. *J. Catal.* **2001**, *204*, 292–304.

(45) Pieck, C. L.; Marecot, P.; Querini, C. A.; Parera, J. M.; Barbier, J.; Querini Parera J Barbier, C. J. Influence of Pt-Re Interaction on Activity and Selectivity of Reforming Catalysts. *Appl. Catal. A* **1995**, *133*, 281–292.

(46) Duke, A. S.; Xie, K.; Monnier, J. R.; Chen, D. A. Superior Long-Term Activity for a Pt-Re Alloy Compared to Pt in Methanol Oxidation Reactions. *Surf. Sci.* **2017**, *657*, 35–43.

(47) Tenney, S. A.; Xie, K.; Monnier, J. R.; Rodriguez, A.; Galhenage, R. P.; Duke, A. S.; Chen, D. A. Novel Recirculating Loop Reactor for Studies on Model Catalysts: CO Oxidation on Pt/TiO_2(110). *Rev. Sci. Instrum.* **2013**, *84*, 104101.

(48) Tenney, S. A.; Ratliff, J. S.; He, W.; Roberts, C. C.; Ammal, S. C.; Heyden, A.; Chen, D. A. Adsorbate-Induced Changes in the Surface Composition of Bimetallic Clusters: Au-Pt on TiO2(110). *J. Phys. Chem. C* **2010**, *114*, 21652–21663.

(49) Tenney, S. A.; He, W.; Roberts, C. C.; Ratliff, J. S.; Shah, S. I.; Shafai, G. S.; Turkowski, V.; Rahman, T. S.; Chen, D. A. CO-Induced Diffusion of Ni Atoms to the Surface of Ni–Au Clusters on TiO2(110). *J. Phys. Chem. C* **2011**, *115*, 11112–11123.

(50) Tenney, S. A.; Cagg, B. A.; Levine, M. S.; He, W.; Manandhar, K.; Chen, D. A. Enhanced Activity for Supported Au Clusters: Methanol Oxidation on Au/TiO2(110). *Surf. Sci.* **2012**, *606*, 1233–1243.

(51) Tenney, S. a.; He, W.; Roberts, C. C.; Ratliff, J. S.; Shah, S. I.; Shafai, G. S.; Turkowski, V.; Rahman, T. S.; Chen, D. a. CO-Induced Diffusion of Ni Atoms to

the Surface of Ni-Au Clusters on TiO2(110). *J. Phys. Chem. C* **2011**, *115*, 11112–11123.

(52) Ratliff, J. S. The Morphology and Catalytic Activity of Bimetallic Nanoclusters Supported on TiO2(110), University of South Carolina, 2009.

(53) Park, J. B.; Conner, S. F.; Chen, D. A. Bimetallic Pt-Au Clusters on TiO2(110): Growth, Surface Composition and Metal-Support Interactions. *J. Phys. Chem. C* **2008**, *112*, 5490–5500.

(54) Stempel, S.; Bäumer, M.; Freund, H. J. STM Studies of Rhodium Deposits on an Ordered Alumina Film -- Resolution and Tip Effects. *Surf. Sci.* **1998**, *404*, 424–427.

(55) Howells, A.; Harris, T.; Sashikata, K.; Chottiner, G. S.; Scherson, D. A. Model Systems in Electrocatalysis: Electronic and Structural Characterization of Vapor Deposited Platinum on the Basal Plane of Highly Oriented Pyrolytic Graphite. *Solid State Ionics* **1997**, *94*, 115–121.

(56) Marcus, P.; Hinnen, C. XPS Study of the Early Stages of Deposition of Ni, Cu and Pt on HOPG. *Surf. Sci.* **1997**, *392*, 134–142.

(57) Howells, A. R.; Hung, L.; Chottiner, G. S.; Scherson, D. A. Effects of Substrate Defect Density and Annealing Temperature on the Nature of Pt Clusters Vapor Deposited on the Basal Plane of Highly Oriented Pyrolytic Graphite. *Solid State Ionics* **2002**, *150*, 53–62.

(58) Venugopal, A.; Pirkle, A.; Wallace, R. M.; Colombo, L.; Vogel, E. M. Contact Resistance Studies of Metal on HOPG and Graphene Stacks. *AIP Conf. Proc.* **2009**, *1173*, 324.

(59) Galhenage, R. P.; Xie, K.; Diao, W.; Tengco, J. M. M.; Seuser, G. S.; Monnier, J. R.; Chen, D. A. Platinum-Ruthenium Bimetallic Clusters on Graphite: A Comparison of Vapor Deposition and Electroless Deposition Methods. *Phys. Chem. Chem. Phys.* **2015**, *17*, 28354–28363.

(60) Yuan, Z.; Hanf, M. C.; Stephan, R.; Dulot, F.; Denys, E.; Florentin, A.; Harbich, W.; Wetzel, P. Growth of Palladium Nanoparticles on Nanostructured Highly Ordered Pyrolytic Graphite. *Surf. Interface Anal.* **2015**, *47*, 82–86.

(61) Yang, D.-Q.; Piyakis, K. N.; Sacher, E. The Manipulation of Cu Cluster Dimensions on Highly Oriented Pyrolytic Graphite Surfaces by Low Energy Ion Beam Irradiation. *Surf. Sci.* **2003**, *536*, 67–74.

(62) de Boer, F. R.; Boom, R.; Mattens, W. C. M.; Miedema, A. R.; Niessen, A. K. *Cohesion in Metals: Transition Metal Alloys*; Vol. 1.; North-Holland Physics Publishing: Amsterdam, 1998.

(63) Tenney, S. A.; Shah, S. I.; Yan, H.; Cagg, B. A.; Levine, M. S.; Rahman, T. S.; Chen, D. A. Methanol Reaction on Pt-Au Clusters on TiO2(110): Methoxy-

Induced Diffusion of Pt. *J. Phys. Chem. C* **2013**, *117*, 26998–27006.

(64) Duke, A. S.; Galhenage, R. P.; Tenney, S. A.; Sutter, P.; Chen, D. A. In Situ Studies of Carbon Monoxide Oxidation on Platinum and Platinum-Rhenium Alloy Surfaces. *J. Phys. Chem. C* **2015**, *119*, 28.

(65) Radhakrishnan, R.; Willigan, R. R.; Dardas, Z.; Vanderspurt, T. H. Water Gas Shift Activity and Kinetics of Pt/Re Catalysts Supported on Ceria-Zirconia Oxides. *Appl. Catal. B Environ.* **2006**, *66*, 23–28.

(66) Duke, A. S.; Galhenage, R. P.; Tenney, S. A.; Sutter, P.; Chen, D. A. In Situ Studies of Carbon Monoxide Oxidation on Platinum and Platinum–Rhenium Alloy Surfaces. *J. Phys. Chem. C* **2015**, *119*, 381–391.

(67) Ammal, S. C.; Heyden, A. Origin of the Unique Activity of Pt/TiO2 Catalysts for the Water–Gas Shift Reaction. *J. Catal.* **2013**, *306*, 78–90.

(68) Standard Guide to Scanner and Tip Related Artifacts in Scanning Tunneling Microscopy and Atomic Force Microscopy. *ASTM International*, 2004, E2382-04.

(69) Fisher, G. B.; Sexton, B. A. Identification on an Adsorbed Hydroxyl Species on the Pt(111) Surface. *Phys. Rev. Lett.* **1980**, *44*, 683–686.

(70) Flaherty, D. W.; Yu, W. Y.; Pozun, Z. D.; Henkelman, G.; Mullins, C. B. Mechanism for the Water-Gas Shift Reaction on Monofunctional Platinum and Cause of Catalyst Deactivation. *J. Catal.* **2011**, *282*, 278–288.

(71) Bruix, A.; Rodriguez, J. A.; Ramirez, P. J.; Senanayake, S. D.; Evans, J.; Park, J. B.; Stacchiola, D.; Liu, P.; Hrbek, J.; Illas, F. A New Type of Strong Metal-Support Interaction and the Production of H_2 through the Transformation of Water on $Pt/CeO_2(111)$ and $Pt/CeO_x/TiO_2(110)$ Catalysts. *J. Am. Chem. Soc.* **2012**, *134*, 8968–8974.

(72) Kalamaras, C. M.; Panagiotopoulou, P.; Kondarides, D. I.; Efstathiou, A. M. Kinetic and Mechanistic Studies of the Water-Gas Shift Reaction on Pt/TiO_2 Catalyst. *J. Catal.* **2009**, *264*, 117–129.

(73) Efstathiou, A. M. Elucidation of Mechanistic and Kinetic Aspects of Water-Gas Shift Reaction on Supported Pt and Au Catalysts via Transient Isotopic Techniques. In *Catalysis, Vol 28*; Spivey, J. J.; Han, Y. F.; Dooley, K. M., Eds.; 2016; Vol. 28, pp. 175–236.

(74) Aranifard, S.; Ammal, S. C.; Heyden, A. On the Importance of Metal-Oxide Interface Sites for the Water-Gas Shift Reaction over Pt/CeO_2 Catalysts. *J. Catal.* **2014**, *309*, 314–324.

(75) Ciftci, A.; Ligthart, D.; Hensen, E. J. M. Influence of Pt Particle Size and Re Addition by Catalytic Reduction on Aqueous Phase Reforming of Glycerol for Carbon-Supported Pt(Re) Catalysts. *Appl. Catal. B* **2015**, *174*, 126–135.

CHAPTER 4

OXIDATION OF MONOMETALLIC RE AND BIMETALLIC PT-RE SURFACES ON TITANIA, HOPG, AND PT(111)

4.1 Introduction

Interest in Pt-Re surfaces has grown over recent years for their use in heterogeneous catalysis. Supported bimetallic Pt-Re systems have exhibited unique properties distinct from Pt or Re alone. The addition of Re to Pt catalysts has shown greater activity and selectivity in a number of hydrocarbon reforming reactions.[1–3] Pt-Re surfaces on titania are reported to have higher activity than monometallic Pt on titania for the water-gas shift (WGS) reaction.[4–7] Additionally, studies of aqueous phase reforming (APR) of glycerol and other polyols have demonstrated that Pt-Re catalysts supported on carbon have higher turnover frequencies and longer lifetimes compared to pure Pt catalysts on carbon.[8–10] The enhanced activity of Pt-Re surfaces is proposed to be due to weaker binding of CO to the Pt-Re surface compared to Pt and is attributed to changes in the electronic structure of the bimetallic surface; thus, weaker CO binding is responsible for higher activity due to decreased CO poisoning.[9,11,12] Alternatively, the presence of ReO_x during catalytic reactions may influence the overall TOF by providing sites for CO bond cleavage in APR or deoxydehydration of glycerol.[10,13]

Nonetheless, the electronic interactions between Re and Pt during reaction are not completely understood. For instance, the presence of Pt can significantly influence the extent of oxidation of Re under oxidizing conditions. Some studies have reported that Re

can be reduced at a lower temperature when Pt is present, and have attributed it to the spillover of hydrogen from Pt onto Re.[14,15] On the contrary, a different study has reported that the presence of Pt facilitates the oxidation of Re on a carbon support after being exposed to water vapor at 225 °C.[10] In CO oxidation experiments conducted previously by Duke et al., a Re film of 2.0 ML Re on Pt(111) and a Pt-Re alloy formed by deposition of 2.9 ML Re on Pt(111) followed by annealing at 1000 K for 5 min were exposed to 500 mTorr O_2/50 mTorr CO at elevated temperatures.[16] Re in higher oxidation states was observed in X-ray photoelectron spectroscopy (XPS) measurements for both surfaces, but the Re film had a notably greater extent of Re oxidation. This result is somewhat convoluted by the fact that originally more Re is present at the surface for the Re film on Pt(111) than the Pt-Re alloy. A greater portion of exposed Re, may aid in its oxidation. In the alloy, Re exists below a layer of Pt, but can be drawn to the surface in oxidizing conditions.[16,17] Thus, for the Pt-Re alloy, the Re(4f) XPS signal still has substantial Re in the metallic state due to some Re remaining subsurface.[16] An alternative outcome arises for clusters of Pt and Re grown on TiO_2(110). After exposing surfaces of Re/TiO_2 and Pt-Re/TiO_2 to methanol oxidation conditions, Re in the bimetallic Pt-Re/TiO_2 clusters is much more oxidized than monometallic Re/TiO_2 clusters.[18] Again, the results are not entirely straightforward, since the oxidation of oxophillic Re deposited on a TiO_2 support may be hindered by the strong interaction Re already has with the oxide support.[19]

The oxidation state of Re and its extent of oxidation in various environments are pertinent factors in many heterogeneous catalytic reactions. In this work, the oxidation state of Re is studied with and without the presence of Pt on three different supports of TiO_2(110), highly oriented pyrolytic graphite (HOPG), and Pt(111). The surfaces are

prepared in ultrahigh vacuum (UHV) and exposed to high pressures (~800 Torr) of oxygen at elevated temperatures (100 °C) in a UHV-coupled microreacter. XPS analysis of the surfaces was conducted before and after oxidation experiments without exposing the samples to air. The results demonstrate that Re oxidation for Pt-Re clusters is enhanced over monometallic Re clusters on both an oxide support of titania and on a non-interactive support of HOPG. The oxidation of pure Re clusters on TiO_2 and HOPG display comparable Re oxide species. When Re is present as a thick film on top of Pt(111), Re is extremely difficult to oxidize compared to thin Re films on Pt(111). It is suggested that small Re clusters are more easily oxidized than bulk Re, and that Pt assists in increasing the dispersion of Re and formation of small Re ensembles leading to the enhanced oxidation in bimetallic Pt-Re surfaces.

4.2 Experimental

Experiments were conducted in an ultrahigh vacuum chamber which has been described in detail previously.[7,20] The chamber operates at a base pressure < 2 x 10^{-10} Torr and is coupled to a microreactor.[21] It is equipped with a residual gas analyzer (Stanford Research Systems, RGA 300), a hemispherical analyzer (SPECS EA10) and Mg/Al Kα X-ray source (Leybold Heraeus, RQ 20/63) for XPS measurements. The chamber also includes an infrared reflection absorption spectroscopy (IRAS) system (Bruker, Tensor 27) with external liquid nitrogen-cooled mercury cadmium telluride (LN-MCT) detector. Samples were prepared on one of three supports: 1) rutile TiO_2(110) crystal (Princeton Scientific Corporation, 10 mm x 10 mm x 1 mm), 2) HOPG crystal (SPI Supplies, 10 mm x 10 mm x 1 mm), each of which were mounted on a Ta back plate using thin Ta foil straps; and 3) Pt(111) crystal (99.999%, Princeton Scientific

Corporation, 8 mm diameter, 2 mm thickness) which was mounted by press-fitting two Ta wires into 1.1 mm deep slots cut into the sides of the crystal. The Ta wires were spot-welded onto a Ta sample plate. The TiO_2 and Pt(111) crystals were cleaned by Ar^+ ion sputtering at 1 kV for 20 min, followed by annealing to 950-1000 K for 3 min by electron bombardment from a tungsten filament positioned behind the sample plate. The crystal temperature was monitored by an infrared pyrometer (Heitronics). The HOPG surface was prepared by cleaving with adhesive tape. For some experiments, the HOPG surface was sputtered to create defects for metal nucleation using Ar^+ ions at 500 eV and a current of 0.1 μA for 5 minutes. The HOPG support was then heated by electron bombardment using a tungsten filament positioned behind the sample plate to 950-1000 K for 12 minutes (3 cycles of 4 min) to remove embedded Ar. The support temperature was also monitored by an infrared pyrometer (Heitronics). Metal clusters of Pt and Re were grown by vapor deposition from a Pt rod (ESPI, 2 mm diameter, 99.95%) and a Re rod (ESPI, 2 mm diameter, 99.99%) using a four-pocket electron-beam evaporator (Oxford Applied Research, EGCO4). Pt and Re metal were deposited sequentially onto the support surface at a rate of approximately 0.08-0.1 ML/min, with one monolayer (ML) being defined as the packing density of Pt(111) (1.50×10^{15} atoms/cm^2) or Re(0001) (1.52×10^{15} atoms/cm^2). The metal flux was calibrated with a UHV bakeable quartz crystal microbalance (QCM, Inficon, XTM-2) before each deposition. Fresh surfaces were prepared for each experiment.

Samples were prepared in the UHV chamber and then directly transferred into the microreactor without exposure to air. The oxidation experiments were conducted in a gas mixture of 20% O_2 (Airgas, 99.5%) and 80% He (Airgas, 99.999%) in static mode by

filling the reactor with the measured gas concentration and closing off the inlet and outlet of the reactor loop. O_2 and He were introduced via independently calibrated mass flow controllers (Brooks, 5850e and 5850i) and the gas composition was determined by a digital flow meter (Agilent Technologies, ADM2000). The reactor was heated and cooled in the same pre-set O_2/He mixture at a rate of 2.0 °C/min by heating tape (Briskheat, BWHD) wrapped around the exterior of the reactor housing. To ensure uniform heating and cooling, the heating tape was regulated by a feedback loop on a temperature controller (Auber, SYL-4342P). The temperature of the sample was measured by a type K thermocouple (Omega, KMQSS-040G-6) welded into the feed gas inlet close to the surface of the sample. The gas lines were heated to a temperature of 65 °C using Valco Instruments temperature controllers. The pressure within the reactor and lines (~800 Torr) was measured by a capacitance manometer (MKS Instruments, Baratron 722A). After oxidation, the gas mixture was directly pumped out of the reactor by a turbo molecular pump (Leybold, TMP 150).

XPS measurements were collected before and after oxidation experiments without the sample being exposed to air. A dwell time of 0.2 seconds and step size of 0.025 eV were used for C(1s), O(1s), Re(4f), Pt(4f), and Ti(2p) regions. A survey scan was also collected to ensure there were no contaminants before or after the reaction.

4.3 Results and Discussion

Monometallic Re and bimetallic Pt-Re clusters were studied on a TiO_2(110) and HOPG support in addition to Re films on Pt(111) to evaluate the extent of Re oxidation with and without the presence of Pt, and the potential influence of the support. Figure 4.1 displays XPS data of the Re(4f) region for 2 ML Re, 2 ML Re + 2 ML Pt, and 2 ML Pt +

2 ML Re deposited on TiO_2. The XPS data for the 2 ML Re/TiO_2 surface before oxidation is shown for comparison. The Re($4f_{7/2}$) peak position appears at 40.4 eV for this surface as well as for the bimetallic surfaces, close to that of the binding energy for metallic Re (~40.3 eV).[22–26] After exposing the surfaces to 20% O_2/He at 100 °C for 2 hours the bimetallic clusters exhibit a significantly greater extent of oxidation than the monometallic Re clusters. The 2 ML Re/TiO_2 surface displays the majority of Re in the oxidized Re^{2+} and Re^{4+} states, with some contribution from Re in the +6 oxidation state. Oxidation state assignments are based on binding energy estimates supported by literature reports for Re^{2+} (41.1-42.1 eV), Re^{4+} (42.5-43.3 eV), Re^{5+} (43.7-44.1 eV) and Re^{6+} (44.8-45.4 eV)[23,25,27–31]. Comparing the bimetallic surfaces, the Pt+Re and Re+Pt

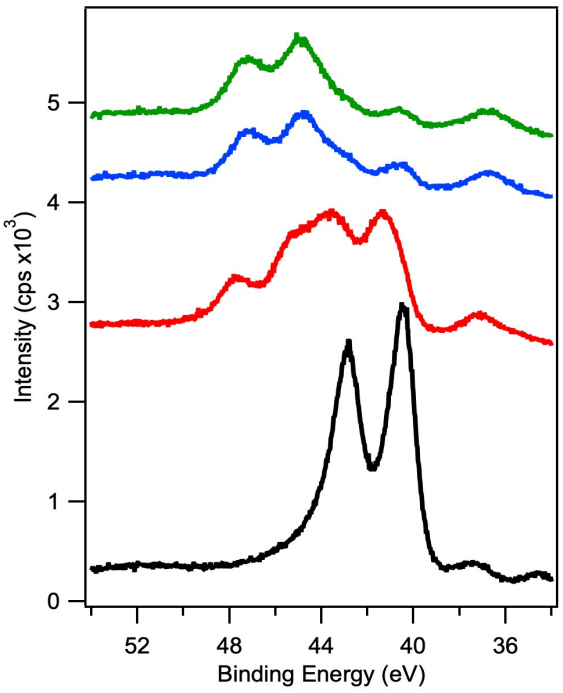

Figure 4.1: X-ray photoelectron spectroscopy data for the Re(4f) region of 2 ML Re/TiO_2 (black) before oxidation; and 2 ML Re/TiO_2 (red), 2 ML Pt + 2 ML Re/TiO_2 (blue) and 2 ML Re + 2 ML Pt/TiO_2 (green) after oxidation in 20% O_2/He at 100 °C for 2 hours.

clusters on TiO_2(110) have nearly identical Re oxidation results, with the majority of Re contribution coming from the higher oxidation state of Re^{6+} (44.8-45.4 eV). Previous STM studies for Pt-Re clusters on TiO_2(110) have established that bimetallic clusters are formed via either order of deposition for the two metals; whether Pt is deposited on top of Re or Re on top of Pt.[19] Previous experiments to probe the surface composition of the bimetallic clusters using CO molecules has established that 2 ML Pt deposited on top of 2 ML Re creates a Re core-Pt shell structure in which the surface is rich in Pt atoms.[7] This can be understood by the lower surface free energy of Pt (2.48 J/m^2) compared to Re (3.60 J/m^2),[32] and the strong affinity of Re toward the oxide support.[19] Bimetallic clusters for the reverse order of deposition in which 2 ML Re is deposited on top of 2 ML Pt exhibit an accumulation of Re at the surface. This can be attributed to kinetic limitations for the complete diffusion of Re atoms into the existing cluster; thus both Pt and Re atoms exist at the surface.[7] Although the order of deposition forms very different bimetallic compositions, the extent of Re oxidation after exposure to oxygen is very nearly identical for the Pt+Re and Re+Pt surfaces on TiO_2. It appears that the Re atoms residing below a layer of Pt are drawn to the surface and just as easily oxidized as Re atoms already residing at the surface. Other studies conducted by Duke et al. reported Re diffusion to the surface in the presence of oxygen when covered by Pt.[16,31] For Pt-Re alloys formed by deposition of ~2.0 ML Re onto Pt(111) and annealed to 1000 K for 5 min, exposure to 500 mTorr of O_2 at 500 K resulted in the metallic Re, originally residing below a layer of Pt, diffusing to the surface and exhibiting oxidized Re in the +5 and +6 oxidation states.[16,31] In addition, DFT calculations found that Pt-Re model surfaces show

a thermodynamic driving force for Re to diffuse to the surface in the presence of oxygen.[31]

In contrast to the bimetallic Pt-Re clusters on TiO_2, the 2 ML Re/TiO_2 surface did not exhibit significant Re in higher oxidation states. These clusters consisted of only Re at the surface, yet they underwent oxidation to a lesser degree than the bimetallic Pt-Re surfaces when exposed to oxygen. One explanation may be that the clusters in the monometallic surface consist of large Re ensembles that are difficult to oxidize, whereas Re in the bimetallic surfaces becomes more dispersed in the Pt clusters, and smaller ensembles of Re are present at the surface that enable more facile oxidation. A study by Okal et al. analyzed the oxidation of 1.04% Re/γ-Al_2O_3 and 10.4% Re/γ-Al_2O_3 after exposure to air at room temperature.[29] The low weight-loaded sample consisted of Re particles with an average size of 2.1 nm; while the high weight-loaded sample consisted of larger Re particles with an average size of 4.9 nm. The authors found that the sample of large particles was less oxidized than the sample of small particles, where 94.5% of Re in the large particles remained in the metallic state and only 2.0% was oxidized to Re^{2+}. The smaller Re particles, however, had a lower amount of 60.5% of metallic Re remaining and oxidized 20.5% to Re^{2+}.[29] The authors attributed the greater extent of oxidation of the low weight-loaded sample to the smaller Re particle size and greater dispersion on the support, as evidenced by HRTEM measurements.[29] A second explanation for the different oxidation behavior of monometallic Re on TiO_2 may be that without the presence of Pt, Re atoms are more strongly influenced by the oxide support. A study by Mitra et al. examined the reducibility of Re_2O_7 species on two different oxide supports: TiO_2 and Al_2O_3.[33] They found that the reducibility of Re species was strongly

influenced by the support, and that reduction of Re_2O_7 on TiO_2 was much more efficient than Re_2O_7 on Al_2O_3.[33] Chądzyński and Kubicka found that after oxidation at 400 °C for 1 hour, the volumetric uptake of oxygen by a low weight loaded Re/γ-Al_2O_3 reached an O/Re ratio of only 2.62 instead of 3.5 as expected for complete oxidation of Re to Re_2O_7.[34] The authors attributed this to the considerable portion of Re bound to the alumina support, forming stable oxide complexes resistant to oxidation. Thus, the interaction of Re with TiO_2 needs to be decoupled in order to determine if the influence is hindering the ability of Re to become oxidized.

In order to eliminate the possible influence of the titania support, monometallic clusters of Re and bimetallic Pt-Re clusters were deposited and oxidized on a support of HOPG. This support is reported to have very little to no interaction with metals.[35–38] Figure 4.2 displays XPS data of the Re(4f) region for 2 ML Re, 2 ML Re + 2 ML Pt, and 2 ML Pt + 2 ML Re deposited on HOPG. Data of the 2 ML Re/HOPG surface before oxidation is shown, and the Re($4f_{7/2}$) peak position appears at 40.3 eV for all three surfaces, similar to that for clusters on TiO_2 before oxidation. After exposure to 20% O_2/He at 100 °C for 2 hours, the bimetallic Pt-Re clusters are again much more oxidized than the monometallic Re clusters on HOPG, just as was seen for clusters on TiO_2. Similar to clusters on TiO_2, the bimetallic clusters display the majority of Re species in the +6 oxidation state, while the monometallic Re clusters consist of Re predominantly in the +2 and +4 oxidation states. From the comparable oxidation behavior seen for clusters on two very different supports of TiO_2 and HOPG, the reason behind the enhanced oxidation for bimetallic Pt-Re clusters and lesser extent of oxidation for monometallic Re clusters cannot be attributed to the strong interaction of Re with the oxide support.

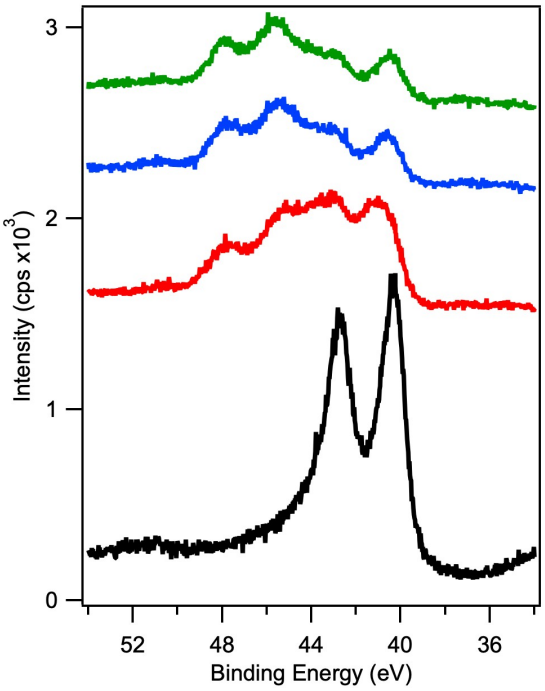

Figure 4.2: XPS data for the Re(4f) region of 2 ML Re/HOPG (black) before oxidation; and 2 ML Re/HOPG (red), 2 ML Pt + 2 ML Re/HOPG (blue), and 2 ML Re + 2 ML Pt/HOPG (green) after oxidation in 20% O_2/He at 100 °C for 2 hours.

Studies of Re clusters deposited on modified and unmodified HOPG were conducted to investigate reports of cluster size and dispersion having an influence on the oxidation extent of Re.[29,39] It has been found for alumina supported metals such as Pt, Rh, and Pd that the particle size has a significant effect on the stoichiometry of metal oxides formed in oxidation treatments.[40–42] Due to the weak interaction of metal particles on HOPG, metal atoms have a high mobility and form large clusters with low cluster densities when deposited on an untreated surface. However, Ar ion sputtering can be used to introduce defects on the HOPG surface to decrease the cluster size and increase the cluster density.[43–45] For instance, comparing 0.25 ML Re deposited on an unmodified HOPG support to 0.22 ML Re deposited on HOPG after sputtering for 5 min at 0.1 μA

and 500 eV, the cluster size decreases by 40% (from 10.7 to 6.4 Å) and the cluster density increases by 88% (from 1.33×10^{12} cm^{-1} to 11.18×10^{12} cm^{-1}).[46] In the experiment here, 2 ML Re was deposited on an unmodified HOPG support and on HOPG after sputtering for 5 min at 0.1 μA and 500 eV. Figure 4.3 displays the XPS data of the Re(4f) region for the 2 ML Re surfaces on modified and unmodified HOPG. Before oxidation, the Re($4f_{7/2}$) peak position appears at 40.3 eV for both surfaces. After exposure to 20% O_2/He at 100 °C for 2 hours, both surfaces display a range of Re oxidation states to +2, +4, and +6. However, the Re clusters on modified HOPG display a slightly greater extent of oxidation than the Re clusters on unmodified HOPG. For the modified HOPG surface, consisting of smaller particles with greater dispersion, there is a larger portion of Re in

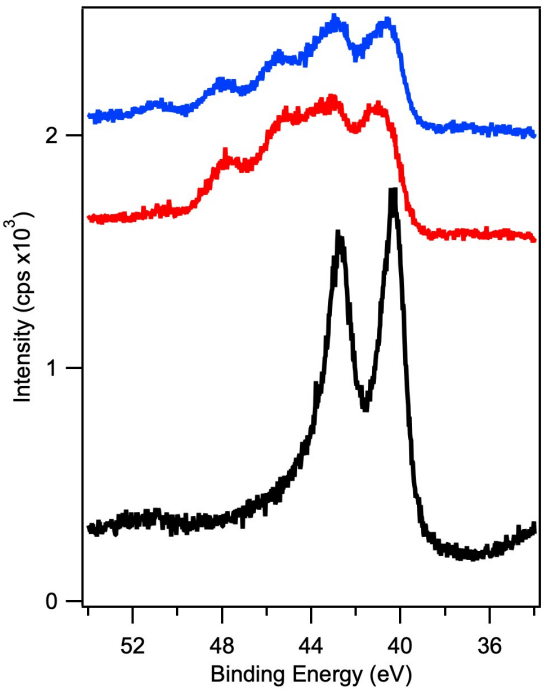

Figure 4.3: XPS data for the Re(4f) region of 2 ML Re/HOPG (black) before oxidation and 2 ML Re/HOPG (red) after oxidation for the modified HOPG support; and 2 ML Re/HOPG (blue) after oxidation for the unmodified HOPG support. Oxidation occurred in 20% O_2/He at 100 °C for 2 hours.

the higher oxidation state of +6 than for the Re clusters on unmodified HOPG, consisting of larger particles with less dispersion. It should also be noted that the Re signal intensity decreases by 32% for the Re clusters on modified HOPG from before and after oxidation, while the signal from Re clusters on unmodified HOPG only decreases by 27%. This decrease in signal is attributed to the loss of Re due to the formation and subsequent sublimation of Re_2O_7, given that at elevated temperatures Re_2O_7 is known to be highly volatile.[29,47] Thus, evidence is presented for Re clusters of smaller particle size and greater dispersion to achieve a greater extent of oxidation than larger particles that are less well dispersed.

Nonetheless, the reason behind the dramatic increase in Re oxidation that occurs in the presence of Pt is not obvious. From the results shown, the bimetallic clusters on both the TiO_2 and HOPG supports undergo similar enhancements of Re oxidation over their monometallic Re counterparts when exposed to the same oxidizing conditions. However, it is unclear whether the contact between Pt and Re is leading to enhanced Re oxidation or if it is an effect of the small size that Re ensembles adopt when intermixed with Pt. In order to maximize the contact between Pt and Re, thin Re films were deposited onto a Pt(111) single crystal at varying coverages. From STM images collected previously[46] a Re coverage of 0.8 ML was chosen to reduce the number of second layer Re islands that grow with 1.0 ML coverage. Deposition of 0.8 ML of Re results in a first layer that almost completely covers the Pt(111) surface with a few second layer islands. A second coverage of 1.8 ML Re was chosen to reduce the number of third layer Re islands that grow, where the first layer of Re nearly completely covers the Pt(111) surface and a second layer of islands grows on top.[46] Figure 4.4a displays XPS data of the Re(4f)

region for 0.8 ML and 1.8 ML Re deposited on Pt(111). Before oxidation, the Re($4f_{7/2}$) peak position appears at 40.3-40.4 eV for the two surfaces. After exposing both surfaces to 20% O_2/He at 100 °C for 2 hours, the Re(4f) region displays binding energy shifts for both surfaces predominantly to the +4 oxidation state (~43.3 eV) and some contribution from the +6 oxidation state given the shoulder at higher binding energy. The peaks for Re^{4+} appear on the high end of the range for Re^{4+} (42.5-43.3 eV)[27,48,49] found in the literature, but they are too low to be attributed to Re^{5+}(43.7-44.1 eV). Furthermore, there are few reports of Re_2O_5, due to its instability, and therefore is unlikely to be the predominant species.[50–52] Although distinctly different in coverage, the equal oxidation seen for these two Re films of 1 layer and 2 layers on the Pt(111) surface may not be so

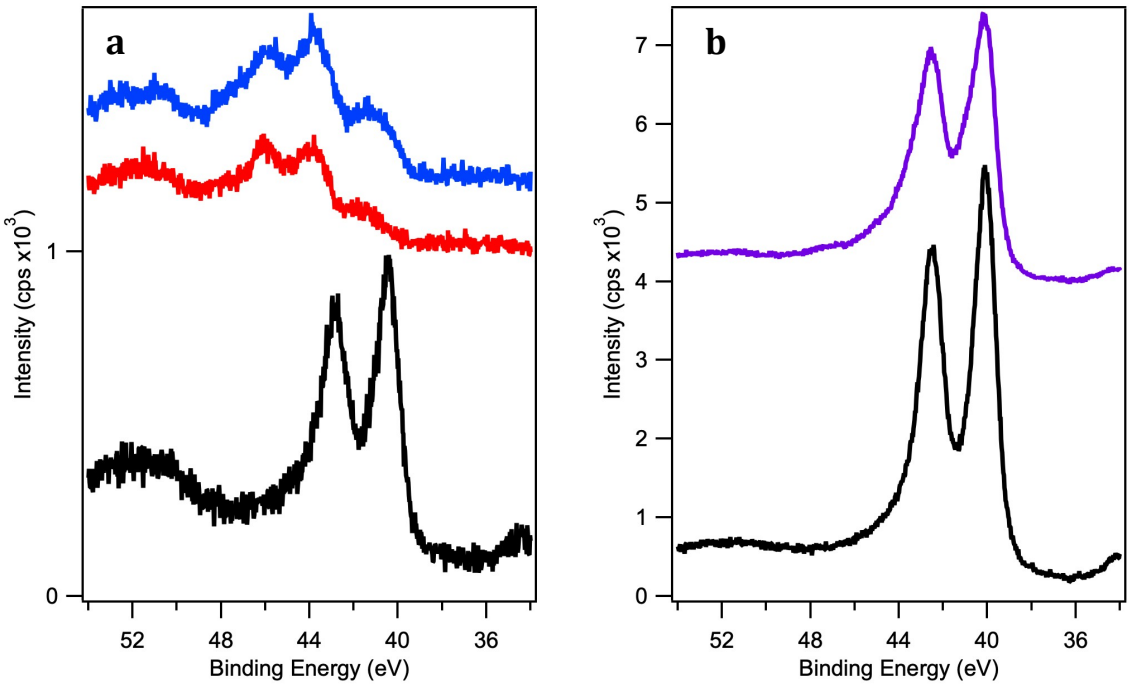

Figure 4.4: XPS data of the Re(4f) region for different coverages of Re films on Pt(111): a) 0.8 ML Re before oxidation (black), 0.8 ML Re (red) and 1.8 ML Re (blue) after oxidation in 20% O_2/He at 100 °C for 2 hours. b) 5 ML Re before oxidation (black) and after oxidation (purple) in 20% O_2/He at 100 °C for 2 hours.

surprising. If the Re ensembles in the 2 layer film are efficiently dispersed, they may be just as likely as the Re ensembles in the 1 layer film to become oxidized, especially at the high temperature and pressure conditions (100 °C, ~800 Torr) used here. A study involving oxidation of a 1.6 ML Re film on Pt(111) reported that Re was oxidized to the +5 and +6 states after being exposed to only 500 mTorr O_2 at 177 °C.[31] Additionally, there is a decrease in the Re(4f) XPS signal intensity from before and after oxidation of 72% for the 2 layer Re film, and a decrease of 63% for the 1 layer Re film. The decrease in signal is due to the sublimation of volatile Re_2O_7, indicating these two films were substantially oxidized in the given conditions.

A thicker Re film of 5 ML was grown on Pt(111) in order to investigate the oxidation extent of a surface composed of Re atoms in contact predominantly only with other Re atoms. Figure 4.4b displays the Re(4f) XPS data for the 5 ML Re/Pt(111) surface before and after oxidation in 20% O_2/He at 100 °C for 2 hours. Before oxidation, the Re($4f_{7/2}$) peak position appears at 40.1 eV, and after oxidation the peak position remains at 40.1 eV; however there is a slight shoulder extending to higher binding energy, indicating a very small level of Re oxidation occurs. From this data it can be seen that the thick Re film is very difficult to oxidize compared to the 1 layer and 2 layer films on Pt(111). A handful of oxidation studies have been conducted on polycrystalline Re foil and Re crystals, of which the majority have taken place at room temperature in UHV. In oxidation conditions where Re clusters can easily become oxidized, the Re foil and crystals exhibit little oxidation, and no oxides with a higher oxidation state than Re^{2+} are formed.[22,23,26,30,53] Interestingly, a distinction was found by Chan et al. in which exposure to 300 L of O_2 at ~1000 K oxidized close-packed Re(0001) to a maximum state of Re^{2+},

while oxidation of atomically rough Re(12$\bar{3}$1), with six layers of exposed surface atoms, produced a thin-film oxide comprising both ReO and Re_2O_3.[23] This report identifies both the difficulty in oxidizing a pure Re surface, and the small enhancement of Re oxidation when more Re atoms are present at step and edge sites. Re atoms at steps and edges have less coordination to surrounding atoms than Re atoms within a plane or terrace. Thus, undercoordinated Re atoms have the potential to interact with a greater number of oxygen atoms, likely leading to the greater extent of oxidation seen for smaller ensembles. Theoretical studies by Miniussi et al. analyzed the adsorption of oxygen molecules on a Re(0001) slab.[54] They observed that oxygen adsorbs preferentially in the 3-fold hollow sites, analogous to the majority of other close-packed transition metal surfaces. When determining saturation coverages, they found that each O_2 molecule required two adjacent 3-fold sites to break the O=O bond and accommodate two oxygen atoms. Therefore, as the oxygen coverage increased, the number of available 3-fold sites, especially those at adjacent positions, progressively decreased.[54] Thus a close packed surface of highly coordinated Re atoms may be hindering the process of oxygen adsorption compared to a surface with a greater number of steps or small cluster size.

In order to evaluate the relationship between undercoordinated Re atoms and extent of oxidation, a comparison is made for surfaces of decreasing particle size and increasing Re oxidation, illustrated in Figure 4.5. The average Re cluster height decreases for the following surfaces: 2 ML Re/HOPG,[55] 2 ML Re TiO_2,[19] and 0.8 ML/Pt(111)[46] as 13.7±2.3 Å, 4.7±1.0 Å, and 2.4±0.5 Å, respectively. In the figure, the XPS data of the Re(4f) region displays the 2 ML Re/HOPG surface before oxidation, in which the peak position was 40.3-40.4 eV for all surfaces. After oxidation in 20% O_2/He at 100 °C for 2

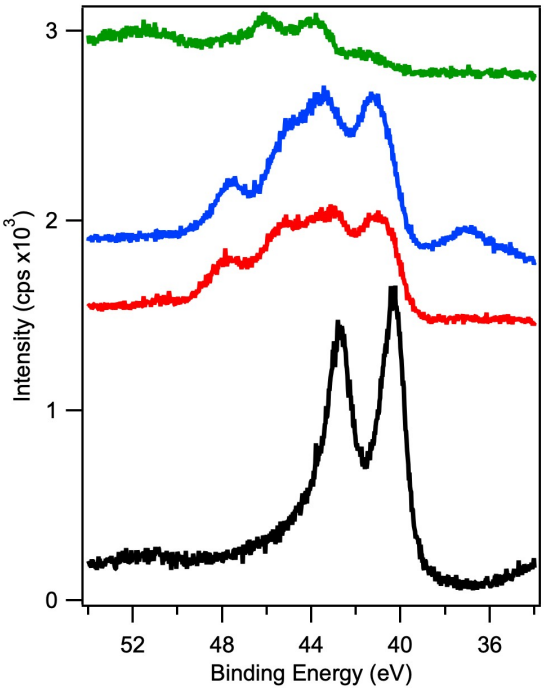

Figure 4.5: XPS data of the Re(4f) region for 2 ML Re/HOPG before oxidation (black), and 2 ML Re/HOPG (red), 2 ML Re/TiO_2 (blue), and 0.8 ML Re/Pt(111) (green) after oxidation in 20% O_2/He at 100 °C for 2 hours.

hours, the 0.8 ML/Pt(111) surface, consisting of the smallest Re particles, has the majority of Re residing in the higher oxidation states of Re^{4+} and Re^{6+}. The 2 ML Re clusters on TiO_2 and HOPG have the majority of Re in the +2 and +4 oxidation states with some contribution from the +6 state. Although the Re clusters on TiO_2 are considerably smaller than on HOPG, the two surfaces are oxidized to a similar extent. This suggests there is likely some interaction between the Re clusters and the titania support due to the oxophilic nature of Re. This interaction promotes a strong bonding of the clusters to the TiO_2 support that inhibits the surface from becoming more oxidized, as has been reported for Re on oxide supports.[3,34,39,56]

Based on the results shown here, it is seen that smaller Re ensembles are responsible for the greater extent of Re oxidation. From studies done previously by our group and those found in the literature, platinum and rhenium are known to form bulk alloys and demonstrate significant electronic interactions between the two metals.[16,19,31,57–61] In order to investigate whether the enhanced oxidation of Re in bimetallic Pt-Re clusters is unique to Pt or if this occurrence is standard for other types of metals in bimetallic Re clusters, a surface consisting of Au and Re particles on TiO_2 was prepared. Gold was chosen for its inertness towards oxygen, in regards to both gas-phase oxygen adsorption and interaction with the oxide support.[62–64] 2 ML Au was first deposited on TiO_2 followed by deposition of 2 ML Re. The surface was then exposed to the usual oxidation conditions of 20% O_2/He at 100 °C for 2 hours. Figure 4.6 displays a comparison of the XPS data for the Re(4f) region after oxidation for Au+Re/TiO_2 with Pt+Re/TiO_2 and Re/TiO_2. Before oxidation, the Re($4f_{7/2}$) peak position is at 40.3 eV binding energy for all surfaces. After oxidation, the Au+Re/TiO_2 surface displays Re oxidized to Re^{2+}, Re^{4+}, and Re^{6+}. Though the bimetallic Au-Re/TiO_2 surface is substantially oxidized, it is not oxidized to the same extent as the bimetallic Pt-Re/TiO_2 surface. Nonetheless, it does have a greater portion of Re in the higher oxidation states than the pure Re/TiO_2 clusters. The lesser extent of oxidation of the Au-Re surface compared to the Pt-Re surface cannot immediately be attributed to unique metal-metal interactions between Pt and Re compared to Au and Re. The morphology and composition of the Au-Re clusters must be considered. From careful studies conducted previously in our lab, the cluster size and density of metals deposited on TiO_2(110) are dependent on the admetal-oxygen bond strength between the deposited metal and the

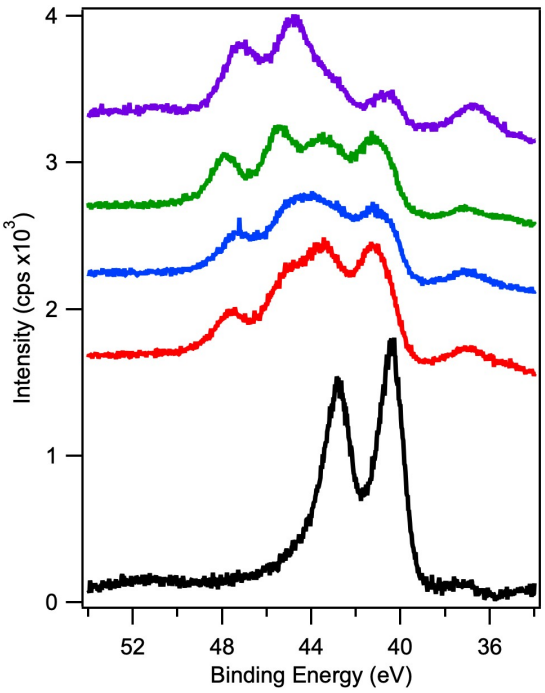

Figure 4.6: XPS data of the Re(4f) region for 2 ML Re/TiO_2 before oxidation (black), and 2 ML Re/TiO_2 (red), 2 ML Au + 2 ML Re/TiO_2 (blue), 2 ML Co + 2 ML Re/TiO_2 (green), and 2 ML Pt + 2 ML Re/TiO_2 (purple) after oxidation in 20% O_2/He at 100 °C for 2 hours.

support.[19,65] Au has a weak metal-titania interaction, therefore large clusters are formed upon deposition in comparison to other metals such as Pt, Ni, and Co.[65] Given the high Au coverage, when Re is deposited second it likely nucleates on top of the large Au clusters. Unlike Pt and Re, Au and Re are immiscible in the bulk,[58] but the surface free energy of Au (1.50 J/m^2)[66] is much lower than that of Re (3.60 J/m^2)[32]; therefore some Au is likely to diffuse to the surface of the cluster, dispersing the large ensembles of Re at the surface. Nonetheless, the larger Re ensembles in the Au-Re surface are not as oxidized as the smaller Re ensembles in the Pt-Re surface, as shown in Figure 4.6. However, the surface composition of the Au-Re clusters is not purely Re, as is the case with the monometallic Re surface, and the Au-Re clusters are seen to be more oxidized

than the monometallic Re clusters given the smaller Re ensembles in the bimetallic Au-Re surface. The immiscible nature and composition of the Au-Re clusters explains the extent of oxidation seen for Re in this surface. An additional bimetallic surface was prepared from 2 ML Co + 2 ML Re on TiO_2. Cobalt has a stronger metal-titania interaction than Pt, indicating the bimetallic Co-Re clusters should be smaller than the Pt-Re clusters.[65] However, the extent of Re oxidation in the Co-Re surface is not as great as seen for Re in the Pt-Re surface (Figure 4.6). Co does have a lower surface free energy than Re, and it is comparable to the surface free energy of Pt (2.55 J/m^2 for Co[66] vs. 2.48 J/m^2 for Pt[32]), suggesting Re would diffuse into the Co cluster similarly to the way Re diffuses subsurface in Pt-Re clusters, forming small Re ensembles. This seems evident as Re in the Co-Re clusters is more oxidized than Re in the monometallic and Au-Re clusters. However, the surface composition of the Co-Re clusters becomes complicated in the presence of O_2 due to the oxophillic nature of both Co and Re.[19,67,68] In an oxidizing environment, both Co and Re are expected to be drawn to the surface. Thus, although there is significant Re^{6+} in the Co-Re clusters after oxidation, the lower amount of Re in the higher oxidation states in the Co-Re clusters compared to the Pt-Re clusters may be due to less Re being able to reach the surface when dispersed in Co. Therefore, after exposing this surface to oxidizing conditions, it seems reasonable that the resulting Re oxidation is intermediate between the pure Re surface and bimetallic Pt-Re surface. Unfortunately, this does not provide direct evidence supporting or refuting unique Pt-Re interactions related to enhanced Re oxidation, but it does show that the presence of a second metal such as Au or Co for bimetallic clusters still has a greater extent of oxidation than pure Re clusters.

4.4 Conclusions

The oxidation of monometallic Re and bimetallic Pt-Re surfaces were investigated on single crystal supports of TiO_2(110), HOPG, and Pt(111). It was found that bimetallic surfaces exhibit enhanced Re oxidation over monometallic Re surfaces on both the titania and HOPG supports. These results demonstrate that the lesser extent of Re oxidation in the pure Re clusters is not due to Re-support interactions between Re and the oxide support, but to the probable formation of smaller Re ensembles in the Pt-Re clusters, and the greater amount of undercoordinated Re sites available for oxygen adsorption. However, the oxidation of pure Re clusters on TiO_2 and HOPG displayed comparable Re oxidation, even though Re clusters on TiO_2 are significantly smaller than those on HOPG. Thus, some extent of interaction between the Re clusters and titania support is likely hindering Re oxidation. In addition, thin Re films on Pt(111) displayed a much greater extent of Re oxidation than a thicker Re film. This demonstrates that surfaces consisting of predominantly Re atoms of high coordination to other Re atoms is inhibited from substantial oxygen adsorption and subsequent Re oxidation. The greater extent of Re oxidation for the Au-Re/TiO_2 and Co-Re/TiO_2 surfaces than the pure Re/TiO_2 surface indicates the enhanced Re oxidation in bimetallic surfaces is not unique to Pt-Re interactions. Although the extent of Re oxidation of the Au-Re and Co-Re surfaces was less than that of the Pt-Re surface, this is likely due to the differences in morphology and composition of the bimetallic clusters.

4.5 References

(1) Huang, Z.; Fryer, J. R.; Park, C.; Stirling, D.; Webb, G. Transmission Electron Microscopy and Energy Dispersive X-Ray Spectroscopy Studies of Pt-Re/γ-Al2O3 Catalysts. *J. Catal.* **1994**, *148*, 478–492.

(2) Macleod, N.; Fryer, J. R.; Stirling, D.; Webb, G. Deactivation of Bi- and Multimetallic Reforming Catalysts: Influence of Alloy Formation on Catalyst Activity. *Catal. Today* **1998**, *46*, 37–54.

(3) Fung, A. S.; Kelley, M. J.; Koningsberger, D. C.; Gates, B. C. Gamma-Al_2O_3-Supported Re-Pt Cluster Catalyst Prepared from $Re_2Pt(CO)_{12}$: Characterization by Extended X-Ray Absorption Fine Structure Spectroscopy and Catalysis of Methylcyclohexane Dehydrogenation. *J. Am. Chem. Soc.* **1997**, *119*, 5877–5887.

(4) Azzam, K. G.; Babich, I. V.; Seshan, K.; Lefferts, L. Role of Re in Pt-Re/TiO_2 Catalyst for Water Gas Shift Reaction: A Mechanistic and Kinetic Study. *Appl. Catal. B Environ.* **2008**, *80*, 129–140.

(5) Iida, H.; Igarashi, A. Structure Characterization of Pt-Re/TiO_2 (Rutile) and Pt-Re/ZrO_2 Catalysts for Water Gas Shift Reaction at Low-Temperature. *Appl. Catal. A Gen.* **2006**, *303*, 192–198.

(6) Sato, Y.; Terada, K.; Hasegawa, S.; Miyao, T.; Naito, S. Mechanistic Study of Water-Gas-Shift Reaction over TiO_2 Supported Pt-Re and Pd-Re Catalysts. *Appl. Catal. A Gen.* **2005**, *296*, 80–89.

(7) Duke, A. S.; Xie, K.; Brandt, A. J.; Maddumapatabandi, T. D.; Ammal, S. C.; Heyden, A.; Monnier, J. R.; Chen, D. A. Understanding Active Sites in the Water-Gas Shift Reaction for Pt-Re Catalysts on Titania. *ACS Catal.* **2017**, *7*, 2597–2606.

(8) Wei, Z. H.; Karim, A. M.; Li, Y.; King, D. L.; Wang, Y. Elucidation of the Roles of Re in Steam Reforming of Glycerol over Pt-Re/C Catalysts. *J. Catal.* **2015**, *322*, 49–59.

(9) Kunkes, E. L.; Simonetti, D. A.; Dumesic, J. A.; Pyrz, W. D.; Murillo, L. E.; Chen, J. G.; Buttrey, D. J. The Role of Rhenium in the Conversion of Glycerol to Synthesis Gas over Carbon Supported Platinum-Rhenium Catalysts. *J. Catal.* **2008**, *260*, 164–177.

(10) Zhang, L.; Karim, A. M.; Engelhard, M. H.; Wei, Z. H.; King, D. L.; Wang, Y. Correlation of Pt-Re Surface Properties with Reaction Pathways for the Aqueous-Phase Reforming of Glycerol. *J. Catal.* **2012**, *287*, 37–43.

(11) Ciftci, A.; Ligthart, D. A. J. M.; Sen, A. O.; van Hoof, A. J. F.; Friedrich, H.; Hensen, E. J. M. Pt-Re Synergy in Aqueous-Phase Reforming of Glycerol and the Water-Gas Shift Reaction. *J. Catal.* **2014**, *311*, 88–101.

(12) Ishikawa, Y.; Liao, M.; Cabrera, C. R. Energetics of H_2O Dissociation and CO_{Ads}+ OH_{Ads} Reaction on a Series of Pt-M Mixed Metal Clusters: A Relativistic Density-

Functional Study. *Surf. Sci.* **2002**, *513*, 98–110.

(13) Nijem, S.; Dery, S.; Carmiel, M.; Horesh, G.; Garrevoet, J.; Spiers, K.; Falkenberg, G.; Marini, C.; Gross, E. Bimetallic Pt−Re Nanoporous Networks: Synthesis, Characterization, and Catalytic Reactivity. *J. Phys. Chem. C* **2018**, *122*, 24801–24808.

(14) Prestvik, R.; Moljord, K.; Grande, K.; Holmen, A. The Influence of Pretreatment on the Metal Function of a Commercial Pt–Re/Al_2O_3 Catalyst. *J. Catal.* **1998**, *174*, 119–129.

(15) Daniel, O. M.; DeLaRiva, A.; Kunkes, E. L.; Datye, A. K.; Dumesic, J. A.; Davis, R. J. X-Ray Absorption Spectroscopy of Bimetallic Pt-Re Catalysts for Hydrogenolysis of Glycerol to Propanediols. *ChemCatChem* **2010**, *2*, 1107–1114.

(16) Duke, A. S.; Galhenage, R. P.; Tenney, S. A.; Sutter, P.; Chen, D. A. In Situ Studies of Carbon Monoxide Oxidation on Platinum and Platinum-Rhenium Alloy Surfaces. *J. Phys. Chem. C* **2015**, *119*, 28.

(17) Unger, W.; Baunack, S. Low Pressure Oxygen Adsorption Induced Re Segregation on an Annealed Pt−Re Alloy: A SIMS and AES Study. *Surf. Sci.* **1987**, *184*, L361–L369.

(18) Xie, K. Understanding the Activity of Model Catalyst Surfaces: Ultrahigh Vacuum and Atmospheric Pressure Studies, University of South Carolina, 2016.

(19) Galhenage, R. P.; Xie, K.; Yan, H.; Seuser, G. S.; Chen, D. A. Understanding the Growth, Chemical Activity, and Cluster−Support Interactions for Pt−Re Bimetallic Clusters on TiO_2(110). *J. Phys. Chem. C* **2016**, *120*, 10866–10878.

(20) Duke, A. S.; Xie, K.; Monnier, J. R.; Chen, D. A. Superior Long-Term Activity for a Pt-Re Alloy Compared to Pt in Methanol Oxidation Reactions. *Surf. Sci.* **2017**, *657*, 35–43.

(21) Tenney, S. A.; Xie, K.; Monnier, J. R.; Rodriguez, A.; Galhenage, R. P.; Duke, A. S.; Chen, D. A. Novel Recirculating Loop Reactor for Studies on Model Catalysts: CO Oxidation on Pt/TiO_2(110). *Rev. Sci. Instrum.* **2013**, *84*, 104101.

(22) Chan, A. S. Y.; Wertheim, G. K.; Wang, H.; Ulrich, M. D.; Rowe, J. E.; Madey, T. E. Surface Atom Core-Level Shifts of Clean and Oxygen-Covered Re(1231). *Phys. Rev. B* **2005**, *72*, 35442.

(23) Chan, A. S. Y.; Chen, W. H.; Wang, H.; Rowe, J. E.; Madey, T. E. Methanol Reactions over Oxygen-Modified Re Surfaces: Influence of Surface Structure and Oxidation. *J. Phys. Chem. B* **2004**, *108*, 14643–14651.

(24) Zaera, F.; Somorjai, G. A. The Chemisorption of O_2, CO, D_2 and C_2H_4 over Epitaxially Grown Rhenium Crystalline Films. *Surf. Sci.* **1985**, *154*, 303–314.

(25) Morant, C.; Galan, L.; Sanz, J. M. X-Ray Photoelectron Spectroscopic Study of

the Oxidation of Polycrystalline Rhenium by Exposure to O_2 and Low-Energy O^{2+} Ions. *Anal. Chim. Acta* **1994**, *297*, 179–186.

(26) Liu, P.; Shuh, D. K. Adsorption of O_2 on Polycrystalline Rhenium Metal at Room Temperature Studied by Synchrotron X-Ray Photoemission Spectroscopy. *J. Electron Spectrosc. Relat. Phenom.* **2001**, *114*, 319–325.

(27) Tysoe, W. T.; Zaera, F.; Somorjai, G. A. An XPS Study of the Oxidation and Reduction of the Rhenium Platinum System under Atmospheric Conditions. *Surf. Sci.* **1988**, *200*, 1–14.

(28) Yuan, Y. Z.; Shido, T.; Iwasawa, Y. The New Catalytic Property of Supported Rhenium Oxides for Selective Oxidation of Methanol to Methylal. *Chem. Commun.* **2000**, 1421–1422.

(29) Okal, J.; Tylus, W.; Kepinski, L. XPS Study of Oxidation of Rhenium Metal on Gamma-Al_2O_3 Support. *J. Catal.* **2004**, *225*, 498–509.

(30) Ducros, R.; Fusy, J. Core Level Binding Energy Shifts of Rhenium Surface Atoms for a Clean and Oxygenated Surface. *J. Electron Spectrosc. Relat. Phenom.* **1987**, *42*, 305–312.

(31) Duke, A. S.; Galhenage, R. P.; Tenney, S. A.; Ammal, S. C.; Heyden, A.; Sutter, P.; Chen, D. A. In Situ Ambient Pressure X-Ray Photoelectron Spectroscopy Studies of Methanol Oxidation on Pt(111) and Pt–Re Alloys. *J. Phys. Chem. C* **2015**, *119*, 23082–23093.

(32) de Boer, F. R.; Boom, R.; Mattens, W. C. M.; Miedema, A. R.; Niessen, A. K. *Cohesion in Metals: Transition Metal Alloys*; Vol. 1.; North-Holland Physics Publishing: Amsterdam, 1998.

(33) Mitra, B.; Gao, X. T.; Wachs, I. E.; Hirt, A. M.; Deo, G. Characterization of Supported Rhenium Oxide Catalysts: Effect of Loading, Support and Additives. *Phys. Chem. Chem. Phys.* **2001**, *3*, 1144–1152.

(34) Chądzyński, G. W.; Kubicka, H. Chemisorption of Hydrogen and Oxygen on γ-Alumina-Supported Rhenium: Part II. Chemisorption of Oxygen and Hydrogen-Oxygen Titration. *Thermochim. Acta* **1990**, *158*, 369–383.

(35) Howells, A.; Harris, T.; Sashikata, K.; Chottiner, G. S.; Scherson, D. A. Model Systems in Electrocatalysis: Electronic and Structural Characterization of Vapor Deposited Platinum on the Basal Plane of Highly Oriented Pyrolytic Graphite. *Solid State Ionics* **1997**, *94*, 115–121.

(36) Marcus, P.; Hinnen, C. XPS Study of the Early Stages of Deposition of Ni, Cu and Pt on HOPG. *Surf. Sci.* **1997**, *392*, 134–142.

(37) Howells, A. R.; Hung, L.; Chottiner, G. S.; Scherson, D. A. Effects of Substrate Defect Density and Annealing Temperature on the Nature of Pt Clusters Vapor Deposited on the Basal Plane of Highly Oriented Pyrolytic Graphite. *Solid State*

Ionics **2002**, *150*, 53–62.

(38) Venugopal, A.; Pirkle, A.; Wallace, R. M.; Colombo, L.; Vogel, E. M. Contact Resistance Studies of Metal on HOPG and Graphene Stacks. *AIP Conf. Proc.* **2009**, *1173*, 324.

(39) Okal, J. A Study of Effect of Particle Size on the Oxidation of Rhenium in the Re/Gamma-Al_2O_3 Catalysts. *Appl. Catal. A* **2005**, *287*, 214–220.

(40) Wang, C.-B.; Yeh, C.-T. Effects of Particle Size on the Progressive Oxidation of Nanometer Platinum by Dioxygen. *J. Catal.* **1998**, *178*, 450–456.

(41) Wang, C.-B.; Yeh, C.-T. Calorimetric Study on Oxidation of Alumina Supported Rhodium by Dioxygen. *J. Mol. Catal. A Chem.* **1997**, *120*, 179–184.

(42) Ho, Y.-S.; Wang, C.-B.; Yeh, C.-T. Calorimetric Study on Interaction of Dioxygen with Alumina Supported Palladium. *J. Mol. Catal. A Chem.* **1996**, *112*, 287–294.

(43) Galhenage, R. P.; Xie, K.; Diao, W.; Tengco, J. M. M.; Seuser, G. S.; Monnier, J. R.; Chen, D. A. Platinum-Ruthenium Bimetallic Clusters on Graphite: A Comparison of Vapor Deposition and Electroless Deposition Methods. *Phys. Chem. Chem. Phys.* **2015**, *17*, 28354–28363.

(44) Yuan, Z.; Hanf, M. C.; Stephan, R.; Dulot, F.; Denys, E.; Florentin, A.; Harbich, W.; Wetzel, P. Growth of Palladium Nanoparticles on Nanostructured Highly Ordered Pyrolytic Graphite. *Surf. Interface Anal.* **2015**, *47*, 82–86.

(45) Yang, D.-Q.; Piyakis, K. N.; Sacher, E. The Manipulation of Cu Cluster Dimensions on Highly Oriented Pyrolytic Graphite Surfaces by Low Energy Ion Beam Irradiation. *Surf. Sci.* **2003**, *536*, 67–74.

(46) Seuser, G. S. Understanding the Adsorption and Nucleation of Transition Metals on a Model Carbon Support, University of South Carolina, 2018.

(47) Shcheglov, P. A.; Drobot, D. V. Heterogeneous Equilibria in the Rhenium-Oxygen System. *Russ. J. Phys. Chem.* **2006**, *80*, 1819–1825.

(48) Okal, J.; Kepinski, L.; Krajczyk, L.; Tylus, W. Oxidation and Redispersion of a Low-Loaded Re/Gamma-Al_2O_3 Catalyst. *J. Catal.* **2003**, *219*, 362–371.

(49) Shpiro, E. S.; Ryashentseva, M. A.; Minachev, K. M.; Antoshin, G. V; Avaev, V. I. XPS Studies of the Rhenium State in Supported Re Catalysts. *J. Catal.* **1978**, *55*, 402–406.

(50) Naor, A.; Eliaz, N.; Burstein, L.; Gileadi, E. Direct Experimental Support for the Catalytic Effect of Iron-Group Metals on Electrodeposition of Rhenium. *Electrochem. Solid State Lett.* **2010**, *13*, D91–D93.

(51) Bazuev, G. V; Chupakhina, T. I.; Korolyov, A. V; Kuznetsov, M. V. Synthesis under Usual Conditions, X-Ray Photoelectron Spectroscopy and Magnetic

Properties of $Re_{1-x}Mn_xO_2$ Oxides with Rutile Structure. *Mater. Chem. Phys.* **2010**, *124*, 946–951.

(52) Nikonova, O. A.; Capron, M.; Fang, G.; Faye, J.; Mamede, A.-S. S.; Jalowiecki-Duhamel, L.; Dumeignil, F.; Seisenbaeva, G. A. Novel Approach to Rhenium Oxide Catalysts for Selective Oxidation of Methanol to DMM. *J. Catal.* **2011**, *279*, 310–318.

(53) Tatarenko, S.; Dolle, P.; Morancho, R.; Alnot, M.; Ehrhardt, J. J.; Ducros, R. XPS and UPS Study of Oxygen-Adsorption on Re(0001) at Low-Temperatures. *Surf. Sci.* **1983**, *134*, L505–L512.

(54) Miniussi, E.; Hernandez, E. R.; Pozzo, M.; Baraldi, A.; Vesselli, E.; Comelli, G.; Lizzit, S.; Alfe, D. Non-Local Effects on Oxygen-Induced Surface Core Level Shifts of Re(0001). *J. Phys. Chem. C* **2012**, *116*, 23297–23307.

(55) Brandt, A. J.; Maddumapatabandi, T. D.; Shakya, D.; Farzandh, S.; Chen, D. A. Water-Gas Shift Activity of Pt-Re Clusters and the Role of the Support. *Manuscr. Prep.*

(56) Räty, J.; Pakkanen, T. A. Controlled Stepwise Preparation of Alumina Supported $Re_2(CO)_{10}$ Catalysts by Gas-Phase Adsorption Technique: TPR, TPO and Pulse Chemisorption Study. *J. Mol. Catal. A Chem.* **2001**, *166*, 275–281.

(57) Godbey, D. J.; Garin, F.; Somorjai, G. A. The Hydrogenolysis of Ethane Over Re-Pt(111) and Pt-Re(0001) Bimetallic Crystal Surfaces. *J. Catal.* **1989**, *117*, 144–154.

(58) *Binary Alloy Phase Diagrams*; Massalski, T. B.; Okamoto, H.; Subramanian, P. R.; Kacprzak, L., Eds.; 2nd ed.; ASM International: Materials Park, OH, 1990.

(59) Ramstad, A.; Strisland, F.; Raaen, S.; Worren, T.; Borg, A.; Berg, C. Growth and Alloy Formation Studied by Photoelectron Spectroscopy and STM. *Surf. Sci.* **1999**, *425*, 57–67.

(60) Mun, B. S.; Rossi, M.; Ross, P. N. The Study of Surface Segregation of Re_3Pt Polycrystalline Alloy with Photoelectron Spectroscopy. *J. Chem. Phys.* **2008**, *129*, 174707.

(61) Godbey, D. J.; Somorjai, G. A. The Adsorption and Desorption of Hydrogen and Carbon Monoxide on Bimetallic Re-Pt(111) Surfaces. *Surf. Sci.* **1988**, *204*, 301–318.

(62) Kondarides, D. I.; Verykios, X. E. Interaction of Oxygen with Supported Ag–Au Alloy Catalysts. *J. Catal.* **1996**, *158*, 363–377.

(63) Tsud, N.; Sutara, F.; Matolinova, I.; Veltruska, K.; Dudr, V.; Prince, K. C.; Matolin, V. Interaction of Oxygen with Au/Ti(0001) Surface Alloys Studied by Photoelectron Spectroscopy. *J. Phys. Condens. Matter* **2010**, *22*, 265002.

(64) Zhang, L.; Persaud, R.; Madey, T. E. Ultrathin Metal Films on a Metal-Oxide Surface: Growth of Au on TiO_2(110). *Phys. Rev. B* **1997**, *56*, 10549–10557.

(65) Galhenage, R. P.; Yan, H.; Tenney, S. A.; Park, N.; Henkelman, G.; Albrecht, P.; Mullins, D. R.; Chen, D. A. Understanding the Nucleation and Growth of Metals on TiO_2: Co Compared to Au, Ni and Pt. *J. Phys. Chem. C* **2013**, *117*, 7191–7201.

(66) Skriver, H. L.; Rosengaard, N. M. Surface Energy and Work Function of Elemental Metals. *Phys. Rev. B* **1992**, *46*, 7157.

(67) Andersson, M.; Persson, J. L.; Rosén, A. Reactivity of Fe_n, Co_n, and Cu_n Clusters with O_2 and D_2 Studied at Single-Collision Conditions. *J. Phys. Chem.* **1996**, *100*, 12222–12234.

(68) Kepp, K. P. A Quantitative Scale of Oxophilicity and Thiophilicity. *Inorg. Chem* **2016**, *55*, 9461–9470.

CHAPTER 5

ELUCIDATING ELECTRONIC PROPERTIES THROUGH THE STUDY OF BIMETALLIC NODES IN METAL-ORGANIC FRAMEWORKS

5.1 Introduction

The steady advancement in technology over the years has resulted in the continuous evolvement of material design for the development and improvement of energy-efficient electronic devices and sensors.[1–4] On this basis, research in this field has focused on exploring different strategies toward the emergence of new materials with enhanced electrical and ionic conductivity.[5–7] Recently, metal-organic frameworks (MOFs), a class of hybrid crystalline and porous materials, have received intense attention in potential electronic device applications owing to their unique intrinsic adjustable properties.[8–11] A few reports have shown the tunability of electronic properties of MOFs through the incorporation of molecules proficient in charge transfer as guests in their pores.[12–15] Furthermore, conductivity in MOFs has also shown to be enhanced by modifying the organic and/or inorganic components of their structure.[16–18]

Very recently, a study conducted in collaboration with our lab demonstrated that electronic properties of MOFs can be effectively tuned by metal node engineering, a strategy that stands out as it distinctively preserves MOF porosity and crystallinity while improving the electrical conductivity.[19] Using a wide range of characterization techniques, it was shown that by incorporating a second metal into a monometallic MOF framework in three different unique ways, the conductive properties of the resulting

bimetallic MOFs could effectively improve. Interestingly, other recent reports have suggested enhancements in various applications such as sensing, gas adsorption, catalysis, and energy storage as a result of the bimetallic property of particular MOFs.[20–23] The effect of factors such as type of secondary building unit (SBU), nature of incorporated metals, and solvent systems have been addressed for the synthesis of bimetallic MOFs.[24–26] However, the study of such factors as topology, ensemble size of SBU, nature of the metal, and presence of unsaturated metal sites have not been investigated for their specific effects on the electronic properties of bimetallic MOFs.

To elucidate the parameters that affect the electronic properties of MOFs, this work probed the changes in the electronic structure as a function of metal ensemble size (i.e., number of metal ions in the SBU), identity of metals in the nodes, SBU geometry, and presence (or absence) of unsaturated metal sites. Systems containing monomeric, dimeric, and pentameric metal nodes were selected: M-(HHTP) (monomeric, HHTP = 2,3,5,6,10,11-hexahydroxytriphenylene), M_2-(BTC) (dimeric, BTC = 1,3,5-benzenetricarboxylate), and M_5-(NIP) (pentameric, NIP = (5-nitroisophthalate). In all systems, the monometallic MOF was first characterized, followed by transmetallation procedures to study the cooperative effect of two different metals for the bimetallic analogs. The bimetallic frameworks contained the following pairs: CuCo, CuRh, CuFe, CuMn, CuRu, and CuNi. The resulting effects brought about from changes in the MOF parameters were studied through Raman spectroscopy, X-ray photoelectron spectroscopy (XPS), and conductivity measurements.

5.2 Experimental

Materials

$Cu(NO_3)_2 \cdot 2.5H_2O$ (98.3%, Mallinckrodt AR), $Cu(OAc)_2 \cdot H_2O$ (>95%, TCI America), $CoCl_2 \cdot 6H_2O$ (>98.0%, TCI America), $Co(OAc)_2 \cdot 4H_2O$ (98%, Alfa Aesar), $MnCl_2 \cdot 4H_2O$ (98.0-101.0%, Alfa Aesar), $FeCl_2 \cdot 4H_2O$ (reagent grade, Ward's Science), $Zn(NO_3)_2 \cdot 6H_2O$ (technical grade, Ward's Science), $RuCl_3 \cdot XH_2O$ (98%, Oakwood Chemical), $RhCl_3 \cdot XH_2O$ (99.98%, Engelhard Chemicals), 1,3,5-benzenetricarboxylic acid (98%, Alfa Aesar), 5-Nitroisophthalic acid (98%, BeanTown Chemical), 2,3,6,7,10,11-hexahydroxytriphenylene (95%, Acros Chemical), N,N′-dimethylformamide (ACS grade, BDH), methanol (>99.8%, HPLC grade, Fisher Scientific), acetone (ACS grade, BDH), ethanol (200 proof, Decon Laboratories, Inc.), were used as received.

Synthesis of Monometallic MOFs

$Cu_3(BTC)_2$: A mixture of $Cu(NO_3)_2 \cdot 2.5H_2O$ (700 mg, 3.01 mmol), H_3BTC (470 mg, 2.24 mmol), and DMF: H_2O: EtOH (1 : 1 : 1 – 30.0 mL) was sonicated in a 40 mL vial for about 5 mins. The mixture was heated at 75 °C in an oven for 24 h. After cooling to room temperature, the blue crystallites of $Cu_3(BTC)_2$ were collected by filtration and washed thoroughly three times with DMF (3 × 20 mL).

$Cu_5(NIP)_4$: A mixture of $Cu(OAc)_2 \cdot H_2O$ (199 mg, 1.00 mmol), H_2NIP (213 mg, 1.00 µmol), and H_2O (10 mL) was sonicated in a flask for about 10 mins and stirred for about 30 mins. The blue jell-like mixture obtained was then transferred to a Parr reaction vessel and heated at 120 °C in an oven for 48 h. The blue powder obtained was washed twice with water (2 × 20 mL). and then thrice with DMF (3 × 20 mL).

$Co_3(HHTP)_2$: A mixture of $Co(OAc)_2 \cdot 4H_2O$ (55.0 mg, 0.222 mmol), HHTP (36.0 mg, 0.111 mmol), and H_2O (3.20 mL) was sonicated in a 20 mL vial for about five mins and heated with stirring on a hotplate at 85 °C overnight. The dark powder obtained was washed twice with water (2 × 20 mL) and then thrice with acetone (3 × 20 mL).

$Cu_3(HHTP)_2$: A mixture of $Cu(OAc)_2 \cdot H_2O$ (68.5 mg, 0.275 mmol), HHTP (36.0 mg, 0.111 mmol), and H_2O (3.20 mL) were sonicated in a 20 mL vial for about five mins and heated with stirring on a hotplate at 85 °C overnight. The dark powder obtained was washed twice with water (2 × 20 mL) and then thrice with acetone (3 × 20 mL).

Synthesis of Bimetallic MOFs

$Cu_{3-x}Co_x(BTC)_2$: The preparation of $Cu_{1.5}Co_{1.5}(BTC)_2$ was done by heating $Cu_3(BTC)_2$ (0.135 g, 0.203 mmol) in a solution of $CoCl_2 \cdot 6H2O$ in DMF (0.441 M, 10 mL) at 90 °C for 24 h in an isothermal oven. After 24 h of heating, the reaction mixture was cooled down to room temperature, and the resulting green powder was washed thoroughly with DMF to remove excess cobalt chloride salt. After DMF washing, the powder underwent a solvent exchange process with dichloromethane at room temperature. The solvent was replaced twice a day over 72 h.

$Cu_{3-x}Rh_x(BTC)_2$: The preparation of $Cu_{2.01}Rh_{0.99}(BTC)_2$ was done by stirring a mixture of $Cu_3(BTC)_2$ powders (226 mg, 0.374 mmol) and 0.0386M ethanol solution (5.00 mL) of $RhCl_3 \cdot H_2O$ in a flask for three days at 90 °C on a hotplate. The green powder obtained was collected by filtration and thoroughly washed several times with ethanol to remove any residual $RhCl_3$ salt.

$Cu_{3-x}Fe_x(BTC)_2$. For the preparation of $Cu_{2.25}Fe_{0.75}(BTC)_2$, 450 mg (0.744 mmol) of $Cu_3(BTC)_2$ crystals were heated in a 20 mL vial containing 0.0670 M DMF solution

(10.0 mL) of $FeCl_2 \cdot 4H_2O$ for three days at 90 °C in a preheated oven. Crystals were thoroughly washed with DMF several times to completely remove any residual $FeCl_2 \cdot 4H_2O$ salt. The solvent was then exchanged with ethanol for three days, and was refreshed twice daily.

$Cu_{3-x}Mn_x(BTC)_2$. For the preparation of $Cu_{1.56}Mn_{0.1.44}(BTC)_2$, 450 mg (0.744 mmol) of $Cu_3(BTC)_2$ crystals were heated in a 20 mL vial containing 0.250 M DMF solution (10.0 mL) of $MnCl_2 \cdot 4H_2O$ for three days at 90 °C in a preheated oven. Crystals were thoroughly washed with DMF several times to completely remove any residual $MnCl_2 \cdot 4H_2O$ salt. The solvent was then exchanged with ethanol for three days, and was refreshed twice daily.

$Cu_{3-x}Ru_x(BTC)_2$. For the preparation of $Cu_{2.73}Ru_{0.27}(BTC)_2$, a mixture of $Cu(NO_3)_2 \cdot 2 \cdot 5H_2O$ (226 mg, 0.970 mmol), $RuCl_3 \cdot H_2O$ (201 mg, 0.970 mmol), H_3BTC (492 mg, 2.34 mmol), ethanol (25.0 mL), and DMF (25.0 mL) was heated in a flask at 60 °C for three days. The blue-green powder obtained was collected by filtration and thoroughly washed several times with ethanol to remove any residual $RuCl_3$ salt.

$Cu_{3-x}Ni_x(BTC)_2$. For the preparation of $Cu_{2.82}Ni_{0.18}(BTC)_2$, freshly prepared $Cu_3(BTC)_2$ (0.135 g, 0.203 mmol) and a solution of $NiCl_2 \cdot 6H_2O$ (0.33 M, 10 mL DMF) were heated at 90 °C for 24 h in a 10 mL vial in an anisothermal oven. After 24 h of heating, the reaction mixture was cooled down to room temperature, and the resulting green powder was washed thoroughly with DMF to remove any excess nickel chloride.

$Cu_{5-x}Rh_x(NIP)_4$. For the preparation of $Cu_{4.82}Rh_{0.18}(NIP)_4$, a mixture of $Cu_5(NIP)_4$ powder (377 mg, 0.275 mmol) was gently stirred in a 0.0386 M DMF solution

(3.00 mL) of $RhCl_3 \cdot H_2O$ in a 20 mL vial for 5 h at 60 °C on a hotplate. The solvent was then exchanged with methanol for three days, and was refreshed twice daily.

$Cu_{5-x}Fe_x(NIP)_4$. For the preparation of $Cu_{4.40}Fe_{0.60}(NIP)_4$, 399 mg (0.291 mmol) of $Cu_5(NIP)_4$ powder was immersed in a 0.0670 M DMF solution of $FeCl_2 \cdot 4H_2O$ (3.00 mL) in a 20 mL vial for 1 h at room temperature. The green powder obtained was thoroughly washed with DMF several times to completely remove any residual metal salt. The solvent was then exchanged with methanol for three days, and was refreshed twice daily.

$Cu_{5-x}Mn_x(NIP)_4$. For the preparation of $Cu_{4.82}Mn_{0.18}(NIP)_4$, $Cu_5(NIP)_4$ powder (399 mg, 0.291 mmol) was soaked in a 0.250 M DMF solution of $MnCl_2 \cdot 4H_2O$ (1.50 mL) in a 20 mL vial for 3.5 h at room temperature. The green powder obtained was thoroughly washed with DMF several times to completely remove any residual metal salt. The solvent was then exchanged with methanol for three days, and was refreshed twice daily.

$Co_{3-x}Cu_x(HHTP)_2$. For the preparation of $Co_{0.51}Cu_{2.49}(HHTP)_2$, a mixture of 20.0 mg of $Co_3(HHTP)_2$ powder was stirred in a 0.069 M aqueous solution of $Cu(OAc)_2 \cdot H_2O$ (1.00 mL) overnight at 85 °C on a hotplate. The dark powder obtained was collected by filtration and washed twice with water (2 × 20 mL) and then thrice with acetone (3 × 20 mL).

Physical Measurements

X-ray diffraction (XRD) studies of the monometallic and bimetallic samples were done on a Bruker AXS D8 Advance diffractometer using a Cu Kα (λ = 1.5406 Å) radiation operating at a voltage of 40 kV and a current of 40 mA. Powder X-ray

diffraction patterns were recorded on a Rigaku Miniflex II diffractometer with accelerating voltage and current of 30 kV and 15 mA, respectively.

ICP-AES analysis was conducted using a Finnigan ELEMENT XR double focusing magnetic sector field inductively coupled plasma-mass spectrometer (SF-ICP-MS) with Ir and/or Rh as internal standards. A Micromist U-series nebulizer (0.2 ml/min, GE, Australia), quartz torch, and injector (Thermo Fisher Scientific, USA) were used for sample introduction. Sample gas flow was 1.08 mL/min, and the forwarding power was 1250 W. The samples were digested in Teflon vessels with nitric and hydrochloric acids and then heated at 180 °C for 4 h. All ICP-AES studies were performed on samples that underwent an extensive washing procedure (~1 week) using the Soxhlet apparatus to remove residual salts used for the second metal integration.

X-ray photoelectron spectroscopy measurements (XPS) were performed using a Kratos AXIS Ultra DLD XPS system equipped with a monochromatic Al Kα source operated at 15 keV and 8 mA, and a hemispherical energy analyzer. This system has been described previously.[19,27] Analysis was performed at a pressure below 2×10^{-8} Torr. To compensate for charging in the powders, a charge neutralizer was used by bombarding the sample with low-energy electrons. A step size of 0.06 eV and dwell time of 800 ms was used for the O(1s), C(1s), N(1s), Cl(2p), and Cu($L_3M_5M_5$) regions; and a dwell time of 1600 ms for Cu(2p), Co(2p), Rh(3d), Fe(2p), Mn(2p), Ru(3p), Ni(2p), and the valence band regions was used. Survey scans were also collected to ensure there were no contaminants present. The binding energies were set according to the position of adventitious carbon at 284.8 eV. Prior to XPS measurements, all samples were activated

according to the values listed in Table 5.1. The samples were then transported to the XPS facility in evacuated or N_2 purged vials in a hot aluminum block.

Raman spectroscopic measurements were carried out using an XploRA PLUS, HORIBA confocal microscope coupled with a TE air cooled CCD detector. Samples were analyzed in powder form by excitation of a 473 nm solid state laser (25 mW) focused onto the surface of the samples with a microscope objective lens (50× LWD). Samples were scanned from 200 to 3600 cm^{-1} at a spectral resolution of 1.2 cm^{-1}.

Conductivity measurements were performed on MOF pressed pellets held in a 2 mm diameter quartz tube pressed between two stainless steel contacts. Measurements were collected using a sourcemeter (Keithley Instruments GmbH, Germering, Germany, model 263) and an electrometer (Keithley Instruments GmbH, Germering, Germany, model 617).[28]

5.3 Results and Discussion

Preparation of Monometallic and Bimetallic Systems

The framework $Cu_3(BTC)_2(H_2O)_3$ ($Cu_3(BTC)_2$) consists of dimeric SBUs (Figure 5.1a), and was used as a precursor for the bimetallic M_2-(BTC) MOFs containing CuCo CuRh, CuFe, CuMn, CuRu, and CuNi metal pairs. The compositions of the bimetallic MOFs are listed in Table 5.1, along with the time and temperature for transmetallation and activation.

The $Cu_5(OH)_2(NIP)_4(H_2O)_6{\cdot}(H_2O)_5$ ($Cu_5(NIP)_4$) framework was used as a precursor to synthesize MOFs containing pentameric SBUs (Figure 5.1b). $Cu_5(NIP)_4$ was transmetallated to form bimetallic M_5-(NIP) MOFs of CuRh, CuFe, and CuMn (Table 5.1).

The M-(HHTP) (M = Cu, Co) framework consists of monomeric SBUs (Figure 5.1c). In contrast to the three-dimensional M_2-(BTC) and M_5-(NIP) systems, the M-(HHTP) structure forms two-dimensional layers, with iteration dependent on the metal. For instance, $Cu_3(HHTP)_2$ posses the slipped-parallel (AAAA) staking configuration, while $Co_3(HHTP)_2$ possess interpolated (ABAB) stacking. The monometallic $Co_3(HHTP)_2$ framework was used as a precursor for the synthesis of CoCu-(HHTP).

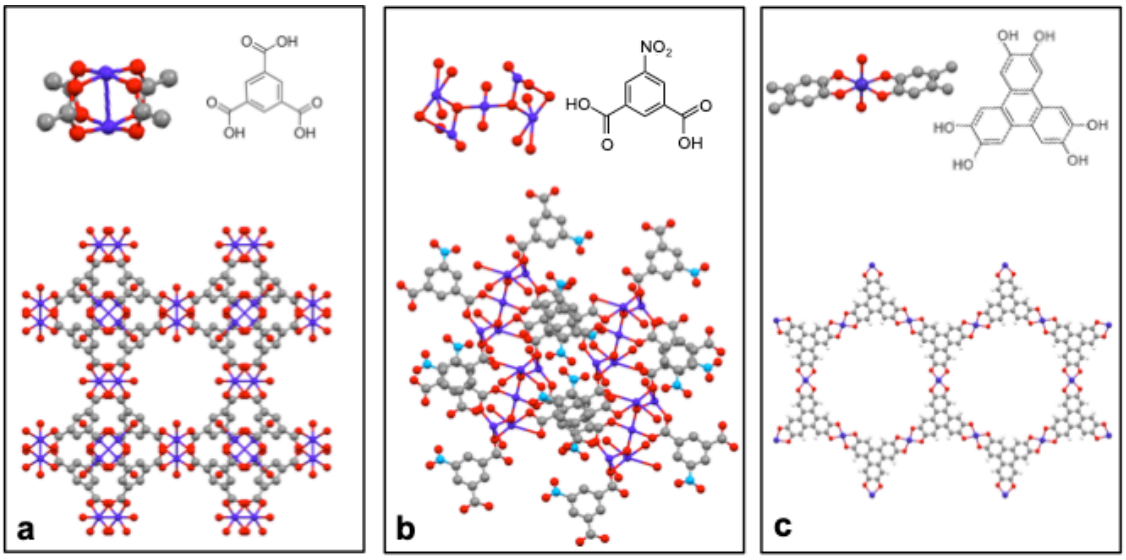

Figure 5.1: Metal node, organic ligand, and MOF structure for a) M_2-(BTC); b) M_5-(NIP); c) M-(HHTP). Purple, red, cyan, and gray spheres represent metal, oxygen, nitrogen, and carbon atoms.

Characterization by ICP-AES was used to determine the ratio of metals in the bimetallic frameworks. All samples underwent an extensive washing procedure (~1 week) using the Soxhlet apparatus to remove residual salts used for the second metal integration. PXRD was performed after synthesis of the monometallic precursors and after transmetallation to ensure crystallinity of the prepared bimetallic MOFs. The activation procedures listed in Table 5.1 were used to remove coordinated solvent molecules and water prior to XPS measurements.

Table 5.1 Composition, Exchange Procedure, and Activation Method for prepared MOFs

Bimetallic MOFs	Exchange Procedure Temp, Time	Activation Method Temp, Time
$Cu_3(BTC)_2$	---	160 °C, 48 h
$Cu_{1.5}Co_{1.5}(BTC)_2$	90 °C, 24 h	120 °C, 48 h
$Cu_{2.01}Rh_{0.99}(BTC)_2$	90 °C, 72 h	160 °C, 24 h
$Cu_{2.25}Fe_{0.75}(BTC)_2$	90 °C, 72 h	200 °C, 24 h
$Cu_{1.56}Mn_{1.44}(BTC)_2$	90 °C, 72 h	200 °C, 24 h
$Cu_{2.73}Ru_{0.27}(BTC)_2$	60 °C, 72 h	160 °C, 24 h
$Cu_{2.82}Ni_{0.18}(BTC)_2$	90 °C, 24 h	120 °C, 48 h
$Cu_5(NIP)_4$	---	100 °C, 48 h
$Cu_{4.82}Rh_{0.18}(NIP)_4$	60 °C, 5 h	85 °C, 6 h
$Cu_{4.40}Fe_{0.60}(NIP)_4$	rt, 1 h	85 °C, 12 h
$Cu_{4.82}Mn_{0.18}(NIP)_4$	rt, 3 h	85 °C, 12 h
$Co_3(HHTP)_2$	---	85 °C, 12 h
$Cu_3(HHTP)_2$	---	85 °C, 12 h
$Co_{0.51}Cu_{2.49}(HHTP)_2$	85 °C, 16 h	85 °C, 12 h

Raman Spectroscopy

The metal distribution within the bimetallic frameworks is important for understanding the electronic properties of the MOF materials, particularly of the multinuclear metal nodes. The dimeric nodes of the CuCo-BTC MOF was chosen as a model system for study. The Raman spectra of two CuCo-BTC samples with different concentrations are shown in Figure 5.2 along with Cu-BTC for comparison. The resonances below 600 cm^{-1} were attributed to copper-related modes (e.g., the 505 cm^{-1} resonance was assigned to the Cu–O stretching mode).[29,30] Characteristic modes of the BTC^{3-} linker appeared in the range of 1800 to 730 cm^{-1}.[31] The resonances at 1616 cm^{-1}

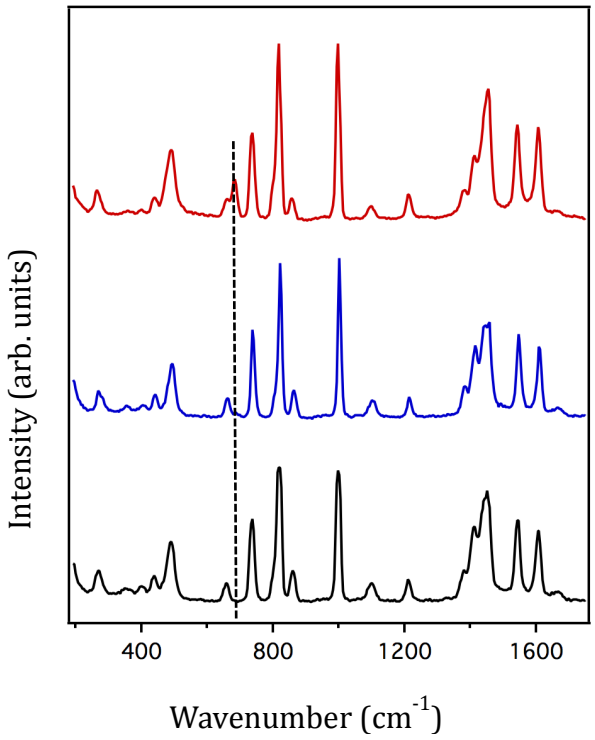

Figure 5.2: Raman spectra for: CuBTC (black); CuCo(9)BTC (blue); and CuCo(21)BTC (red). The % composition of Co is given in parenthesis for the bimetallic MOFs.

and 1547 cm^{-1} were attributed to the C=C stretching modes of phenyl rings, and the asymmetric υ_{as} (COO^{-}) and symmetric stretching υ_{s} (COO^{-}) vibrations of the linker carboxylate groups appeared at 1467 cm^{-1} and 1388 cm^{-1}.[29,30] The strong resonances at 826 and 740 cm^{-1} were ascribed to the out-of-plane C–H bending modes in the linker.[29,31] When 9% of the Cu ions were substituted with Co in the $Cu_3(BTC)_2$ structure, the Raman spectrum was unchanged from that of pure $Cu_3(BTC)_2$ except for the appearance of a small peak at 684 cm^{-1}. Furthermore, when the Co concentration in CuCo-BTC was increased to 21%, a pronounced peak at 684 cm^{-1} was observed. Theoretical calculations that modeled the Cu-Co node with acetate linkers found that the 684 cm^{-1} peak is associated with a rocking motion of the C_2O_4 ligands attached to the metal-metal dimer and an in-phase rotation about the C-C axes. Notably, the calculations do not predict this

vibration for CuBTC itself, and therefore the observed increase in intensity of this peak with increasing Co concentration from 9 to 21% is consistent with this assignment.

Valence band and Oxidation States

XPS provides a powerful tool for rapid evaluation of the electronic structure and oxidation states for a large number of samples; in this manner, MOFs with potentially interesting electronic behavior can be quickly identified.[19] Specifically, XPS of the valence band region provides information about density of states (DOS) near the Fermi level (E_F, binding energy = 0 eV) All of the monometallic and bimetallic MOFs were studied by XPS after thermal treatment (Table 5.1) to remove coordinated solvent molecules and water before introduction into the vacuum chamber. PXRD analysis confirmed the structural integrity of the MOF framework after activation. For all samples, XPS measurements were collected of the valence band region, in addition to the O(1s), C(1s), Cu($2p_{3/2}$), and second metal regions.

Valence band spectra for the Cu-containing MOFs are shown in Figure 5.3. In all cases, the valence band intensities were normalized for the total amount of material sampled based on the integrated O(1s) signals, the number of oxygen atoms/unit cell, and the total unit cell volume. For the pure Cu-BTC, the intensity of the valence band is nearly zero between 0 eV and 1.5 eV, which is characteristic of an insulating material (Figure 5.3a). In contrast, the CuM'-BTC (M'= Co, Rh) MOFs have valence band edges with intensity extending nearly to 0 eV (Figure 5.3a). This behavior suggests that there should be better conductivity due to a greater number of electronic states near the Fermi level when Co or Rh ions are substituted for some of the Cu ions. For all of the other

bimetallic MOFs investigated (M'=Fe, Mn, Ru, Ni) the valence band edges were similar to that of the insulating pure Cu-BTC.

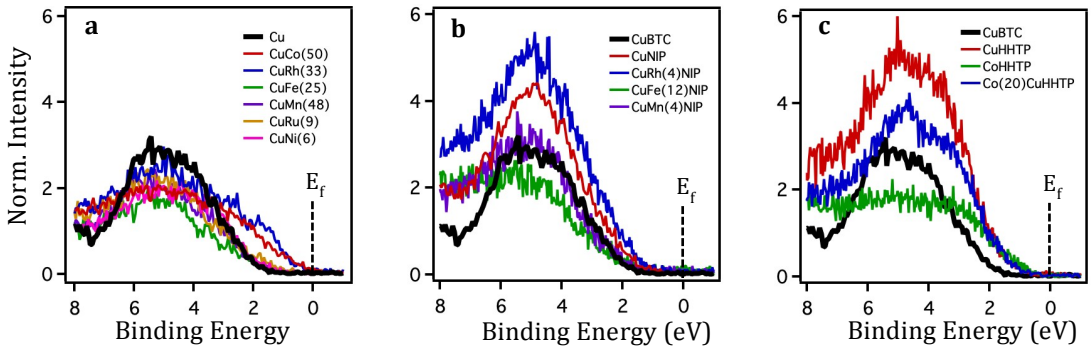

Figure 5.3: XPS valence band spectra for Cu-containing MOFs with a) BTC; b) NIP; and c) HHTP ligands. The percentage of the second metal is given in parenthesis. The CuBTC spectrum is shown in black as a reference point in all three graphs, and the intensities have been normalized to account for different amounts of material sampled for each MOF powder (see text for more details).

The interesting behavior of Co incorporation was recently analyzed in a detailed comparison of CuCo-BTC and CuCo-BTB(bp) (BTB = benzene-1,3,5-tribenzoate, bp = 4,4′-bipyridyl) in our previous work.[19] For CuCo-BTC, XPS measurements of the valence band region exhibited nonzero intensity near E_F, which is characteristic of semiconductors. However, the valence band spectrum of CuCo-BTB(bp) resembled that of an insulator, with little intensity near the Fermi level.[19] This demonstrated the effect that differences in MOF structure can have on the apparent density of states observed in the valence band.

Since CuRh-BTC also displayed a valence band edge with intensity near E_F, the CuRh-NIP system was studied to further explore the effect of Rh integration on the electronic structure of Cu-based MOFs (Figure 5.3b). The M_5-NIP MOFs have a pentameric SBU, as opposed to the dimeric SBU in M_2-BTC. In comparison to Cu-BTC (black trace), the valence band edge for CuRh-NIP is shifted to lower binding energy,

indicating a greater DOS near E_F for another MOF containing mixed Cu-Rh nodes. Furthermore, the valence band edge for Cu-NIP itself appears at lower binding energy than for Cu-BTC, and this suggests that the ligand also plays a significant role in determining DOS near the Fermi level. However, the shift to lower binding energy for the valence band of Cu-NIP is not as great as for CuRh-NIP. Furthermore, the incorporation of other metals such as Mn or Fe into the Cu-NIP MOF did not significantly alter the position of the valence band edge.

Despite a number of literature examples demonstrating metallic or semiconducting behavior for Fe-containing MOFs,[16,32,33] the valence band spectra of the CuFe-BTC and CuFe-NIP MOFs exhibit zero intensity within ~1.5 eV of E_F, which is typical for insulating materials. Thus, the incorporation of Fe ions into both Cu-containing MOFs is not accompanied with increased DOS near the Fermi level, regardless of the SBU geometry.

In contrast to M_5-(NIP) and M_2-(BTC) systems, $Cu_3(HHTP)_2$ has a two-dimensional structure as well as relatively high intrinsic conductivity.[34] The valence band edge of Cu-HHTP lies closer to E_F, than that of Cu-BTC (shown in black, Figure 5.3c), as expected based on its higher conductivity. For CoCu-HHTP, the position of the valence band edge remains unchanged compared to monometallic Cu-HHTP, and therefore Co incorporation does not appear to have a substantial impact on the DOS near the Fermi level in this case.

The Cu(2p) regions for the Cu-containing MOFs (Figure 5.4) all had a major peak at a binding energy of 935 eV, which corresponds to Cu^{2+}, as previously observed for Cu-BTC and CuCo-BTC.[19] However, Cu^{1+} was also detected as a shoulder around 932.7 eV

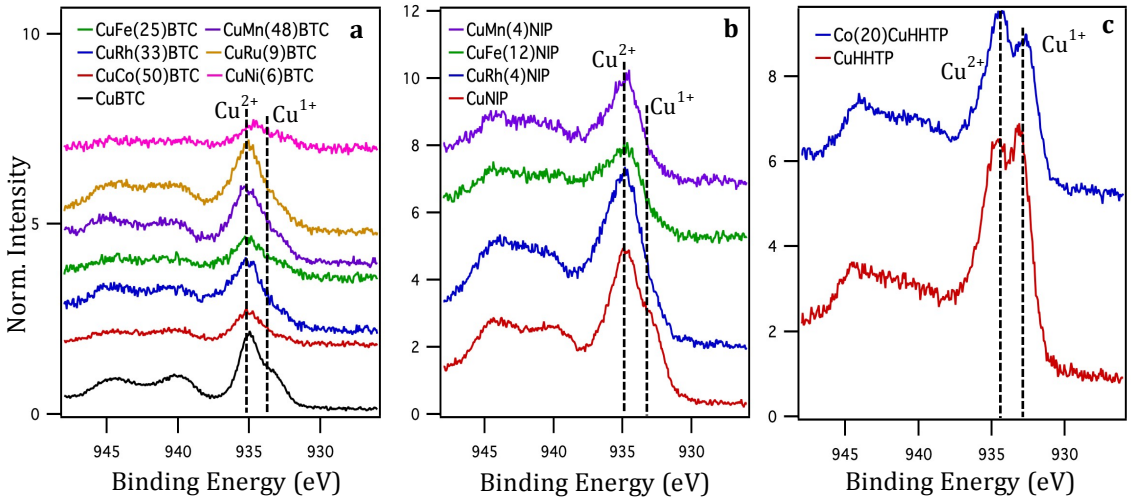

Figure 5.4: XPS Cu(2p) region for Cu-containing a) BTC; b) NIP and c) HHTP MOFs.

for the M_2-(BTC) and M_5-(NIP) MOFs,[27] (Figure 5.4a,b) and as a prominent peak in the M-(HHTP) MOFs (Figure 5.4c). This reduction of Cu^{2+} to Cu^{1+} in Cu-containing MOFs has been previously reported and is attributed to a combination of thermal activation and bombardment by X-rays.[27,35] The satellite features at 940 and 945 eV are characteristic of Cu^{2+}.[36]

The Co(2p) regions for CuCo-BTC, CuCo-HHTP, and Co-HHTP had Co($2p_{3/2}$) binding energies of ~781.3 eV which is consistent with Co^{2+} species[19] (Figure 5.5a). The strong satellite feature appearing 4-5 eV higher in binding energy is attributed to final state effects and core-hole screening associated with charge transfer from the ligand to the 3d orbitals.[37,38] The 16 eV splitting between the Co($2p_{3/2}$) and Co($2p_{1/2}$) peaks is also associated with paramagnetic Co^{2+} as opposed to a 15 eV splitting observed for Co^{3+}.[39,40]

The Mn($2p_{3/2}$) peaks of CuMn-BTC and CuMn-NIP had binding energies of 642.0 and 642.5 eV (Figure 5.5b). Mn^{2+} is the common oxidation state for manganese complexes, and a broad range of binding energies has been reported in the literature for Mn^{2+} ranging from 641.1-642.3 eV.[41–44] The oxidation state of Mn in both MOFs is

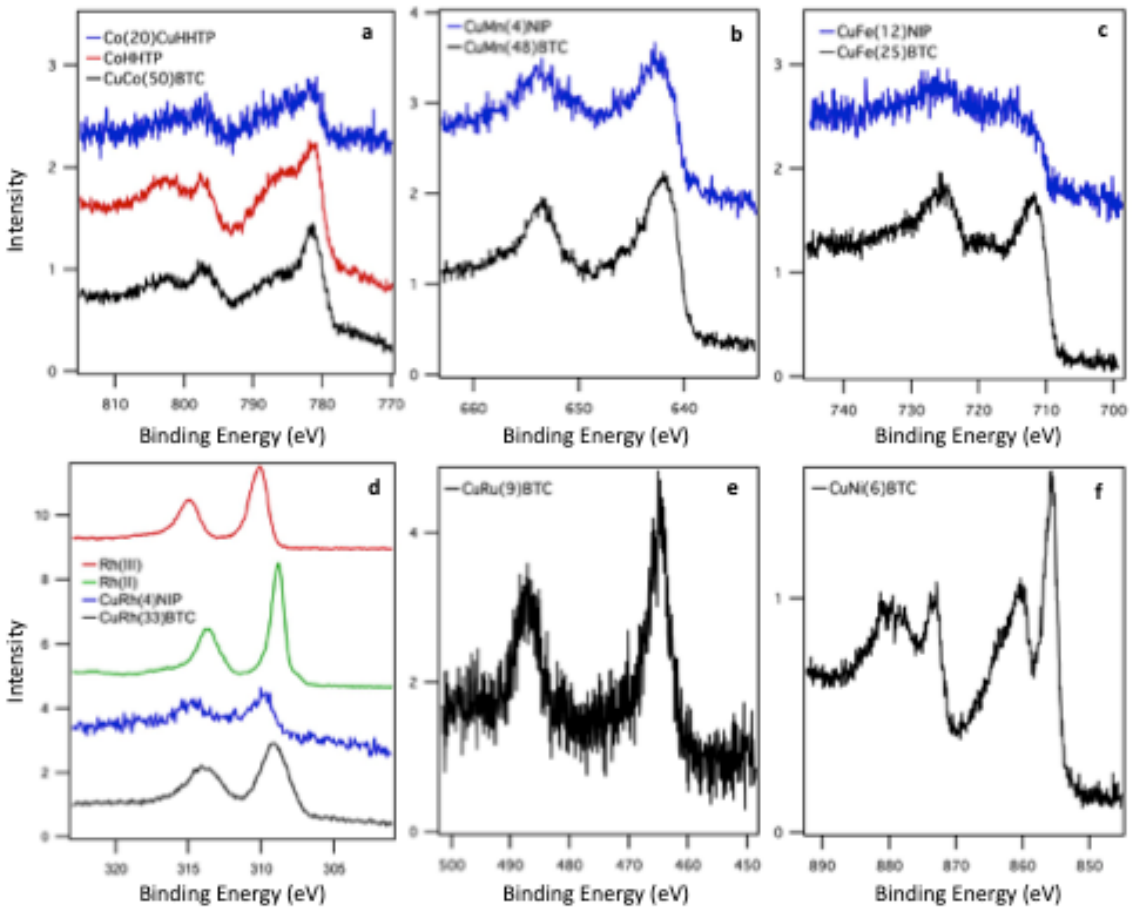

Figure 5.5: XPS metal regions of the MOFs. a) Co(2p); b) Rh(3d); c) Fe(2p); d) Mn(2p); e) Ru(3p); and f) Ni(2p).

assigned to the +2 oxidation state, though it is noted that the Mn($2p_{3/2}$) peak in the M_5-(NIP) sample is ~0.5 eV higher in binding energy than that of Mn in the M_2-(BTC) sample. This is believed to be a result of the differences in binding environment between the pentameric M_5-(NIP) structure and the dimeric M_2-(BTC) structure of the metal nodes.

XPS data of the Fe(2p) regions for CuFe-BTC and CuFe-NIP displayed binding energies for Fe($2p_{3/2}$) at 711.8 eV and 712.4 eV, respectively (Figure 5.5c). Though reports in the literature cite the binding energy of Fe_2O_3 around 710.9 eV,[45,46] and FeOOH species in the range of 711.3-711.8 eV,[47,48] it is difficult to definitively assign the

oxidation state of Fe in the MOF as +2 or +3 without a similar ligand environment to compare to. The low signal from CuFe-NIP makes identification of the peak center difficult, and the satellite features that appear at 730.9 and 719.9 eV in CuFe-BTC can be associated with either Fe^{2+} or Fe^{3+} oxidation states. Therefore no conclusive assignment can be given based on the XPS data alone. Though as was seen for Mn, Fe in the M_5-(NIP) MOF had a binding energy ~0.5 eV higher than that of Fe in the M_2-(BTC) MOF. This is similarly attributed to differences in binding environment between the two different nodes.

The Rh($3d_{5/2}$) peaks of CuRh-BTC and CuRh-NIP had binding energies of 309.2 eV and 309.7 eV (Figure 5.5d). Dirhodium(II) tetraacetate ($Rh_2(OAC)_4$) was used as a standard to provide the oxidation state of Rh^{2+}, which appears at 308.9 eV for ($Rh_2(OAC)_4$). This value was similar to the value observed for CuRh-BTC. In contrast, Rh^{3+} in $RhCl_3$ appeared at 310.1 eV, which is consistent with Rh^{3+} oxidation states reported in the literature.[49] There was no evidence of Rh^{1+}, which is expected at 308.0-308.4 eV,[49,50] or metallic Rh, which has a binding energy of 307.0-307.4 eV.[48,49] It was again seen here that the binding energy of Rh in the M_5-(NIP) sample appeared ~0.5 eV higher than in the M_2-(BTC) sample; this difference in binding energy is attributed to differences in the binding environment for Rh in the pentameric M_5-(NIP) node compared to the dimeric node of M_2-(BTC)

The Ru(3p) region was collected for CuRu-BTC in addition to the Ru(3d) region (which has the highest photoionization cross section) because there was peak overlap between the Ru($3d_{3/2}$) and C(1s) peaks. As shown in Figure 5.5e, the Ru($3p_{3/2}$) peak appeared at 465.1 eV. This value is higher than reported binding energies for Ru^{2+}

(461.0-461.6 eV);[51,52] and Ru^{3+} species have a wide range of expected binding energies from 463.5-465.0 eV).[51–53] However, given the overlap of the Ru(3d) region with C(1s) and the limited information provided by the Ru($3p_{3/2}$) peak, no definitive oxidation assignment can be made for Ru in the CuRu-BTC sample from our XPS data alone.

The Ni($2p_{3/2}$) peak for CuNi-BTC appeared at a binding energy of 855.7 eV (Figure 5.5f). This is near the value expect for Ni^{2+} species reported in the literature at ~855.9 eV.[54,55] The spectrum also consisted of two satellite features at 860.3 and 879.5 eV associated with the presence of Ni^{2+}.[55]

Conductivity Measurements

For further elucidation of the electronic properties of the bimetallic MOFs, conductivity measurements were performed. Prior to measurement, the samples were activated and stored in closed vials, however these vials had not been evacuated of air. Analysis of the prepared M_2-(BTC) systems exhibited an increase in conductivity for the bimetallic MOFs in the order of: CuRu(9)-BTC ($4.98x10^{-10}$ S/cm), CuRh(33)-BTC (6.99×10^{-10} S/cm), CuFe(25)-BTC (6.71×10^{-9} S/cm), and CuMn(48)-BTC (1.34×10^{-8} S/cm); with CuMn and CuFe nodes demonstrating the greatest conductivity. The observed trend in conductivity was contradictive of the results observed by XPS, since the valence band data indicated that the CuRh-BTC sample possessed the greatest DOS near the Fermi level. Interestingly, the main difference between the conductivity measurements and XPS measurements was the sample treatment. For the conductivity measurements, the activated MOF samples were analyzed after a relatively long exposure time to air. While for the XPS measurements, the samples were activated immediately prior to analysis, and transferred to the UHV chamber in air-evacuated vials. To more

accurately compare the conductivity of the samples with their XPS results, the conductivity measurements of two MOFs were repeated using similar sample treatment to that used for XPS. CuFe(25)-BTC and CuRh(33)-BTC were activated and then stored in evacuated ampules prior to their conductivity measurements; the measurements were then performed inside a glove box. As a result, the conductivity of CuRh-BTC revealed to be two orders of magnitude greater than the conductivity of CuFe-BTC, which is in line with the valence band data. Therefore, it was observed that the sample activation or presence of unsaturated metal sites could have a significant effect on the electronic properties of the material.

The monometallic M-(HHTP) MOFs are known to possess relatively high intrinsic conductivity properties.[34] From measuring their conductivity, the value for Cu-HHTP ($3.58x10^{-4}$ S/cm) was found to be greater in comparison to the value for Co-HHTP ($2.55x10^{-5}$ S/cm), which could be partially attributed to the differences in their framework packing. The conductivity value for the bimetallic Co(20)Cu-HHTP MOF was found to be $4.24x10^{-5}$ S/cm, falling between the values of the monometallic MOFs. The result that all M-(HHTP) systems were found to be semiconducting is in agreement with the valence band analysis that exhibited DOS near the Fermi level for each M-(HHTP) MOF.

5.4 Conclusions

The characterization and evaluation of electronic properties were performed for monometallic and bimetallic MOFs. These MOFs were systematically studied by using three different unique SBUs (M_2-(BTC), M_5-(NIP), and M-(HHTP)), and synthesizing bimetallic nodes through metal incorporation of Co, Rh, Fe, Mn, Ru, and Ni in Cu-containing MOFs. Raman spectroscopy was consistent with theoretical calculations in

assigning specific vibrations to those only observed with Cu-Co nodes and not seen with Cu-Cu nodes. This suggests the presence of individual nodes possessing bimetallic nature in the CuCo-BTC system. XPS demonstrated to be a functional tool for determining the relative conductivity of different MOFs by analyzing the density of states near the Fermi level. For the M_2-(BTC) systems, CuCo-BTC and CuRh-BTC demonstrated intensity near E_F, whereas Cu-BTC had no intensity within 1.5 eV of E_F. The monometallic and bimetallic M-(HHTP) systems had similar valence band edges to each other near the Fermi level, closer than that of Cu-BTC. This indicates that the ligand and structure of the MOF plays a significant role in determining the density of states near E_F. The valence band results were supported by conductivity measurements that proved to be dependent on the sample treatment and presence of unsaturated metal sites. CuRh-BTC had the greatest conductivity value among the M_2-(BTC) MOFs, and all of the M-(HHTP) MOFs had a high level of conductivity. Such parameters as SBU geometry, metal node composition, and sample treatment were elucidated for affecting the electronic properties of the MOFs.. Through this work, the aim of understanding the influences on MOF electronic properties can be carried forward in the pursuit of designing functional MOF materials with desirable properties.

Acknowledgments

Thank you to Dr. Natalia Shustova and the members of her group: Otega Ejegbavwo, Corey Martin, and Dr. Ekaterina Dolgopolova for their collaboration in MOF synthesis, PXRD, conductivity measurements, and data analysis. Thank you also to Dr. Vitaly Rassolov, for the theoretical calculations, and collaborator Dr. Vitalie Stavila from Sandia National Lab for additional conductivity measurements. This work acknowledges

funding from the U.S. Department of Energy, Office of Science, Office of Basic Energy Sciences, under Award DE-SC0019360. This work also acknowledges funding from the Donors of the American Chemical Society Petroleum Research Fund, USC's Advanced Support for Innovative Research Excellence (ASPIRE II), and NSF IGERT grant (DGE-1250052).

5.5 References

(1) Chang, K. E.; Kim, C.; Yoo, T. J.; Kwon, M. G.; Heo, S.; Kim, S. Y.; Hyun, Y.; Yoo, J. Il; Ko, H. C.; Lee, B. H. High-Responsivity Near-Infrared Photodetector Using Gate-Modulated Graphene/Germanium Schottky Junction. *Adv. Electron. Mater.* **2019**, *5*, 1800957.

(2) Ji, Y.; Wang, Y.; Yang, Y. Photovoltaic–Pyroelectric–Piezoelectric Coupled Effect Induced Electricity for Self-Powered Coupled Sensing. *Adv. Electron. Mater.* **2019**, *5*, 1900195.

(3) Zhang, X.; Grajal, J.; Luis Vazquez-Roy, J.; Radhakrishna, U.; Wang, X.; Chern, W.; Zhou, L.; Lin, Y.; Shen, P.-C.; Ji, X.; et al. Two-Dimensional MoS_2-Enabled Flexible Rectenna for Wi-Fi-Band Wireless Energy Harvesting. *Nature* **2019**, *566*, 368.

(4) Kumar, L.; Reddy, B. V. R. A Greener Energy Perspective for Smart Devices. In *Proceedings of International Conference on Sustainable Computing in Science, Technology and Management (SUSCOM)*; p. Amity University Rajasthan, Jaipur-India.

(5) Zhang, S.; Nguyen, N.; Leonhardt, B.; Jolowsky, C.; Hao, A.; Park, J. G.; Liang, R. Carbon-Nanotube-Based Electrical Conductors: Fabrication, Optimization, and Applications. *Adv. Electron. Mater.* **2019**, *5*, 1800811.

(6) Bolat, S.; Fuchs, P.; Knobelspies, S.; Temel, O.; Sevilla, G. T.; Gilshtein, E.; Andres, C.; Shorubalko, I.; Liu, Y.; Tröster, G.; et al. Inkjet-Printed and Deep-UV-Annealed $YAlO_x$ Dielectrics for High-Performance IGZO Thin-Film Transistors on Flexible Substrates. *Adv. Electron. Mater.* **2019**, *5*, 1800843.

(7) Vendrell, X.; Yadav, D.; Raj, R.; West, A. R. Influence of Flash Sintering on the Ionic Conductivity of 8 Mol% Yttria Stabilized Zirconia. *J. Eur. Ceram. Soc.* **2019**, *39*, 1352–1358.

(8) Kung, C.-W.; Platero-Prats, A. E.; Drout, R. J.; Kang, J.; Wang, T. C.; Audu, C. O.; Hersam, M. C.; Chapman, K. W.; Farha, O. K.; Hupp, J. T. Inorganic "Conductive Glass" Approach to Rendering Mesoporous Metal−Organic Frameworks Electronically Conductive and Chemically Responsive. *ACS Appl. Mater. Interfaces* **2018**, *10*, 30532.

(9) Lustig, W. P.; Li, J. Luminescent Metal–Organic Frameworks and Coordination Polymers as Alternative Phosphors for Energy Efficient Lighting Devices. *Coord. Chem. Rev.* **2018**, *373*, 116–147.

(10) Stavila, V.; Talin, A. A.; Allendorf, M. D. MOF-Based Electronic and Optoelectronic Devices. *Chem. Soc. Rev.* **2014**, *43*, 5994–6010.

(11) Stassen, I.; Burtch, N.; Talin, A.; Falcaro, P.; Allendorf, M.; Ameloot, R. An Updated Roadmap for the Integration of Metal-Organic Frameworks with

Electronic Devices and Chemical Sensors. *Chem. Soc. Rev.* **2017**, *46*, 3185–3241.

(12) Yeon Lee, D.; Kim, E.-K.; Shrestha, N. K.; Boukhvalov, D. W.; Kee Lee, J.; Han, S.-H. Charge Transfer-Induced Molecular Hole Doping into Thin Film of Metal−Organic Frameworks. *ACS Appl. Mater. Interfaces* **2015**, *7*, 18501–18507.

(13) Rana, S.; Rajendra, R.; Dhara, B.; Jha, P. K.; Ballav, N. Highly Hydrophobic and Chemically Rectifiable Surface-Anchored Metal-Organic Framework Thin-Film Devices. *Adv. Mater. Interfaces* **2016**, *3*, 1–8.

(14) Yeon Lee, D.; Shinde, D. V; Joon Yoon, S.; Nam Cho, K.; Lee, W.; Shrestha, N. K.; Han, S.-H. Cu-Based Metal−Organic Frameworks for Photovoltaic Application. *J. Phys. Chem. C* **2014**, *118*, 16328.

(15) Draga¨sser, A.; Shekhah, O.; Zybaylo, O.; Shen, C.; Buck, M.; Woïl, C.; Schlettwein, D. Redox Mediation Enabled by Immobilised Centres in the Pores of a Metal-Organic Framework Grown by Liquid Phase Epitaxy. *Chem. Commun* **2012**, *48*, 663–665.

(16) Sun, L.; Hendon, C. H.; Minier, M. A.; Walsh, A.; Dincă, M. Million-Fold Electrical Conductivity Enhancement in Fe_2(DEBDC) versus Mn_2 (DEBDC) (E = S, O). *J. Am. Chem. Soc.* **2015**, *137*, 6164–6167.

(17) Johnson, B. A.; Bhunia, A.; Fei, H.; Cohen, S. M.; Ott, S. Development of a UiO-Type Thin Film Electrocatalysis Platform with Redox-Active Linkers. *J. Am. Chem. Soc.* **2018**, *140*, 2985–2994.

(18) Xie, L. S.; Sun, L.; Wan, R.; Park, S. S.; Degayner, J. A.; Hendon, C. H.; Dincă, M. Tunable Mixed-Valence Doping toward Record Electrical Conductivity in a Three-Dimensional Metal−Organic Framework. *J. Am. Chem. Soc.* **2018**, *140*, 7411–7414.

(19) Dolgopolova, E. A.; Brandt, A. J.; Ejegbavwo, O. A.; Duke, A. S.; Maddumapatabandi, T. D.; Galhenage, R. P.; Larson, B. W.; Reid, O. G.; Ammal, S. C.; Heyden, A.; et al. Electronic Properties of Bimetallic Metal-Organic Frameworks (MOFs): Tailoring Density of Electronic States Through MOF Modularity. *J. Am. Chem. Soc.* **2017**, *139*, 5201–5209.

(20) Kim, D.; Song, K. S.; Buyukcakir, O.; Yildirim, T.; Coskun, A. Bimetallic Metal Organic Frameworks with Precisely Positioned Metal Centers for Efficient H_2 Storage. *Chem. Commun* **2018**, *54*, 12218.

(21) Song, X.; Oh, M.; Lah, M. S. Hybrid Bimetallic Metal−Organic Frameworks: Modulation of the Framework Stability and Ultralarge CO 2 Uptake Capacity. *Inorg. Chem.* **2013**, *52*, 10869–10876.

(22) Su, Y.; Yu, J.; Li, Y.; Fiona, S.; Phua, Z.; Liu, G.; Lim, W. Q.; Yang, X.; Ganguly, R.; Dang, C.; et al. Versatile Bimetallic Lanthanide Metal-Organic Frameworks for Tunable Emission and Efficient Fluorescence Sensing. *Commun. Chem.* **2018**, *1*,

12.

(23) Chen, C.; Wu, M.-K.; Tao, K.; Zhou, J.-J.; Li, Y.-L.; Han, X.; Han, L. Formation of Bimetallic Metal–Organic Framework Nanosheets and Their Derived Porous Nickel–Cobalt Sulfides for Supercapacitors. *Dalt. Trans.* **2018**, *47*, 5639–5645.

(24) Stock, N.; Biswas, S. Synthesis of Metal-Organic Frameworks (MOFs): Routes to Various MOF Topologies, Morphologies, and Composites. *Chem. Rev.* **2012**, *112*, 933–969.

(25) Yuan, S.; Feng, L.; Wang, K.; Pang, J.; Bosch, M.; Lollar, C.; Sun, Y.; Qin, J.; Yang, X.; Zhang, P.; et al. Stable Metal–Organic Frameworks: Design, Synthesis, and Applications. *Adv. Mater.* **2018**, *30*, 1–35.

(26) Kirchon, A.; Feng, L.; Drake, H. F.; Joseph, E. A.; Zhou, H.-C. From Fundamentals to Applications: A Toolbox for Robust and Multifunctional MOF Materials. *Chem. Soc. Rev* **2018**, *47*, 8611.

(27) Duke, A. S.; Dolgopolova, E. A.; Galhenage, R. P.; Ammal, S. C.; Heyden, A.; Smith, M. D.; Chen, D. A.; Shustova, N. B. Active Sites in Copper-Based Metal-Organic Frameworks: Understanding Substrate Dynamics, Redox Processes, and Valence-Band Structure. *J. Phys. Chem. C* **2015**, *119*, 27457–27466.

(28) Dolgopolova, E. A.; Galitskiy, V. A.; Martin, C. R.; Gregory, H. N.; Yarbrough, B. J.; Rice, A. M.; Berseneva, A. A.; Ejegbavwo, O. A.; Stephenson, K. S.; Kittikhunnatham, P.; et al. Connecting Wires: Photoinduced Electronic Structure Modulation in Metal−Organic Frameworks. *J. Am. Chem. Soc* **2019**, *141*, 5350–5358.

(29) Dhumal, N. R.; Singh, M. P.; Anderson, J. A.; Kiefer, J.; Kim, H. J. Molecular Interactions of a Cu-Based Metal-Organic Framework with a Confined Imidazolium-Based Ionic Liquid: A Combined Density Functional Theory and Experimental Vibrational Spectroscopy Study. *J. Phys. Chem. C* **2016**, *120*, 3295–3304.

(30) Todaro, M.; Alessi, A.; Sciortino, L.; Agnello, S.; Cannas, M.; Gelardi, F. M.; Buscarino, G. Investigation by Raman Spectroscopy of the Decomposition Process of HKUST-1 upon Exposure to Air. *J. Spectrosc.* **2016**, *2016*, 1–7.

(31) Sun, H.; Han, X.; Liu, K.; Shen, B.; Liu, J.; Wu, D.; Shi, X. Metal-Modified Cu-BTC Acid for Highly Enhanced Adsorption of Organosulfur Species. *Ind. Eng. Chem. Res.* **2017**, *56*, 9541–9550.

(32) Ko, M.; Aykanat, A.; Smith, M. K.; Mirica, K. A.; Ko, M.; Aykanat, A.; Smith, M. K.; Mirica, K. A. Drawing Sensors with Ball-Milled Blends of Metal-Organic Frameworks and Graphite. *Sensors* **2017**, *17*, 2192.

(33) Darago, L. E.; Aubrey, M. L.; Yu, C. J.; Gonzalez, M. I.; Long, J. R. Electronic Conductivity, Ferrimagnetic Ordering, and Reductive Insertion Mediated by

Organic Mixed-Valence in a Ferric Semiquinoid Metal-Organic Framework. *J. Am. Chem. Soc.* **2015**, *137*, 15703–15711.

(34) Mendecki, L.; Mirica, K. A. Conductive Metal-Organic Frameworks as Ion-to-Electron Transducers in Potentiometric Sensors. *ACS Appl. Mater. Interfaces* **2018**, *10*, 19248–19257.

(35) Szanyi, J.; Daturi, M.; Clet, G.; Baer, D. R.; Peden, C. H. F. Well-Studied Cu-BTC Still Serves Surprises: Evidence for Facile Cu2+/Cu+ Interchange. *Phys. Chem. Chem. Phys.* **2012**, *14*, 4383–4390.

(36) Ghijsen, J.; Tjeng, L. H.; Vanelp, J.; Eskes, H.; Westerink, J.; Sawatzky, G. A.; Czyzyk, M. T. Electronic-Structure of Cu_2O and CuO. *Phys. Rev. B* **1988**, *38*, 11322–11330.

(37) Vaz, C. A. F.; Prabhakaran, D.; Altman, E. I.; Henrich, V. E. Experimental Study of the Interfacial Cobalt Oxide in Co3O4/Alpha-Al2O3(0001) Epitaxial Films. *Phys. Rev. B* **2009**, *80*, 155457.

(38) Kochubey, D.; Kaichev, V.; Saraev, A.; Tomyn, S.; Belov, A.; Voloshin, Y. Combined X-Ray Absorption Near-Edge Structure and X-Ray Photoelectron Study of the Electrocatalytically Active Cobalt(I) Cage Complexes and the Clathrochelate Cobalt(II)- and Cobalt(III)-Containing Precursors and Analogs. *J. Phys. Chem. C* **2013**, *117*, 2753–2759.

(39) Frost, D. C.; McDowell, C. A.; Woolsey, I. S. Evidence for Multiplet Splitting of 2p Photoelectron Lines of Transition-Metal Complexes. *Chem. Phys. Lett.* **1972**, *17*, 320–323.

(40) Haraguchi, H.; Fujiwara, K.; Keiichiro, F. A Study of Co Complexes by X-Ray Photoelectron Spectroscopy. *Chem. Lett.* **1975**, 409–414.

(41) Chen, J.; Ma, H.-C.; Xin, W.-L.; Li, X.-B.; Jin, F.-Z.; Wang, J.-S.; Liu, M.-Y.; Dong, Y.-B. Dual Heterogeneous Catalyst Pd−Au@Mn(II)-MOF for One-Pot Tandem Synthesis of Imines from Alcohols and Amines. *Inorg. Chem* **2017**, *56*, 660.

(42) Li, H.-T.; Gao, Q.; Han, B.; Ren, Z.-H.; Xia, K.-S.; Zhou, C.-G. Partial-Redox-Promoted Mn Cycling of Mn(II)-Doped Heterogeneous Catalyst for Efficient H_2O<sub2</sub>>-Mediated Oxidation. *ACS Appl. Mater. Interfaces* **2017**, *9*, 371–380.

(43) Lin, J.; Zhang, Q.; Wang, L.; Liu, X.; Yan, W.; Wu, T.; Bu, X.; Feng, P. Atomically Precise Doping of Monomanganese Ion into Coreless Supertetrahedral Chalcogenide Nanocluster Inducing Unusual Red Shift in Mn 2+ Emission. *J. Am. Chem. Soc* **2014**, *136*, 4769–4779.

(44) Thompson, M. J.; Blakeney, K. J.; Cady, S. D.; Reichert, M. D.; Del Pilar-Albaladejo, J.; White, S. T.; Vela, J. Cu 2 ZnSnS 4 Nanorods Doped with

Tetrahedral, High Spin Transition Metal Ions: Mn 2+ , Co 2+ , and Ni 2+. *Chem. Mater* **2016**, *28*, 1668–1677.

(45) Leveneur, J.; Waterhouse, G. I. N.; Kennedy, J.; Metson, J. B.; Mitchell, D. R. G. Nucleation and Growth of Fe Nanoparticles in SiO_2: A TEM, XPS, and Fe L-Edge XANES Investigation. *J. Phys. Chem. C* **2011**, *115*, 20978–20985.

(46) Zhang, G.; Qu, J.; Liu, H.; Liu, R.; Li, G. Removal Mechanism of As(III) by a Novel Fe-Mn Binary Oxide Adsorbent: Oxidation and Sorption. *Environ. Sci. Technol.* **2007**, *41*, 4613–4619.

(47) Niu, S.; Jiang, W.-J.; Wei, Z.; Tang, T.; Ma, J.; Hu, J.-S.; Wan, L.-J. Se-Doping Activates FeOOH for Cost-Effective and Efficient Electrochemical Water Oxidation. *J. Am. Chem. Soc.* **2019**, *141*, 7005–7013.

(48) Wagner, C. D.; Riggs, W. M.; Davis, L. E.; Moulder, J. F. *Handbook of X-Ray Photoelectron Spectroscopy*; Muilenberg, G. E., Ed.; Perkin Elmer Corporation: Eden Prairie, MN, 1979.

(49) Lang, R.; Li, T. B.; Matsumura, D.; Miao, S.; Ren, Y. J.; Cui, Y. T.; Tan, Y.; Qiao, B. T.; Li, L.; Wang, A. Q.; et al. Hydroformylation of Olefins by a Rhodium Single-Atom Catalyst with Activity Comparable to RhCl(PPh3)3. *Angew. Chem. Int. Ed.* **2016**, *55*, 16054–16058.

(50) Zhou, X.-S.; Dong, Z.-R.; Zhang, H.-M.; Yan, J.-W.; Gao, J.-X.; Mao, B.-W. Self-Assembly of a Rh(I) Complex on Au(111) Surfaces and Its Electrocatalytic Activity toward the Hydrogen Evolution Reaction. **2007**.

(51) Varughese, B.; Chellamma, S.; Lieberman, M. XPS Study of Self-Assembly of Ruthenium Dimers $[((Acac)_2Ru)_2Bptz]^{0,+}$ on Hydrophobic and Hydrophilic SAMs. *Langmuir* **2002**, *18*, 7964–7970.

(52) Citrin, P. H.; Ginsberg, A. P. X-Ray Photoemission from the Creutz-Taube Mixed Valence Complex: A Reassessment. *J. Am. Chem. Soc* **1981**, *103*, 3673–3679.

(53) Morgan, D. J. Resolving Ruthenium: XPS Studies of Common Ruthenium Materials. *Surf. Interface Anal.* **2015**, *47*, 1072–1079.

(54) Peng, M. M.; Jeon, U. J.; Ganesh, M.; Aziz, A.; Vinodh, R.; Palanichamy, M.; Jang, H. T. Oxidation of Ethylbenzene Using Nickel Oxide Supported Metal Organic Framework Catalyst. *Bull. Korean Chem. Soc.* **2014**, *35*, 3213–3218.

(55) Cheng, Q.; Tao, K.; Han, X.; Yang, Y.; Yang, Z.; Ma, Q.; Han, L. Ultrathin Ni-MOF Nanosheet Arrays Grown on Polyaniline Decorated Ni Foam as an Advanced Electrode for Asymmetric Supercapacitors with High Energy Density. *Dalt. Trans* **2019**, *48*, 4119–4123.

CHAPTER 6

GROWTH OF CRYSTALLINE, BIMETALLIC METAL-ORGANIC FRAMEWORK FILMS VIA DIP-COATING AND TRANSMETALLATION

6.1 Introduction

The diversity of active metal sites and tunable, porous structures of metal-organic frameworks (MOFs) has elevated MOFs to a high level of interest, extending into several areas of research including catalysis[1–3], gas storage and separation[4–6], energy transfer[7,8], and sensing devices.[9,10] In recent years, the shift to reduce reliance on fossil fuels and move toward harnessing renewable sources for energy has drawn focus on energy efficiency and sustainability while mitigating greenhouse gas emissions. MOFs have emerged as promising materials for electrochemical applications ranging from electrode materials for batteries and supercapacitors, to electrocatalysts for fuel cells and electrolyzers.[11–13] Based on their high surface area, crystalline framework, and intrinsic porosity, MOFs possess ideal characteristics for innovation in these applications. MOFs are comprised of molecular organic linkers and metal-rich nodes[14] that can be assembled from a vast array of metal ions and ligands to form unique structures of various pore sizes and surface areas for enhancing their chemical and physical properties. Typically, MOFs are generated through solvothermal synthesis methods to produce microcrystalline powders. However, this presents a challenge in controlling the geometry and structural uniformity of the material for implementation in electrical applications. The development

of MOFs as thin films has gained much attention for their promise in future electrochemical applications.[12,15–17] MOFs synthesized as films ensures a direct physical interface between the MOF and substrate material. The means by which the MOF film is grown is key to the integrity of its structure and resulting performance. Growth procedures such as solvothermal film synthesis in which the substrate is heated in a solution of mixed precursors,[18–23] or pre-synthesized MOF powder is transferred onto the substrate material through drop-casting[24,25] or electrodeposition[26,27] often lead to polycrystalline films with poor electrochemical communication between the MOF and the underlying substrate. Separating the reactants and alternately immersing the substrate into the metal and organic precursors enables the formation of uniform films with controllable thicknesses. This ideal method also reduces the surface roughness down to the nm scale.[28]

The incorporation of a second metal in the MOF structure has been studied in powder MOFs for potential in improving catalytic, conductive, and gas storage, properties.[29–32] However, the field of bimetallic MOF films has been relatively unexplored. There are reports of bimetallic MOF films created from solvothermal synthesis by heating the substrate in the mixed solution,[19–23] or coating the pre-formed powder MOF onto the substrate in a thin layer,[24,25] but very few studies have reported on bimetallic films grown by the synthesis procedure of alternating the substrate in precursor solutions. Some studies have used a spraying technique for bimetallic film growth, alternating between a Zn metal-oxo cluster and Re[33] or Pd ligands.[34] Studies by Kitagawa et al. employed a dipping procedure for bimetallic MOF films using three components: two separate metal ion solutions and one solution of organic linker.[35–40] The growth of

these bimetallic films, however, were conducted using thiol-based self-assembled monolayers (SAMs) for film nucleation and orientation. Substrate functionalization using SAMs can assist in directing crystal orientation, but there are a number of disadvantages to using SAMs for binding the MOF structure to the support. One example is their poor thermal and chemical stability.[41,42] Another concern of thiol-based SAMs is their insulating nature, hindering electrical contact between the substrate and MOF film.[10]

In this work, the first account of a bimetallic MOF film grown using an alternating-solution dip-coating technique followed by transmetallation for incorporation of a second metal at the MOF nodes is presented. Crystalline films of $Cu_3(BTC)_2$ (BTC = 1,3,5-benzenetricarboxylate) are grown by immersing an alumina/Si(100) substrate in solutions of Cu acetate and organic linker (H_3BTC). The $Cu_3(BTC)_2$ MOF is known to possess favorable qualities of high surface area and thermal stability.[43,44] Co^{2+} ions are exchanged into the MOF framework by immersing the $Cu_3(BTC)_2$ films in solutions of $CoCl_2$. Co has shown to have excellent redox properties and substantial activity for electrocatalysis processes.[45–48] By varying the temperature and immersion time, different concentrations of Co are incorporated into the films, as determined by X-ray photoelectron spectroscopy (XPS) experiments. Atomic force microscopy (AFM) measurements show that the substrate is uniformly covered by the MOF film after transmetallation, and GIWAXS indicates that the bimetallic films retain their crystallinity. Stability studies of the films submerged in dimethylformamide (DMF) indicate the coverage remains uniform with crystallites covering the surface, however some rearrangement does occur as the crystallite sizes increase over time. Here, the morphology, composition, and crystallinity of bimetallic copper-cobalt BTC-containing

MOF films are characterized. Because of the controllable means of incorporating a second metal into the framework, and the stability of the film in maintaining a crystalline structure after transmetallation, this synthesis method provides a novel approach for achieving bimetallic MOF films for potential in electrical applications and device integration.

6.2 Experimental

Materials

$Cu(CH_3COO)_2 \cdot H_2O$ ($Cu(OAc)_2$, >95%, TCI America), 1,3,5-benzenetricarboxylic acid (H_3BTC, 98%, Alfa Aesar), $CoCl_2 \cdot 6H_2O$ (>98.0%, TCI America), ethanol (200 proof, Decon Laboratories), *N,N′*-dimethylformamide (DMF, ACS grade, BDH), tetrachloroethylene (99.9%, BDH), acetone (≥99.5%, Sigma-Aldrich), and methanol (≥99.8%, Sigma-Aldrich) were used as received.

Film Synthesis

Thin films of Cu_3BTC_2 were grown on a sputter-deposited 2.5 nm film of Al_2O_3 on a polished, p-type Si(100) substrate (University Wafer). The wafer substrates were cut into approximate 1.0 x 1.2 cm size rectangles and thoroughly cleaned by sonication in tetrachloroethylene, acetone, and methanol, separately, for 20 minutes each. The precursors for growing the Cu_3BTC_2 films consisted of 1mM $Cu(OAc)_2$ in ethanol and 1mM H_3BTC in ethanol. One cycle of thin film synthesis is conducted by sequential submersion of the substrate into the $Cu(OAc)_2$ solution for 1 minute followed by 15 seconds of rinsing in ethanol and 15 seconds of drying under a flow of N_2. The substrate is then submerged in H_3BTC solution for 1 minute followed again by 15 seconds of

rinsing in ethanol and 15 seconds of drying under N_2. Forty cycles were used for the synthesis of each Cu_3BTC_2 film.

Film Transmetallation

Monometallic Cu_3BTC_2 films are transformed into bimetallic copper-cobalt BTC films ($Cu_3Co_{3-x}(BTC)_2$) through transmetallation utilizing a $CoCl_2$ solution in DMF (10 mL, 1.05 g Co_2Cl) or ethanol (10 mL, 0.33 g Co_2Cl). Cu_3BTC_2 films are placed in the $CoCl_2$ solution for a specified exchange temperature and time. The length of time and temperature of transmetallation dictate the amount of cobalt that exchanges with copper in the film. After the metal exchange, the new bimetallic film is placed either in fresh DMF or ethanol to remove excess cobalt chloride and ensure the cobalt that remains is incorporated within the MOF framework. The DMF solvent is replaced twice a day over a 72 hour time period and the ethanol solvent is replaced 3 times in a 15 minute time period.

Characterization

X-ray Photoelectron Spectroscopy (XPS) measurements were collected using a Kratos AXIS Ultra DLD system with a monochromatic Al K_α source, hemispherical analyzer and charge neutralizer; this vacuum system has been described previously.[49] The base pressure of the vacuum chamber is 1 x 10^{-9} Torr before sample introduction and $\leq$ 3 x 10^{-9} Torr during experiments. The dwell time for all regions is 1000 ms and the energy step size is 0.06 eV. Survey scans were collected for all films to ensure that there were no contaminants introduced during sample preparation. Absolute binding energies were determined by setting the position of the lower energy adventitious carbon peak to 284.8 eV.

Grazing Incidence Wide Angle X-ray Scattering (GIWAXS) measurements were collected on a SAXSLab Ganesha at the South Carolina SAXS Collaborative. A Xenocs GeniX3D microfocus source with a Cu target and a Hybrid Pixel Array Pilatus detector (Dectris) was used for collecting scattering patterns. Measurements of films were conducted at an incident angle of 4˚ at room temperature for 30 minutes.

Tapping mode Atomic Force Microscopy (AFM) experiments were carried out using a Multimode Nanoscope IIIA system (Digital Instruments Inc.) to study the surface morphology of different MOF thin films prepared on the commercial Al_2O_3/Si substrate. AFM imaging was performed in air using commercial Si cantilevers with nominal spring constants of 25-75 N/m and resonance frequencies of 200-400 kHz (ACT, Applied NanoStructures). All AFM images were obtained using Nanoscope V530R software with scan rate of 1Hz.

Film thicknesses were measured with a field emission scanning electron microscope (Zeiss Gemini Ultraplus). The edge of the MOF film was coated with gold (200 Å) to prevent charging effects.

6.3 Results and Discussion

GIWAXS data for the CuBTC films grown by dip-coating indicate that the film is crystalline (Figure 6.1) and has the same structure as CuBTC powders reported in the literature.[44,50] A simulated spectrum for CuBTC is shown in the top panel of Figure 6.1 along with the assignment of the prominent peaks at the lower scattering angles. The CoCuBTC films prepared by exchanging the Cu^{2+} with Co^{2+} ions at different temperatures and times (13-56%, Figure 6.1b-e) also exhibit the same GIWAXS spectrum as the CuBTC film, indicating that the crystallinity of the film is retained after

incorporation of Co into the MOF structure. However, crystallinity of the pure CoBTC film was lost when 100% of the Cu^{2+} ions were exchanged for Co^{2+} (Figure 6.1f), and

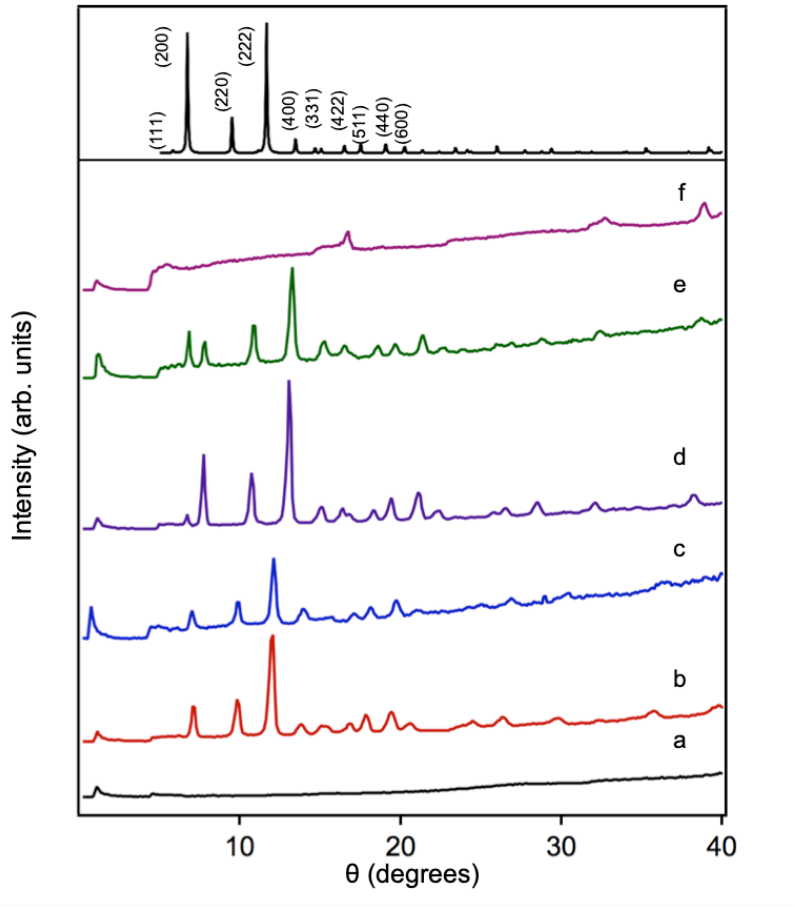

Figure 6.1: GIWAXS data for: a) the Al_2O_3/Si substrate; b) CuBTC film; c) CoCuBTC film (56% Co, exchanged at 90 °C for 15 min); d) CoCuBTC film (20% Co, exchanged at 50 °C for 60 min); e) CoCuBTC film (13% Co, exchanged at 25 °C for 24 hr in ethanol); f) CoBTC film (100% Co, exchanged at 90 °C for 8 hr). As a reference, the top panel shows the simulated spectrum for CuBTC.

this suggests that some fraction of Cu^{2+} is necessary to provide stability to the structure. In general, the CoCuBTC films were found to be crystalline for Co concentrations ranging from 7% to 94%. Although the (111) facet is only a minor peak in both the simulated spectrum and in the spectrum of CuBTC, this peak is more pronounced in the spectra of the 13% and 20% Co films. It should be noted that the (111) facet is also

observed in the literature for CuBTC powders and appears to be sensitive to the exact growth conditions.[44,51]

Table 6.1: Conditions for transmetallation of the CuBTC films by exposure to $CoCl_2$.

% Co	Exchange time (hrs)	Temperature (°C)	Solvent
7	1	25	DMF
20	1	50	DMF
35	24	25	DMF
56	0.25	90	DMF
63	1	90	DMF
94	6	90	DMF
100	8	90	DMF
9	3	25	Ethanol
13	24	25	Ethanol
40	0.50	70	Ethanol

The compositions of the films and metal oxidation states were investigated by XPS (Figure 6.2). Specifically, the relative Co:Cu compositions were established from the integrated Co($2p_{3/2}$) and Cu($2p_{3/2}$) peaks after correcting for atomic sensitivities. The results are displayed in Table 6.1, showing that longer exchange times and temperatures during transmetallation resulted in higher Co concentrations. The Al_2O_3/Si substrate itself had no features in the Co(2p) and Cu(2p) regions, and the CuBTC film did not exhibit features in the Co(2p) region (Figure 6.2a,b). For the 35%, 56% and 63% CoCuBTC films, the Co($2p_{3/2}$) peak appeared at 781.8 eV, which is the same as the binding energy attributed to Co^{2+} for CoCuBTC MOF powders.[32] The pronounced shoulder at 4-5 eV higher binding energy is ascribed to final state effects and core-hole screening associated with charge transfer from the ligand to the 3d orbitals;[52,53] this satellite feature is associated with paramagnetic Co^{2+}, which is also consistent with the 16 eV splitting between the Co($2p_{3/2}$) and Co($2p_{1/2}$) peaks as opposed to a splitting of 15 eV observed for

diamagnetic Co^{3+}.[54,55] In the Cu(2p) region (Figure 6.2b), the CuBTC film has a peak at 935.2 eV assigned to Cu^{2+} and a shoulder at 933.5 eV assigned to Cu^{1+}.[49,56,57] A

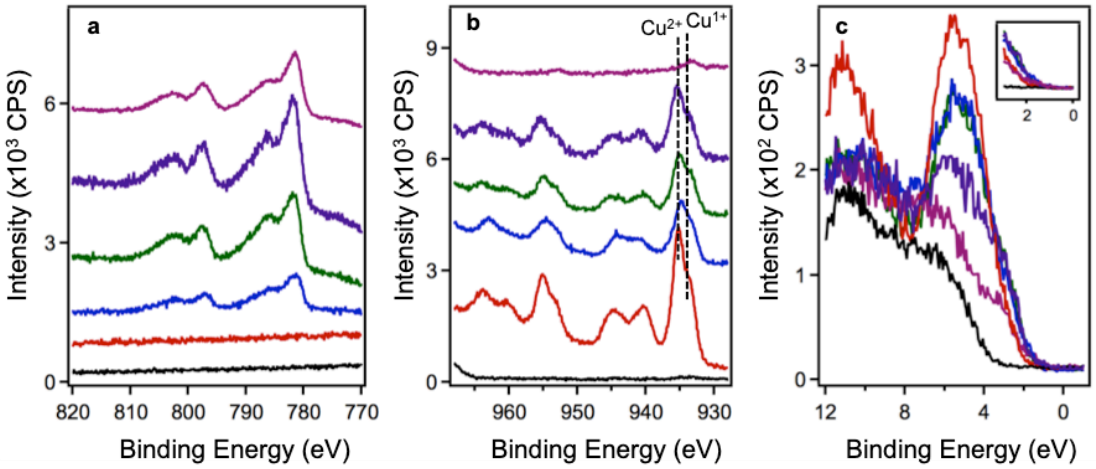

Figure 6.2: XPS data for: a) Co(2p); b) Cu(2p); and c) valence band regions. Surfaces shown are: the Al_2O_3/Si substrate (black); CuBTC film (red); CoCuBTC film (35% Co, blue); CoCuBTC film (56% Co, green); CoCuBTC film (63% Co, purple); and CoCuBTC film (94% Co, pink).

combination of removal of the coordinating solvent and water in vacuum and irradiation by X-rays is known to induce reduction of Cu^{2+} to Cu^{1+} in CuBTC.[49,58–60] Furthermore, the pronounced satellite features at 940.2 and 944.9 eV are also characteristic of Cu^{2+} and not observed for Cu^{1+}.[61] Given that the Cu($2p_{3/2}$) binding energies are nearly identical for Cu^0 and Cu^{1+},[61,62] the Cu(LMM) Auger region was also collected (Figure 6.3a) to confirm that metallic Cu was not present; the Cu(LMM) spectrum exhibits a much broader feature at 572 eV for Cu^{1+} in contrast to a sharp peak at 568 eV for Cu^0.[49] For the CoCuBTC films containing 35-63% Co, the main features of the Cu(2p) region are the same as for CuBTC although the intensities decrease due to the decrease in Cu concentration. For the CoCuBTC film with only 6% Cu, the main peak appears to be Cu^{1+}. Valence band spectra (Figure 6.2c) show that incorporation of Co into the MOF results in a shift in the valence band edge to lower binding energies. While the insulating

Al_2O_3/Si substrate has almost no intensity above 4 eV, the CuBTC film has a peak in the valence band region at 5.25 eV as well as intensity that extends to ~2 eV. The valence

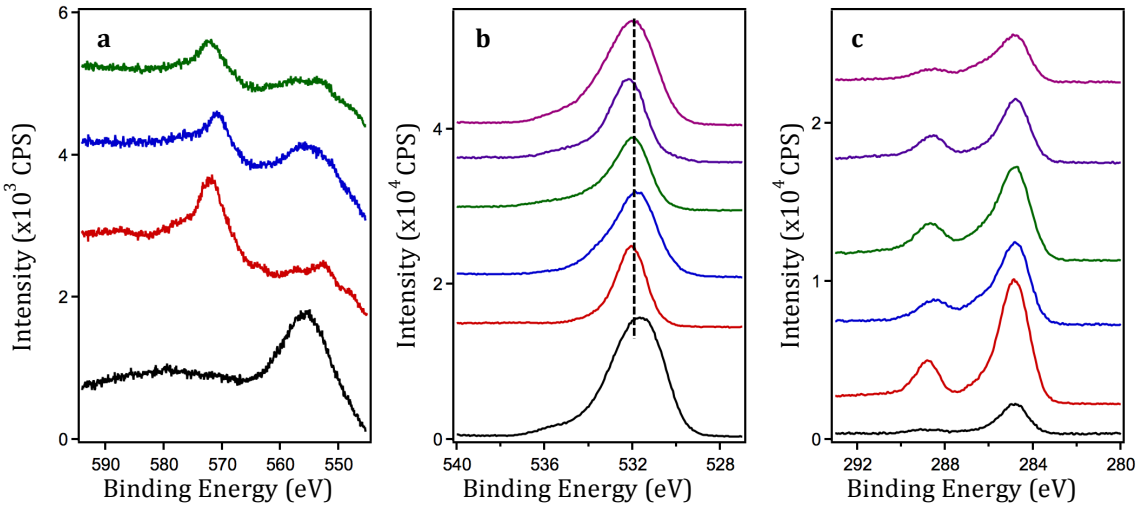

Figure 6.3: XPS data for: a) Cu(KLL) Auger; b) O(1s); and c) C(1s) regions. Surfaces shown are: the Al_2O_3/Si substrate (black); CuBTC film (red); CoCuBTC film (35% Co, blue); CoCuBTC film (56% Co, green); CoCuBTC film (63% Co, purple); and CoCuBTC film (94% Co, pink).

band spectra for the CoCuBTC films (35-63% Co) are similar to that of CuBTC except that the valence band edge extends slightly more towards the Fermi level for the bimetallic films. For example, the onset of rise of the valence band edge occurs ~0.7 eV lower in energy for the 63% Co film compared to CuBTC. The 94% Co film has a peak shape that resembles that of the substrate except at the lowest binding energies, where a higher intensity tail exists; this behavior is attributed to the fact that the 94% Co film has some regions of exposed substrate. Previous studies of CoCuBTC MOF powders have shown that the valence band edge shifts significantly toward the Fermi level compared to the position for the CuBTC valence band edge, indicating that there is density of states near the Fermi level, as typically observed for a semiconductor.[63] However, for the

CoCuBTC films differences in the valence band edge compared to CuBTC are not as pronounced, and intensity does not appear at the Fermi level.

The O(1s) and C(1s) spectra for the MOF films are consistent with what has been reported for the MOF powders (Figure 6.3b,c).[58,64] The higher binding energy C(1s) peak at 288.8 eV is attributed to C=O while the 284.8 eV is assigned to a combination of adventitious carbon and aliphatic carbons. For both MOF films and powders, the ratio of the 288.8 eV to 284.8 eV peaks is 0.32 ± 0.04. However, in the cases where the MOF films are partially delaminated, the ratio decreases, and therefore this ratio is used as an indicator of delamination. The 94% Co film is believed to be partially delaminated given that this ratio is 0.26. Furthermore, the Al(2s) and Si(2p) signals from the substrate are visible whereas these signals are almost completely attenuated for the CuBTC films. The shape of the O(1s) peak is also indicative of exposed Al_2O_3 regions, given that oxygen species in the MOFs have a narrower O(1s) peak and oxygen in alumina is shifted to lower binding energy by 0.4 eV. In general, delamination of the films is characterized by more prominent Si(2p) and Al(2s) peaks from the substrate, as well as a decrease in MOF:adventitious carbon ratio and a broadening and shift to lower binding energy for the O(1s) peak. However, the GIWAXS data for the partially delaminated films indicate that they are still crystalline.

As shown in Table 6.1, various Co concentrations can be achieved by varying the exchange time and temperature, with higher temperatures and longer times leading to greater Co compositions. However, the extent of Co incorporation appears to be sensitive to defects in the original CuBTC film. For example, when the film is not uniformly dried with N_2 between dip-coating cycles, visual defects may appear that reflect how the excess

solvent was dried on the surface. These films with visual defects incorporate a higher percentage of Co ions under the same exchange conditions compared with the films that were dried uniformly.

AFM experiments were conducted to characterize the morphology of the CuBTC film (Figure 6.4a). After 40 cycles of immersion in the Cu acetate solution followed by immersion in the solution of BTC ligand, the resulting surface appeared to be covered by crystallites with lateral dimensions ranging from 200-400 nm and heights of 60-150 nm. The root mean squared (RMS) roughness was ~25 nm. After the film is exchanged in

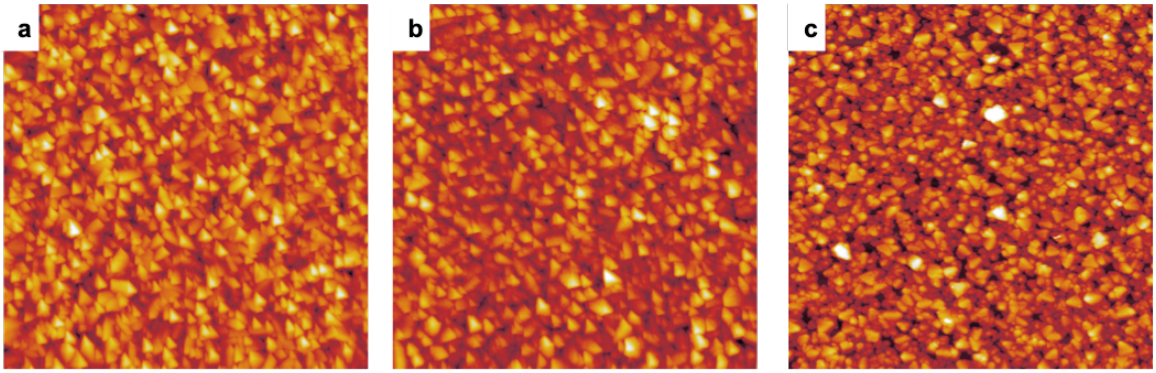

Figure 6.4: AFM images of: a) CuBTC film; b) CoCuBTC film (56% Co, exchanged at 90 °C for 15 min); and c) CoCuBTC film (63% Co, exchanged at 90 °C for 60 min). All images are 5 μm x 5 μm.

$CoCl_2$ for 15 min at 90 °C to produce a 56% Co concentration, the overall morphology of the film is unchanged and the RMS roughness remains 25 nm (Figure 6.4b). Furthermore, a longer exchange time of 60 min at 90 °C, which produced a film with 63% Co (Figure 6.4c), had the same general crystallite sizes and similar RMS roughness (~35 nm). Thus, incorporation of Co into the MOF film did not alter the overall film morphologies.

Films were also exchanged using ethanol as a solvent instead of the usual DMF. In general, the concentration of Co ions incorporated into the film was lower with ethanol

than DMF under similar conditions; however significant Co concentrations (40%) could be achieved at higher temperatures, though the maximum temperature is limited to ~70 °C by the boiling point of ethanol (Table 6.1). The films exchanged in ethanol exhibited smaller crystallites with widths and heights of roughly 75 and 20 nm, respectively, although some larger crystallites ~200 nm in width and ~70 nm in height also formed (Figure 6.5). The RMS roughness of the ethanol-exchanged films was 13-17 nm, which was also lower than those exchanged in DMF. These results suggest that exposure of the MOF to DMF facilitates larger crystallite sizes whereas exposure to ethanol results in distinctly smaller crystallites.

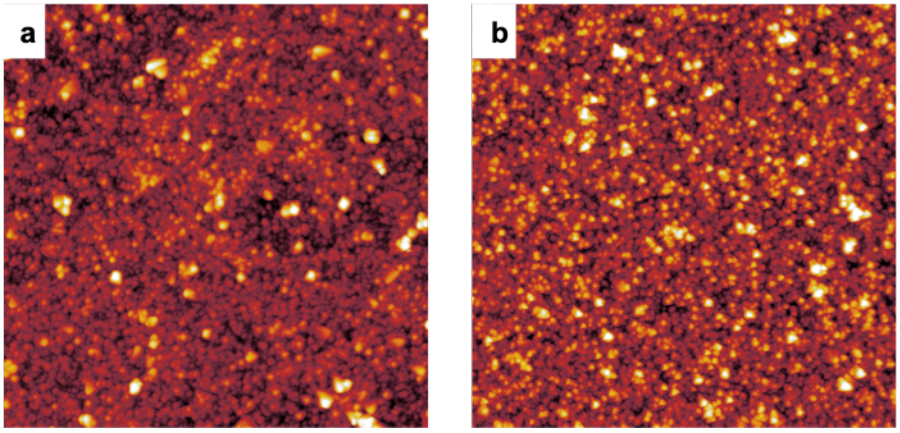

Figure 6.5: AFM images of CoCuBTC films using ethanol as the exchange solvent: a) CoCuBTC film (9% Co, exchanged at 25 °C for 3 hrs); and b) CoCuBTC film (40% Co, exchanged at 70 °C for 30 min). All images are 5 μm x 5 μm.

An additional reason for using ethanol as a solvent for the Co^{2+} exchange was because the CuBTC films were grown from precursors in an ethanol solvent, and the hypothesis was that the films might be less likely to delaminate. However, there was no evidence that the films were less likely to delaminate in ethanol compared to DMF. The factor that affected delamination the most was the defectiveness of the film. Specifically, CuBTC films that were not visually uniform were more likely to delaminate.

Film crystallites and morphologies were best preserved by storing the films in a closed vial that was purged with N_2 gas. When the films were stored under DMF, delamination occurred over time. Figure 6.6 shows a CuBTC film that was stored under DMF for 40 days; the dimensions of these crystallites, which range from 150-425 nm in width and 32-150 nm height, are much larger than the ones observed for the freshly grown film (Figure 6.4a) and suggests that DMF promotes restructuring of CuBTC into larger crystallites. Furthermore, AFM images for a CoCuBTC film (7% Co, exchanged 60 min in DMF) that was stored for 22 days in DMF exhibit the same large crystallites observed for CuBTC under DMF.

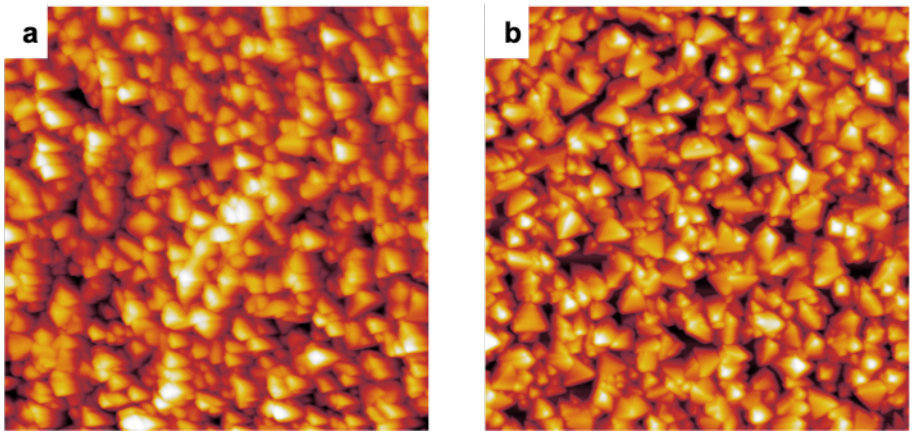

Figure 6.6: AFM images of: a) CuBTC film stored at room temperature for 40 days in DMF; and b) CoCuBTC film (7% Co, exchanged at 25 °C for 60 min) stored at room temperature for 22 days in DMF. Both images are 5 μm x 5 μm.

Standard film growth involved 40 cycles of exposure to Cu acetate followed by the BTC ligand solution. Film thicknesses were estimated as ~70 nm from cross-sectional SEM, in which the substrate was cleaved after MOF deposition in order to image the center of the film. Typical film thicknesses ranged from 40 to 105 nm with an average value of 70 nm; measurements were taken from a set of 13 images in which uniform film

thicknesses could be observed. In some AFM images of the CuBTC films, regions of the substrate appear to be visible, and the measured heights of the MOF crystallites are also in the range of 135-150 nm. These measured film thicknesses are in general agreement with the crystallite sizes measured from the AFM images. Films prepared with less immersion cycles were grown to establish a correlation between film thickness and number of dip-coating cycles. 10 cycles of exposure to metal and ligand solution resulted in crystallites 20-60 nm high and 60-180 nm wide, whereas a 20 cycle film resulted in 35-95 nm high and 80-245 nm wide features (Figure 6.7). In both cases, ~30% of the substrate was exposed compared to <5% for the 40-cycle film. Thus, a smaller number of dip coating cycles resulted in thinner films, but complete coverage of the surface was not achieved.

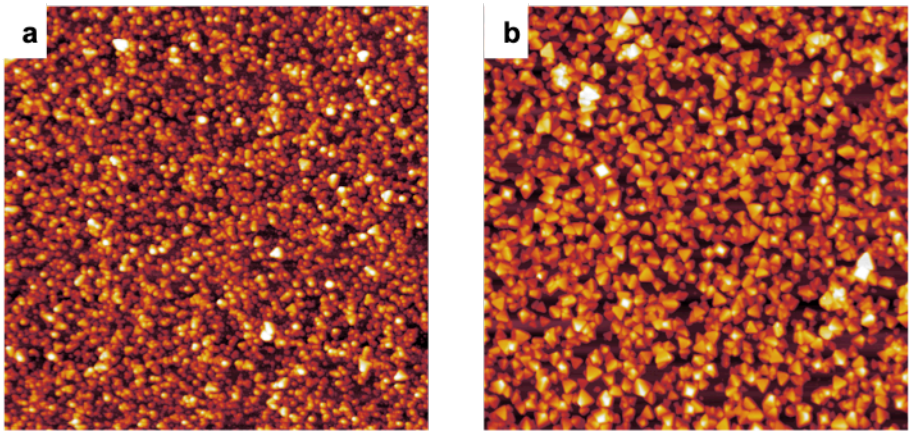

Figure 6.7: AFM images of CuBTC films grown by: a) 10 cycles; and b) 20 cycles. Both images are 5 μm x 5 μm.

6.4 Conclusions

A novel synthesis procedure for producing uniform, crystalline bimetallic MOF films has been presented. Stable Cu_3BTC_2 MOF films are directly grown on an Al_2O_3/Si(100) substrate using an alternate dip-coating procedure in the precursor solutions. Co is successfully transmetallated into the MOF structure, and the amount of

Co incorporated can be controlled by the temperature and immersion time. The crystallinity and uniformity of the bimetallic MOF films are retained upon Co transmetallation, demonstrating their stability upon exchange and ability to preserve a high surface area and porosity for potential integration in devices and electrochemical applications.

Acknowledgements

Thank you to Deepen Shakya for the AFM images, Lauren Hensley for assistance in film growth, and Dr. Ekaterina Dolgopolova for several transmetallation experiments. This research was partially supported by the U.S. Department of Energy, Office of Science, Office of Basic Energy Sciences, under Award DE-SC0019360. This work also acknowledges funding from the Donors of the American Chemical Society Petroleum Research Fund, USC's Advanced Support for Innovative Research Excellence (ASPIRE II), and NSF IGERT grant (DGE-1250052).

6.5 References

(1) Chughtai, A. H.; Ahmad, N.; Younus, H. A.; Laypkov, A.; Verpoort, F. Metal–Organic Frameworks: Versatile Heterogeneous Catalysts for Efficient Catalytic Organic Transformations. *Chem. Soc. Rev.* **2015**, *44*, 6804–6849.

(2) Liu, J.; Chen, L.; Cui, H.; Zhang, J.; Zhang, L.; Su, C.-Y. Applications of Metal–Organic Frameworks in Heterogeneous Supramolecular Catalysis. *Chem. Soc. Rev* **2014**, *43*, 6011–6061.

(3) Gascon, J.; Corma, A.; Kapteijn, F.; Xamena, F.; Llabre Xamena, F. X. Metal Organic Framework Catalysis: Quo Vadis? *ACS Catal.* **2014**, *4*, 361–378.

(4) He, Y.; Zhou, W.; Qian, G.; Chen, B. Methane Storage in Metal–Organic Frameworks. *Chem. Soc. Rev. Chem. Soc. Rev* **2014**, *43*, 5657–5678.

(5) Yang, X.; Xu, Q. Bimetallic Metal−Organic Frameworks for Gas Storage and Separation. *Cryst. Growth Des.* **2017**, *17*, 1450–1455.

(6) Herm, Z. R.; Bloch, E. D.; Long, J. R. Hydrocarbon Separations in Metal−Organic Frameworks. *Chem. Mater.* **2014**, *26*, 323–338.

(7) Yeon Lee, C.; Farha, O. K.; Jin Hong, B.; Sarjeant, A. A.; Nguyen, S. T.; Hupp, J. T. Light-Harvesting Metal-Organic Frameworks (MOFs): Efficient Strut-to-Strut Energy Transfer in Bodipy and Porphyrin-Based MOFs. *J. Am. Chem. Soc* **2011**, *133*, 15858–15861.

(8) Kent, C. A.; Mehl, B. P.; Ma, L.; Papanikolas, J. M.; Meyer, T. J.; Lin, W. Energy Transfer Dynamics in Metal-Organic Frameworks. *J. Am. Chem. Soc.* **2010**, *132*, 12767–12769.

(9) Kreno, L. E.; Leong, K.; Farha, O. K.; Allendorf, M.; Van Duyne, R. P.; Hupp, J. T. Metal-Organic Framework Materials as Chemical Sensors. *Chem. Rev* **2012**, *112*, 1105–1125.

(10) Stavila, V.; Talin, A. A.; Allendorf, M. D. MOF-Based Electronic and Optoelectronic Devices. *Chem. Soc. Rev.* **2014**, *43*, 5994–6010.

(11) Allendorf, M. D.; Schwartzberg, A.; Stavila, V.; Talin, A. A. A Roadmap to Implementing Metal-Organic Frameworks in Electronic Devices: Challenges and Critical Directions. *Chem. Eur. J.* **2011**, *17*, 11372–11388.

(12) Stassen, I.; Burtch, N.; Talin, A.; Falcaro, P.; Allendorf, M.; Ameloot, R. An Updated Roadmap for the Integration of Metal-Organic Frameworks with Electronic Devices and Chemical Sensors. *Chem. Soc. Rev.* **2017**, *46*, 3185–3241.

(13) Hendon, C. H.; Rieth, A. J.; Korzynski, M. D.; Dinca, M. Grand Challenges and Future Opportunities for Metal-Organic Frameworks. *ACS Cent. Sci.* **2017**, *3*, 554–563.

(14) Rowsell, J. L. C.; Yaghi, O. M. Metal-Organic Frameworks: A New Class of Porous Materials. *Microporous Mesoporous Mater.* **2004**, *73*, 3–14.

(15) Heinke, L.; Wöll, C. Surface-Mounted Metal–Organic Frameworks: Crystalline and Porous Molecular Assemblies for Fundamental Insights and Advanced Applications. *Adv. Mater.* **2019**, *1806324*.

(16) Sun, F.; Li, Q.; Xue, H.; Pang, H. Pristine Transition-Metal-Based Metal-Organic Frameworks for Electrocatalysis. *ChemElectroChem* **2019**, *6*, 1273–1299.

(17) Liu, J. X.; Woll, C. Surface-Supported Metal-Organic Framework Thin Films: Fabrication Methods, Applications, and Challenges. *Chem. Soc. Rev.* **2017**, *46*, 5730–5770.

(18) Kung, C.-W.; Mondloch, J. E.; Wang, T. C.; Bury, W.; Hoffeditz, W.; Klahr, B. M.; Klet, R. C.; Pellin, M. J.; Farha, O. K.; Hupp, J. T. Metal−Organic Framework Thin Films as Platforms for Atomic Layer Deposition of Cobalt Ions To Enable Electrocatalytic Water Oxidation. *ACS Appl. Mater. Interfaces* **2015**, *7*, 28223–28230.

(19) Usov, P. M.; Huffman, B.; Epley, C. C.; Kessinger, M. C.; Zhu, J.; Maza, W. A.; Morris, A. J. Study of Electrocatalytic Properties of Metal−Organic Framework PCN-223 for the Oxygen Reduction Reaction. *ACS Appl. Mater. Interfaces* **2017**, *9*, 33539–33543.

(20) Usov, P. M.; Ahrenholtz, S. R.; Maza, W. A.; Stratakes, B.; Epley, C. C.; Kessinger, M. C.; Zhu, J.; Morris, A. J. Cooperative Electrochemical Water Oxidation by Zr Nodes and Ni–Porphyrin Linkers of a PCN-224 MOF Thin Film. *J. Mater. Chem. A* **2016**, *4*, 16818–16823.

(21) Lin, S. Y.; Pineda-Galvan, Y.; Maza, W. A.; Epley, C. C.; Zhu, J.; Kessinger, M. C.; Pushkar, Y.; Morris, A. J. Electrochemical Water Oxidation by a Catalyst-Modified Metal-Organic Framework Thin Film. *ChemSusChem* **2017**, *10*, 514–522.

(22) Johnson, B. A.; Bhunia, A.; Ott, S. Electrocatalytic Water Oxidation by a Molecular Catalyst Incorporated into a Metal-Organic Framework Thin Film. *Dalt. Trans.* **2017**, *46*, 1382.

(23) Duan, J.; Chen, S.; Zhao, C. Ultrathin Metal-Organic Framework Array for Efficient Electrocatalytic Water Splitting. *Nat. Commun.* **2017**, *8*, 15341.

(24) Zhao, S. L.; Wang, Y.; Dong, J. C.; He, C. T.; Yin, H. J.; An, P. F.; Zhao, K.; Zhang, X. F.; Gao, C.; Zhang, L. J.; et al. Ultrathin Metal-Organic Framework Nanosheets for Electrocatalytic Oxygen Evolution. *Nat. Energy* **2016**, *1*, 1–10.

(25) Shimoni, R.; He, W.; Liberman, I.; Hod, I. Tuning of Redox Conductivity and Electrocatalytic Activity in Metal−Organic Framework Films Via Control of Defect Site Density. *J. Phys. Chem. C* **2019**, *123*, 5531–5539.

(26) Hod, I.; Sampson, M. D.; Deria, P.; Kubiak, C. P.; Farha, O. K.; Hupp, J. T. Fe-Porphyrin-Based Metal−Organic Framework Films as High-Surface Concentration, Heterogeneous Catalysts for Electrochemical Reduction of CO_2. *ACS Catal.* **2015**, *5*, 6302–6309.

(27) Wang, L.; Wu, Y.; Cao, R.; Ren, L.; Chen, M.; Feng, X.; Zhou, J.; Wang, B. Fe/Ni Metal-Organic Frameworks and Their Binder-Free Thin Films for Efficient Oxygen Evolution with Low Overpotential. *ACS Appl. Mater. Interfaces* **2016**, *8*, 16736–16743.

(28) Munuera, C.; Shekhah, O.; Wang, H.; Woell, C.; Ocal, C.; Wöll, C.; Ocal, C. The Controlled Growth of Oriented Metal–Organic Frameworks on Functionalized Surfaces as Followed by Scanning Force Microscopy. *Phys. Chem. Chem. Phys.* **2008**, *10*, 7257.

(29) Yang, X.; Xu, Q. Bimetallic Metal−Organic Frameworks for Gas Storage and Separation. *Cryst. Growth Des.* **2017**, *17*, 1450–1455.

(30) Kim, D.; Song, K. S.; Buyukcakir, O.; Yildirim, T.; Coskun, A. Bimetallic Metal Organic Frameworks with Precisely Positioned Metal Centers for Efficient H_2 Storage. *Chem. Commun* **2018**, *54*, 12218.

(31) Zheng, F.; Xiang, D.; Li, P.; Zhang, Z.; Du, C.; Zhuang, Z.; Li, X.; Chen, W. Highly Conductive Bimetallic Ni-Fe Metal Organic Framework as Novel Electrocatalyst for Water Oxidation. *ACS Sustain. Chem. Eng.* **2019**, *7*, 11.

(32) Dolgopolova, E. A.; Brandt, A. J.; Ejegbavwo, O. A.; Duke, A. S.; Maddumapatabandi, T. D.; Galhenage, R. P.; Larson, B. W.; Reid, O. G.; Ammal, S. C.; Heyden, A.; et al. Electronic Properties of Bimetallic Metal-Organic Frameworks (MOFs): Tailoring Density of Electronic States Through MOF Modularity. *J. Am. Chem. Soc.* **2017**, *139*, 5201–5209.

(33) Jinxuan Liu, S.; Sun, L.; Ye, L.; Liu, J.; Gao, Y.; Gong, C.; Addicoat, M.; Heine, T. Highly Oriented MOF Thin Film-Based Electrocatalytic Device for the Reduction of CO_2 to CO Exhibiting High Faradaic Efficiency. *J. Mater. Chem. A* **2016**, *4*, 15320.

(34) Liu, J.; Zhou, W.; Liu, J.; Howard, I.; Kilibarda, G.; Schlabach, S.; Coupry, D.; Addicoat, M.; Yoneda, S.; Tsutsui, Y.; et al. Photoinduced Charge-Carrier Generation in Epitaxial MOF Thin Films: High Efficiency as a Result of an Indirect Electronic Band Gap? *Angew. Chemie - Int. Ed.* **2015**, *54*, 7441–7445.

(35) Otsubo, K.; Haraguchi, T.; Sakata, O.; Fujiwara, A.; Kitagawa, H. Step-by-Step Fabrication of a Highly Oriented Crystalline Three-Dimensional Pillared-Layer-Type Metal−Organic Framework Thin Film Confirmed by Synchrotron X-Ray Diffraction. *J. Am. Chem. Soc* **2012**, *134*, 9605–9608.

(36) Haraguchi, T.; Otsubo, K.; Sakata, O.; Fujiwara, A.; Kitagawa, H. Remarkable Lattice Shrinkage in Highly Oriented Crystalline Three-Dimensional

Metal−Organic Framework Thin Films. *Inorg. Chem* **2015**, *54*, 11593–11595.

(37) Haraguchi, T.; Otsubo, K.; Sakata, O.; Fujiwara, A.; Kitagawa, H. Guest-Induced Two-Way Structural Transformation in a Layered Metal−Organic Framework Thin Film. *J. Am. Chem. Soc* **2016**, *138*, 16787–16793.

(38) Haraguchi, T.; Otsubo, K.; Sakata, O.; Kawaguchi, S.; Fujiwara, A.; Kitagawa, H. A Three-Dimensional Accordion-like Metal-Organic Framework: Synthesis and Unconventional Oriented Growth on a Surface. *Chem. Commun* **2016**, *52*, 6017.

(39) Sakaida, S.; Otsubo, K.; Sakata, O.; Song, C.; Fujiwara, A.; Takata, M.; Kitagawa, H. Crystalline Coordination Framework Endowed with Dynamic Gate-Opening Behaviour by Being Downsized to a Thin Film. *Nat. Chem.* **2016**, *8*, 377.

(40) Sakaida, S.; Haraguchi, T.; Otsubo, K.; Sakata, O.; Fujiwara, A.; Kitagawa, H. Fabrication and Structural Characterization of an Ultrathin Film of a Two-Dimensional-Layered Metal-Organic Framework, {Fe(Py)2[Ni(CN)4]} (Py = Pyridine). *Inorg. Chem.* **2017**, *56*, 7606–7609.

(41) Shekhah, O.; Liu, J.; Fischer, R. A.; Woll, C.; Wöll, C. MOF Thin Films: Existing and Future Applications. *Chem. Soc. Rev.* **2011**, *40*, 1081–1106.

(42) Falcaro, P.; Ricco, R.; Doherty, C. M.; Liang, K.; Hill, A. J.; Styles, M. J. MOF Positioning Technology and Device Fabrication. *Chem. Soc. Rev.* **2014**, *43*, 5513–5560.

(43) Liu, J.; Culp, J. T.; Natesakhawat, S.; Bockrath, B. C.; Zande, B.; Sankar, S. G.; Garberoglio, G.; Johnson, J. K. Experimental and Theoretical Studies of Gas Adsorption in $Cu_3(BTC)_2$: An Effective Activation Procedure. *J. Phys. Chem. C* **2007**, *111*, 9305–9313.

(44) Schlichte, K.; Kratzke, T.; Kaskel, S. Improved Synthesis, Thermal Stability and Catalytic Properties of the Metal-Organic Framework Compound $Cu_3(BTC)_2$. *Microporous Mesoporous Mater.* **2004**, *73*, 81–88.

(45) Xu, Q.; Li, H.; Yue, F.; Chi, L.; Wang, J. Nanoscale Cobalt Metal-Organic Framework as a Catalyst for Visible Light-Driven and Electrocatalytic Water Oxidation. *New J. Chem.* **2016**, *40*, 3032.

(46) Clough, A. J.; Yoo, J. W.; Mecklenburg, M. H.; Marinescu, S. C. Two-Dimensional Metal-Organic Surfaces for Efficient Hydrogen Evolution from Water. *J. Am. Chem. Soc.* **2015**, *137*, 118–121.

(47) Mishra, P.; Edubilli, S.; Mandal, B.; Gumma, S. Adsorption Characteristics of Metal−Organic Frameworks Containing Coordinatively Unsaturated Metal Sites: Effect of Metal Cations and Adsorbate Properties. *J. Phys. Chem. C* **2014**, *118*, 6847–6855.

(48) Diercks, C.; Lin, S.; Zhang, Y. B.; Chang, C.; Yaghi, O. Covalent Organic Frameworks Comprising Cobalt Porphyrins for the Electrocatalytic Reduction of

CO_2 in Water. *Science* **2015**, *349*, 1208–1213.

(49) Duke, A. S.; Dolgopolova, E. A.; Galhenage, R. P.; Ammal, S. C.; Heyden, A.; Smith, M. D.; Chen, D. A.; Shustova, N. B. Active Sites in Copper-Based Metal Organic Frameworks: Understanding Substrate Dynamics, Redox Processes, and Valence Band Structure. *J. Phys. Chem. C* **2015**, *119*, 27457–27466.

(50) Alaerts, L.; Séguin, E.; Poelman, H.; Thibault-Starzyk, F.; Jacobs, P. a.; De Vos, D. E. Probing the Lewis Acidity and Catalytic Activity of the Metal-Organic Framework [Cu3(Btc)2] (BTC = Benzene-1,3,5-Tricarboxylate). *Chem. Eur. J.* **2006**, *12*, 7353–7363.

(51) Liu, J.; Shekhah, O.; Stammer, X.; Arslan, H. K.; Liu, B.; Schüpbach, B.; Terfort, A.; Wöll, C. Deposition of Metal-Organic Frameworks by Liquid-Phase Epitaxy: The Influence of Substrate Functional Group Density on Film Orientation. *Materials (Basel).* **2012**, *5*, 1581–1592.

(52) Vaz, C. A. F.; Prabhakaran, D.; Altman, E. I.; Henrich, V. E. Experimental Study of the Interfacial Cobalt Oxide in Co3O4/Alpha-Al2O3(0001) Epitaxial Films. *Phys. Rev. B* **2009**, *80*, 155457.

(53) Kochubey, D.; Kaichev, V.; Saraev, A.; Tomyn, S.; Belov, A.; Voloshin, Y. Combined X-Ray Absorption Near-Edge Structure and X-Ray Photoelectron Study of the Electrocatalytically Active Cobalt(I) Cage Complexes and the Clathrochelate Cobalt(II)- and Cobalt(III)-Containing Precursors and Analogs. *J. Phys. Chem. C* **2013**, *117*, 2753–2759.

(54) Frost, D. C.; McDowell, C. A.; Woolsey, I. S. Evidence for Multiplet Splitting of 2p Photoelectron Lines of Transition-Metal Complexes. *Chem. Phys. Lett.* **1972**, *17*, 320–323.

(55) Haraguchi, H.; Fujiwara, K.; Keiichiro, F. A Study of Co Complexes by X-Ray Photoelectron Spectroscopy. *Chem. Lett.* **1975**, 409–414.

(56) Sun, Y.-H.; Yu, J.-H.; Jin, X.-J.; Song, J.-F.; Xu, J.-Q.; Ye, L. Synthesis and Characterization of First Hetero-Nuclear Molybdenum Copper Cluster with Highly Delocalized Cu(I)/Cu(II). *Inorg. Chem. Commun.* **2006**, *9*, 1087–1090.

(57) Gagne, R. R.; Allison, J. L.; Koval, C. A.; Mialki, W. S.; Smith, T. J.; Walton, R. A. X-Ray Photoelectron-Spectra of Copper(I) and Copper(II) Complexes Derived from Macrocyclic Ligands. *J. Am. Chem. Soc.* **1980**, *102*, 1905–1909.

(58) Nijem, N.; Bluhm, H.; Ng, M. L.; Kunz, M.; Leone, S. R.; Gilles, M. K.; Leone, R.; Gilles, M. K.; Leone, S. R.; Gilles, M. K. Cu1+ in HKUST-1: Selective Gas Adsorption in the Presence of Water. *Chem. Commun. (Camb).* **2014**, *50*, 10144–10147.

(59) St Petkov, P.; Vayssilov, G. N.; Liu, J.; Shekhah, O.; Wang, Y.; Woell, C.; Heine, T. Defects in MOFs: A Thorough Characterization. *Chemphyschem* **2012**, *13*,

2025–2029.

(60) Szanyi, J.; Daturi, M.; Clet, G.; Baer, D. R.; Peden, C. H. F. Well-Studied Cu-BTC Still Serves Surprises: Evidence for Facile Cu2+/Cu+ Interchange. *Phys. Chem. Chem. Phys.* **2012**, *14*, 4383–4390.

(61) Ghijsen, J.; Tjeng, L. H.; Vanelp, J.; Eskes, H.; Westerink, J.; Sawatzky, G. A.; Czyzyk, M. T. Electronic-Structure of Cu_2O and CuO. *Phys. Rev. B* **1988**, *38*, 11322–11330.

(62) Wagner, C. D.; Riggs, W. M.; Davis, L. E.; Moulder, J. F. *Handbook of X-Ray Photoelectron Spectroscopy*; Muilenberg, G. E., Ed.; Perkin Elmer Corporation: Eden Prairie, MN, 1979.

(63) Höchst, H.; Hüfner, S.; Goldmann, A. The XPS Valence Band of Nickel Metal. *Z. Phys. B* **1977**, *26*, 133–136.

(64) Senthil Kumar, R.; Senthil Kumar, S.; Anbu Kulandainathan, M. Efficient Electrosynthesis of Highly Active $Cu_3(BTC)_2$-MOF and Its Catalytic Application to Chemical Reduction. *Microporous Mesoporous Mater.* **2013**, *168*, 57–64.

APPENDIX A

YTTRIUM-INDUCED STABILITY OF THE TETRAGONAL PHASE OF ZIRCONIA THIN FILMS

Introduction

Yttrium (Y) is an excellent dopant of zirconia (ZrO_2) due to its enhancement of mechanical strength, fracture toughness, and ionic conductivity, which is desirable in materials used in high temperature ceramic applications and solid oxide fuel cells (SOFCs)[1]. ZrO_2 undergoes transformation from the cubic structure to tetragonal and monoclinic structures with decreasing temperature in order to minimize electronic repulsion between neighboring oxygen atoms and maintain short Zr-O distances. Tetragonal zirconia thin films cannot only be stabilized by oxygen vacancies resulting from reduction, but also by yttrium incorporation. The addition of yttrium replaces tetravalent Zr^{4+} with trivalent Y^{3+}, creating oxygen vacancies due to charge neutralization[2], and therefore minimizing repulsion. While yttria-stabilized zirconia (YSZ) is a well-known material, a defined model system is necessary for interpreting its function in such applications as catalysis and SOFCs. The influence of Y on ZrO_2 thin films is investigated for its effect on stabilizing the tetragonal zirconia structure under various thermal and oxidizing conditions.

Experimental

Yttrium-doped ZrO_2 thin films were grown in an ultra-high vacuum (UHV) chamber with a base pressure below 10^{-10} mbar. The chamber is equipped with a room

temperature scanning tunneling microscope (Omicron micro STM), low energy electron diffraction optics (ErLEED), and Specs Phoibos 100 hemispherical analyzer for x-ray photoelectron spectroscopy measurements (XPS). This chamber has been described in a previous publication.[3] Zirconia films are sputter deposited onto a Rh(111) crystal (9 mm x 2 mm, MaTecK, Germany) using a home-built, UHV-compatible sputter source.[4] ZrO_2 was sputter-deposited in an Ar/O_2 atmosphere ($p_{Ar} \sim 6.5 \times 10^{-6}$ mbar, $p_{O2} \sim 1.5 \times 10^{-6}$ mbar) at room temperature. One O–Zr–O repeat unit of cubic-ZrO_2(111) is defined as one monolayer, which corresponds to $\sim 9 \times 10^{18}$ Zr atoms/m^2 or ~0.3 nm thickness. The as-deposited films were not fully oxidized and were therefore post-annealed for 10 min in O_2 ($p_{O2} = 5 \times 10^{-7}$ mbar) at 625 °C for 10 minutes to form an ordered structure. Further information on ZrO_2 thin film growth has been previously described in detail.[3] Yttrium is deposited on the ZrO_2 film using an Omicron metal evaporation source in an O_2 atmosphere ($p_{O2} = 5 \times 10^{-7}$ mbar) with the zirconia film heated to 430 °C or 550 °C. The deposition rate of Y was measured by a quartz crystal microbalance (QCM) using a density of (1/5) * 4.340 = 0.868 g/cm^3 and a z-ratio of 0.835. The investigation of two Y-ZrO_2 films are outlined below.

Results and Discussion

Stabilization of the Tetragonal Phase

The film is first prepared by depositing 5 ML ZrO_2 on the Rh(111) substrate as described in the Experimental section. The STM image of the film shows the tetragonal rows of zirconia, while the LEED pattern indicates spots from the tetragonal ZrO_2 (2 × 1) structure and spots from the Rh(111) crystal below.[3] Yttrium is deposited on top of the 5 ML ZrO_2 film in an oxygen atmosphere ($p_{O2} = 5 \times 10^{-7}$ mbar) with the ZrO_2 film heated

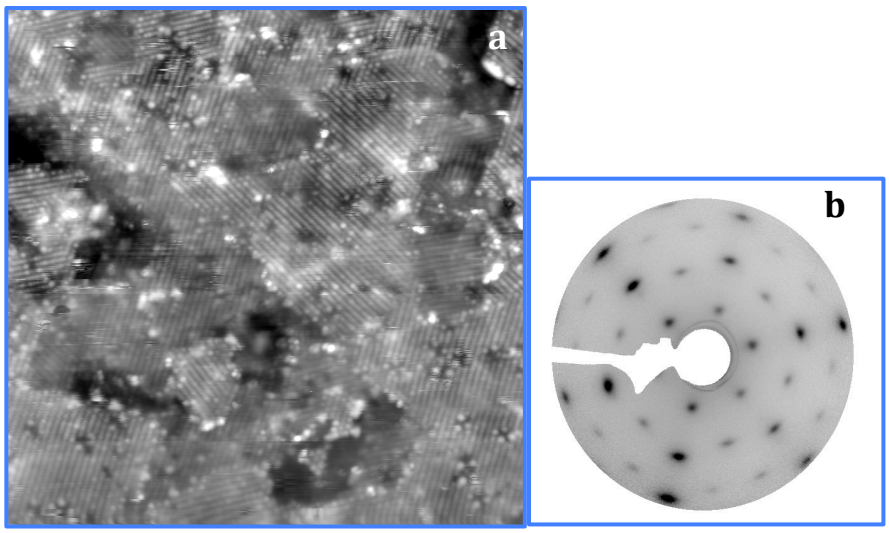

Figure A.1: 5 ML ZrO_2 film on Rh(111). a) STM image (50 nm x 50 nm); b) LEED pattern (70 eV).

to 430 °C. In Figure A.2, small triangular features can be seen in the STM image representing the deposited Y. Subsequent heating of the Y-ZrO_2 film in oxygen is analyzed post-annealing by STM, LEED, and XPS. By adding only 5% of a monolayer of Y, the tetragonal zirconia film is stabilized beyond the temperature at which pure ZrO_2

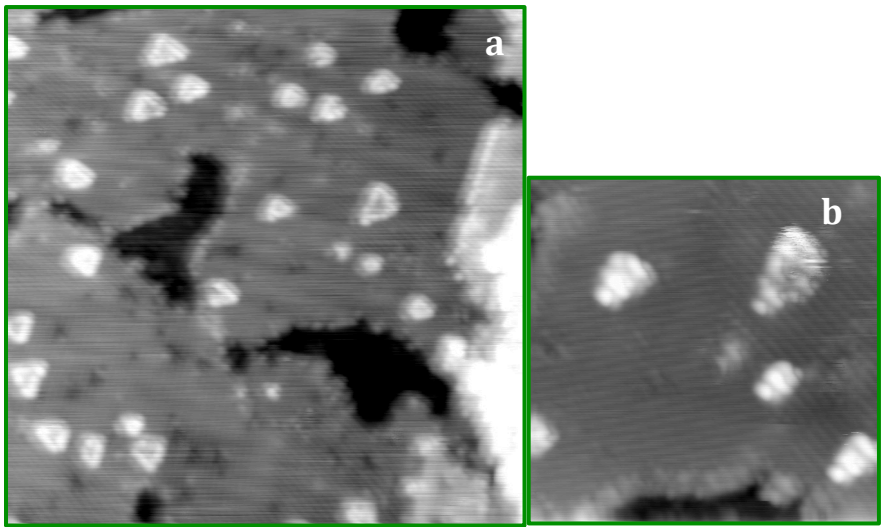

Figure A.2: STM images of 5% Y deposited on tetragonal 5 ML ZrO_2. a) Image size 50 x 50 nm; b) Image size 20 x 20 nm.

films begin to dewet. In pure ZrO_2 films, the tetragonal to monoclinic transformation occurs after full oxidation of the film, typically via oxygen dissociation on the Rh(111) substrate and spillover to zirconia.[5] The tetragonal to monoclinic transformation initiates at temperatures near 730 °C, and the zirconia film is fully transformed to the monoclinic structure at 850 °C.[3] With added yttrium, the tetragonal phase could be stabilized at a temperature of 850 °C (Figure A.3). Higher temperatures (T=920 °C) were tested for 20% of a monolayer of Y on the ZrO_2 film with the same result.

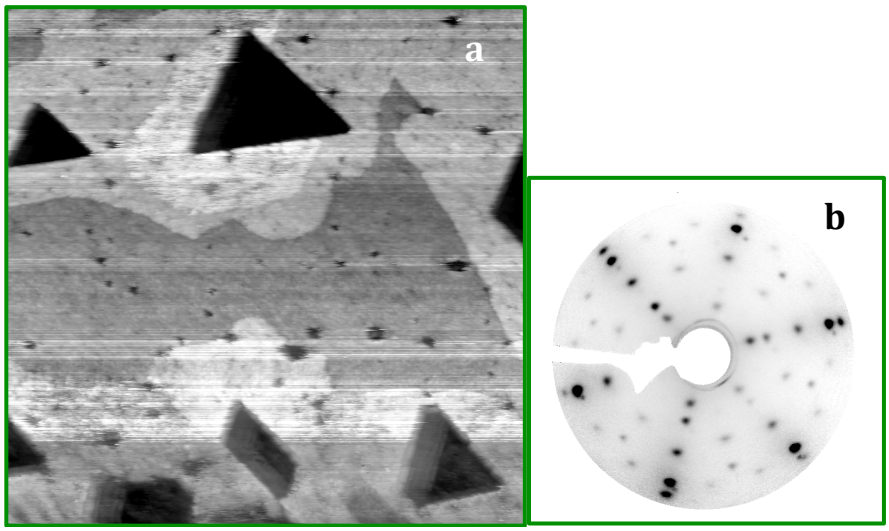

Figure A.3: 5% Y on tetragonal 5 ML ZrO_2 after heating at 850 °C for 10 min in oxygen (p_{O2} = 5 x 10^{-7} mbar). a) STM image size 200 x 200 nm. Large triangular holes form in the film. b) LEED pattern 70 eV. Tetragonal structure is maintained.

Y-Induced Transformation to the Tetragonal Phase

The deposition of yttrium can also facilitate the transformation of a monoclinic zirconia film back to the tetragonal phase. This is possible for a pure ZrO_2 film; however reducing conditions are required (950 °C in UHV).[3] With the addition of yttrium to the film, no reduction is needed. Figure A.4a shows the STM image of a monoclinic 5 ML

ZrO_2 film formed by heating at 820 °C in oxygen (p_{O2} = 5 x 10^{-7} mbar) for 10 min. The surface lattice of the monoclinic film appears hexagonal in the images, unlike the rows

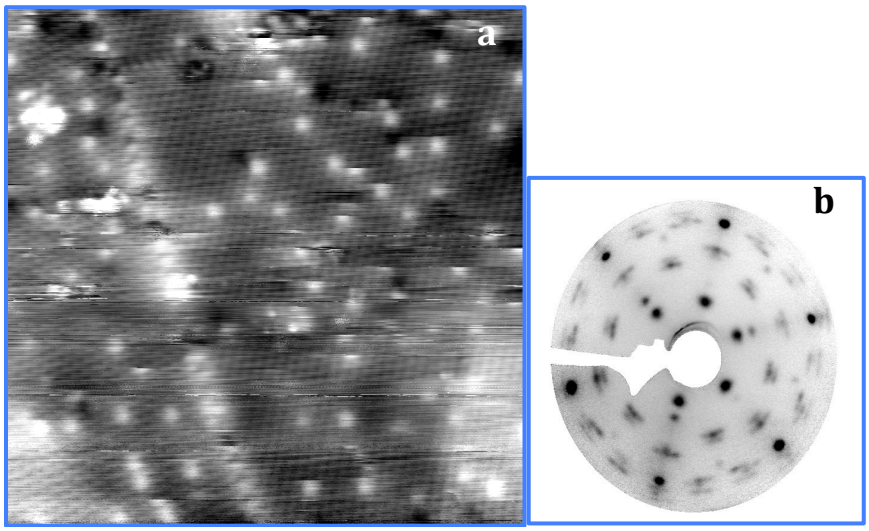

Figure A.4: Monoclinic 5 ML ZrO_2 film. a) STM image size 30 x 30 nm; b) LEED pattern 70 eV.

seen in the tetragonal film. The LEED image (Figure A.4b) clearly shows the distinction between tetragonal and monoclinic films. The splitting of the monoclinic spots in LEED are due to the expected diffraction pattern from six domains of the distorted monoclinic structure (with respect to the cubic structure).[3] After depositing 20% of a monolayer of yttrium in oxygen (p_{O2} = 5 x 10^{-7} mbar) with the film heated to 550 °C, the film remains monoclinic (Figure A.5). However, after heating the monoclinic Y-ZrO_2 film to 820 °C (the same temperature used to form the monoclinic film) in oxygen (p_{O2} = 5 x 10^{-7} mbar) for 10 min, the film was transformed back to the tetragonal phase (Figure A.5c). Since oxygen could readily dissociate on Rh(111) from the holes in the monoclinic film, this again shows that the transformation and stabilization is induced by Y alone, and not by reduction of the film.

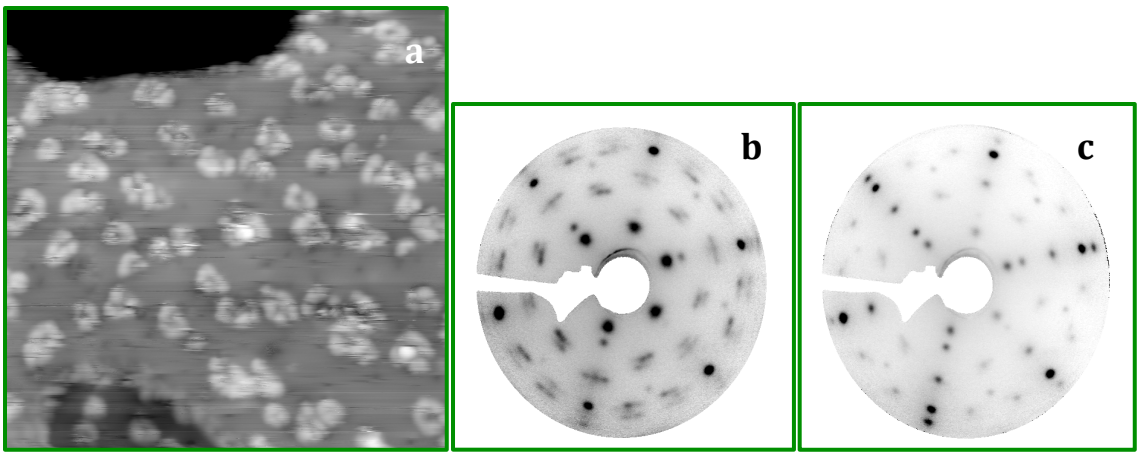

Figure A.5: a) STM image (50 x 50 nm) and b) LEED (70 eV) of as-deposited 20% Y on monoclinic 5 ML ZrO_2; c) LEED (70 eV) after annealing to 820 °C in oxygen (p_{O2} = 5 x 10^{-7} mbar) for 10 min to transform the film back to the tetragonal phase.

Insights from X-ray Photoelectron Spectroscopy

In general, the electronic structure of zirconia behaves similarly with and without yttrium. Oxygen vacancies that exist in the tetragonal ZrO_2 film, and which are not associated with Y, are positively charged and lead to band bending.[5] The oxygen vacancies are positively charged due to the close proximity of the film with the metal Rh substrate; it has been noted that electrons in oxygen vacancies are readily transferred to the metal.[6,7] As a result, XPS shows tetragonal zirconia films starting with high binding energies (~183 eV for $Zr(3d_{5/2})$) before the deposition of Y. After annealing in O_2, the films break up and oxygen vacancies are filled, leading to a shift of all peaks in the XPS toward lower binding energies (Figure A.6); when Y is present, the Y(3d) peaks shift accordingly. Coincidentally, due to the presence of Y, oxidation of the film does not lead to a structural transformation toward the monoclinic phase, as is seen in pure ZrO_2 films, mentioned above. Therefore it is assumed that oxygen vacancies are still present close to the trivalent Y ions; but these oxygen vacancies are neutral, as the electrons from the absent oxygen ions are located close to the Y ions.

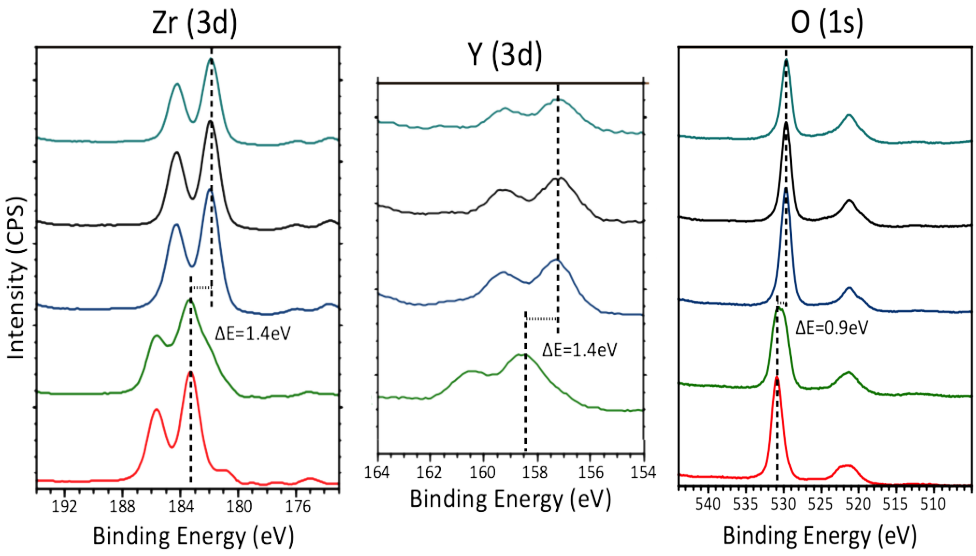

Figure A.6: XPS data of tetragonal 5 ML ZrO_2 before (red) and after (green) deposition of 0.2 ML Y; and after annealing for 10 min in oxygen (p_{O2} = 5 x 10^{-7} mbar) at 650 °C (blue), 750 °C (black), and 800 °C (turquoise).

Conclusions

With the addition of only 5% Y to a ZrO_2 film, the film was able to maintain the tetragonal phase due to the stabilizing effect of yttrium at temperatures above 800 °C. A monoclinic zirconia film can be transformed back to the tetragonal phase with the addition of yttrium at much lower temperatures and without reducing the film. The stabilizing effect of Y was linked to the inherent oxygen vacancies that accompany trivalent Y when replacing tetravalent Zr in zirconia films. The oxygen vacancies are not filled in oxidizing environments, which allows the tetragonal phase to remain stable.

Acknowledgements

Thank you to Dr. Peter Lackner, Dr. Michael Schmidt, and Dr. Ulrike Diebold from the Technical University of Vienna, Austria. Their time, mentoring, and resources made this research possible. This work also acknowledges funding from the FWF Austrian Science Fund for Functional Oxide Surfaces and Interfaces (FOXSI), and partial funding from NSF IGERT grant (DGE-1250052).

References

(1) Tao, J.; Batzill, M. Ultrathin Y2O3(111) Films on Pt(111) Substrates. *Surf. Sci.* **2011**, *605*, 1826–1833.

(2) Götsch, T.; Wallisch, W.; Stöger-Pollach, M.; Klötzer, B.; Penner, S. From Zirconia to Yttria: Sampling the YSZ Phase Diagram Using Sputter-Deposited Thin Films. *AIP Adv.* **2016**, *6*, 025119.

(3) Lackner, P.; Zou, Z.; Mayr, S.; Choi, J. I. J.; Diebold, U.; Schmid, M. Surface Structures of ZrO2 Films on Rh(111): From Two Layers to Bulk Termination. *Surf. Sci.* **2019**, *679*, 180–187.

(4) Lackner, P.; Il, J.; Choi, J.; Diebold, U.; Schmid, M. Construction and Evaluation of an Ultrahigh-Vacuum-Compatible Sputter Deposition Source. *Rev. Sci. Instrum* **2017**, *88*, 103904.

(5) Lackner, P.; Zou, Z.; Mayr, S.; Diebold, U.; Schmid, M. Oxygen Spillover on Zirconia Thin Films Observed via the Electronic Structure. *Submitt. to Surf. Sci.* **2019**.

(6) Puigdollers, A. R.; Pacchioni, G. CO Oxidation on Au Nanoparticles Supported on ZrO2: Role of Metal/Oxide Interface and Oxide Reducibility. *ChemCatChem* **2017**, *9*, 1119–1127.

(7) Puigdollers, A. R.; Schlexer, P.; Tosoni, S.; Pacchioni, G. Increasing Oxide Reducibility: The Role of Metal/Oxide Interfaces in the Formation of Oxygen Vacancies. *ACS Catal.* **2017**, *7*, 6493–6513.